Readout and Control Techniques Towards Scalable Superconducting Quantum Processors

LIANGYU CHEN

Readout and Control Techniques Towards Scalable Superconducting Quantum Processors

LIANGYU CHEN

Readout and Control Techniques Towards Scalable Superconducting Quantum Processors

Liangyu Chen
ISBN 978-91-8103-185-0

Cover:
This is a photo of the dilution refrigerator, code-named "Loki", where the main experiments in this thesis were carried out.

To Huizhong, the love of my life

Your love and care has bathed me with happiness

This is for you and our future life together

Abstract

The realization of fault-tolerant quantum computing requires the execution of quantum error-correction (QEC) schemes, to mitigate the fragile nature of qubits. In this context, to ensure the success of QEC, a protocol capable of implementing both qubit reset and leakage reduction is highly desirable together with the ability to perform fast and high-fidelity readout of the qubit s' quantum states. In this thesis, we tackle both these challenges in an architecture consisting of fixed-frequency transmon qubits pair-wise coupled via tunable couplers. We demonstrate a readout scheme that combines two microwave techniques: applying a shelving technique to the qubits that reduces the contribution of decay error during readout, and a two-tone excitation of the readout resonators to distinguish among qubits' populations in higher energy levels. We perform single-shot frequency-multiplexed qubit readout, with a 140 ns readout time, and demonstrate 99.5 % assignment fidelity for two-state readout and 96.9 % for three-state readout - without using a quantum-limited amplifier. We also demonstrate a reset scheme that is fast, unconditional, and achieves fidelities well above 99 %, thus enabling fixed-frequency qubit architectures as future implementations of fault-tolerant quantum computers. Our reset protocol uses the tunable couplers to transfer any undesired qubits' excitation to the readout resonators of the qubits, from which this excitation decays into the feedline. In total, the combination of qubit reset, leakage reduction, and coupler reset takes only 83 ns to complete. This reset protocol also provides a means to both reduce QEC cycle runtime and improve algorithmic fidelity on quantum processors.

Keywords: Quantum Computing, Superconducting Circuits, Transmons, Qubit Control and Readout

ii

List of Publications

This thesis is based on the following publications:

[A] **Liangyu Chen**, Hang-Xi Li, Yong Lu, Christopher W. Warren, Christian J. Križan, Sandoko Kosen, Marcus Rommel, Shahnawaz Ahmed, Amr Osman, Janka Biznárová, Anita Fadavi Roudsari, Benjamin Lienhard, Marco Caputo, Kestutis Grigoras, Leif Grönberg, Joonas Govenius, Anton Frisk Kockum, Per Delsing, Jonas Bylander, Giovanna Tancredi , "Transmon qubit readout fidelity at the threshold for quantum error correction without a quantum-limited amplifier". *npj Quantum Information* **9**, 26 (2023).

[B] **Liangyu Chen**, Simon Pettersson Fors, Zixian Yan, Anaida Ali, Tahereh Abad, Amr Osman, Eleftherios Moschandreou, Benjamin Lienhard, Sandoko Kosen, Hang-Xi Li, Daryoush Shiri, Tong Liu, Stefan Hill, Abdullah-Al Amin, Robert Rehammar, Mamta Dahiya, Andreas Nylander, Marcus Rommel, Anita Fadavi Roudsari, Marco Caputo, Grönberg Leif, Joonas Govenius, Miroslav Dobsicek, Michele Faucci Giannelli, Anton Frisk Kockum, Jonas Bylander, Giovanna Tancredi, "Fast unconditional reset and leakage reduction in fixed-frequency transmon qubits". *arXiv* **2409**, 16748 (2024).

[C] Sandoko Kosen, Hang-Xi Li, Marcus Rommel, Robert Rehammar, Marco Caputo, Leif Grönberg, Jorge Fernández-Pendás, Anton Frisk Kockum, Janka Biznárová, **Liangyu Chen**, Christian Križan, Andreas Nylander, Amr Osman, Anita Fadavi Roudsari, Daryoush Shiri, Giovanna Tancredi, Joonas Govenius, Jonas Bylander, "Signal Crosstalk in a Flip-Chip Quantum Processor". *PRX Quantum* **5**, 030350 (2024).

[D] Sandoko Kosen, Hang-Xi Li, Marcus Rommel, Daryoush Shiri, Christopher Warren, Leif Grönberg, Jaakko Salonen, Tahereh Abad, Janka Biznárová, Marco Caputo, **Liangyu Chen**, Kestutis Grigoras, Göran Johansson, Anton Frisk Kockum, Christian Križan, Daniel Pérez Lozano6, Graham J Norris, Amr Osman, Jorge Fernández-Pendás, Alberto Ronzani, Anita Fadavi Roudsari, Slawomir Simbierowicz, Giovanna Tancredi, Andreas Wallraff, Christopher Eichler, Joonas Govenius and Jonas Bylander, "Building blocks of a flip-chip integrated superconducting quantum processor". *Quantum Science and Technology* **7**, 035018 (2022).

[E] Christian Križan, Janka Biznárová, **Liangyu Chen**, Emil Hogedal, Amr Osman, Christopher W. Warren, Sandoko Kosen, Hang-Xi Li, Tahereh Abad, Anuj Aggarwal, Marco Caputo, Jorge Fernández-Pendás, Akshay Gaikwad, Leif Grönberg, Andreas Nylander, Robert Rehammar, Marcus Rommel, Olga I. Yuzephovich, Anton Frisk Kockum, Joonas Govenius, Giovanna Tancredi, Jonas Bylander, "Quantum SWAP gate realized with CZ and iSWAP gates in a superconducting architecture". *arXiv* **2412**, 15022 (2024).

[F] Hampus Renberg Nilsson, **Liangyu Chen**, Giovanna Tancredi, Robert Rehammar, Daryoush Shiri, Filip Nilsson, Amr Osman, Vitaly Shumeiko, Per Delsing, "A small footprint travelling-wave parametric amplifier with a high Signal-to-Noise Ratio improvement in a wide band". *arXiv* **2408**, 16366 (2024).

Acknowledgments

Looking back at these past four years at Chalmers, I recognize what an arduous, yet rewarding, journey it has been. This achievement would not have been possible without the help and support of the people around me during these times, and I am filled with profound gratitude as I express my thanks.

First and foremost, I am very grateful to my supervisor, Giovanna Tancredi. Thank you for your exceptional guidance and mentorship throughout these years. Your constant support and optimism for this project are greatly appreciated. I will always cherish the memory of your encouragement to present our results at the first March Meeting, share both the hardships and the achievements of our work, as well as the countless hours spent meticulously editing our papers. It is a true honor to be the first PhD student to graduate under your mentorship. I also extend my sincere thanks to my co-supervisor, Jonas Bylander, and examiner, Per Delsing, for providing me with this invaluable opportunity in the group and for ensuring we had access to all the resources and support as much as possible. A special note of gratitude to Simone for many insightful discussions during my initial project in the group and for your role as the discussion leader during my mid-term seminar. I am deeply thankful for your collective efforts in fostering such a nourishing and stimulating research environment.

It has been a privilege to collaborate with such a talented and passionate cohort of PhD students at QTL. To Hangxi, thank you for your warm welcome to Chalmers and for showing me the ropes around the lab. To Chris, I appreciate our insightful discussions on calibration techniques and for sharing our mutual enthusiasm for works of sci-fi and history. To Christian, thank you for your patient explanations on microwave electronics and your meticulous work in setting up Loki. To Janka, I am grateful for your expertise in fabrication and your invaluable assistance in the making of my first chip at Chalmers. To Amr, thank you for co-piloting our latest endeavors in the automatic calibration of the 25-qubit chip. And to Jiaying, Anuj, Hampus, Emil, and Theresa, thank you for your support and contributions to our vibrant team. Of course, the dedication and guidance of our experienced researchers and postdocs—Anita, Daryoush, Marcus, Andreas, Robert, Michele, Tong, and Abdullah—were essential. A heartfelt thank you to everyone on our team who is dedicated to realizing our common goal of building a quantum computer.

My deepest gratitude, of course, is reserved for Huizhong, the love of my life, with whom I have been so fortunate to share this journey. Your love and companionship transform hardships into shared joys, and your constant encouragement and wise counsel empower me to reach heights I never thought possible alone. I am also very grateful to your family, and especially to your grandmother, for welcoming me so warmly. Finally, I would never have reached this point without the unwavering love and support of my parents, Weining and Xiaohong, and my grandparents, whose caring memory has been a constant source of warmth and courage throughout my life.

Contents

Part I

Thesis

CHAPTER 1

Introduction

1.1 Quantum Information and Computation

Quantum computing has emerged as a transformative paradigm with the potential to revolutionize computational science by offering solutions to problems intractable for classical machines [1, 2]. This potential is rooted in the fundamental principles of quantum mechanics, specifically superposition and path interference [3, 4]. Unlike classical bits, which are constrained to discrete states of 0 or 1, quantum bits, or qubits, can exist in a coherent superposition of quantum states. The superposition principle allows a quantum computer to explore a vast computational space, effectively performing computations on an exponentially large number of classical states simultaneously. The vast computational space is formally described by a 2^n-dimensional complex Hilbert space for an n-qubit system [5]. This exponential scaling of the state space with the number of qubits is the origin of quantum parallelism, enabling the exploration of exponentially larger solution spaces than classically achievable with a comparable number of bits [4, 6].

Furthermore, quantum systems exhibit entanglement, a uniquely quantum correlation phenomenon wherein the quantum state of multiple qubits be-

comes intertwined, irrespective of spatial separation [7, 8]. This non-classical correlation, a direct consequence of the tensor product structure of composite quantum systems, further amplifies the computational capabilities. Entanglement, characterized by non-separable states, represents correlations that cannot be described by local hidden variable theories [9, 10] and is essential for many quantum algorithms [4, 11].

Quantum computation proceeds by applying unitary transformations, represented by $2^n \times 2^n$ unitary matrices, to state vectors, effectively evolving the system within this high-dimensional space [12]. By coherently manipulating superpositions and exploiting entanglement, quantum algorithms can achieve significant speedups for specific computational tasks, such as integer factorization (Shor's algorithm) [13] and unstructured search (Grover's algorithm) [14], demonstrating the potential for exponential quantum advantage [15]. The power of quantum computation stems from the ability to efficiently manipulate these exponentially large state spaces and exploit uniquely quantum phenomena such as quantum interference. This interference, arising from the superposition principle, allows computational paths to constructively or destructively interfere, leading to probabilistic but potentially exponentially faster solutions compared to classical algorithms, where computations follow deterministic trajectories in a classical phase space. The manipulation of these high-dimensional state vectors through unitary transformations, combined with the exploitation of quantum interference, constitutes the core of quantum algorithmic design.

1.1.1 Quantum State of a Qubit

To formally represent the state of a single qubit, we use the Dirac, or "ket," notation. A general qubit state $|\psi\rangle$ can be expressed as a superposition of the computational basis states $|0\rangle$ and $|1\rangle$:

$$|\psi\rangle = \alpha|0\rangle + \beta|1\rangle, \tag{1.1}$$

where α and β are complex amplitudes such that $|\alpha|^2 + |\beta|^2 = 1$ [1]. This normalization condition ensures that the total probability of measuring the qubit is 1. Geometrically, a single qubit state can be visualized using the Bloch sphere, a unit sphere where the north pole represents $|0\rangle$ and the south pole represents $|1\rangle$ [1]. Any pure qubit state can be mapped to a point on the
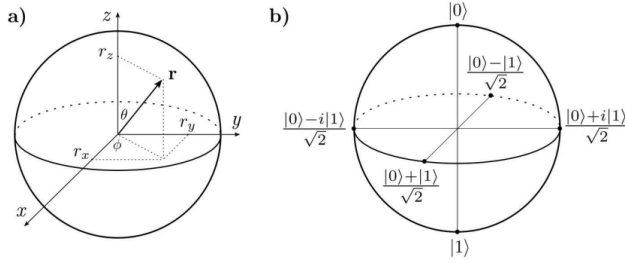
Figure 1.1: Qubit state representation on a Bloch sphere. **(a)** The geometric parameters θ and ϕ of a qubit state vector **r** in the Bloch sphere. **(b)** The locations of the basis states $|0\rangle$ (north pole) and $|1\rangle$ (south pole), along with the four equatorial superposition states on the cardinal axes [16].

surface of the Bloch sphere, parameterized by two angles, θ and ϕ, as shown in Fig. 1.1(a):

$$|\psi\rangle = \cos(\theta/2)|0\rangle + e^{i\phi}\sin(\theta/2)|1\rangle. \tag{1.2}$$

It is important to note that the global phase of the qubit state is physically irrelevant and is not explicitly represented in the Bloch sphere parametrization.

1.1.2 Coherent Quantum Operations

The evolution of a qubit state is governed by unitary transformations, which correspond to rotations on the Bloch sphere. First, the basis states $|0\rangle$ and $|1\rangle$ can be defined as

$$|0\rangle = \begin{bmatrix} 1 \\ 0 \end{bmatrix}, \quad |1\rangle = \begin{bmatrix} 0 \\ 1 \end{bmatrix}, \tag{1.3}$$

in the matrix representation of the Hilbert space. An arbitrary single-qubit rotation can then be parameterized by an angle α about the x-, y-, or z-axes applied to the quantum state:

$$X_\alpha = e^{-i\frac{\alpha}{2}\hat{\sigma}_x}, \qquad Y_\alpha = e^{-i\frac{\alpha}{2}\hat{\sigma}_y}, \qquad Z_\alpha = e^{-i\frac{\alpha}{2}\hat{\sigma}_z}, \tag{1.4}$$

using the Pauli operators

$$\sigma_x = \begin{bmatrix} 0 & 1 \\ 1 & 0 \end{bmatrix}, \quad \sigma_y = \begin{bmatrix} 0 & -i \\ i & 0 \end{bmatrix}, \quad \sigma_z = \begin{bmatrix} 1 & 0 \\ 0 & -1 \end{bmatrix}. \tag{1.5}$$

The rotation operators enable continuous manipulation of the qubit state. For example, X_α adjusts the polar angle θ by an amount α, while Z_α modifies the azimuthal phase ϕ in the Bloch sphere representation in Eq. (1.2). A fundamental subset of these rotations occurs at $\alpha = \pi$, where they reduce (up to a global phase) to the Pauli operators:

- $X_\pi = -i\sigma_x$: The X gate flips $|0\rangle \leftrightarrow |1\rangle$ (bit-flip), analogous to a classical NOT gate.

- $Z_\pi = -i\sigma_z$: The Z gate introduces a π relative phase between $|0\rangle$ and $|1\rangle$ (phase-flip).

- $Y_\pi = -i\sigma_y$: The Y gate combines both effects, equivalent to $Y = iXZ$.

These discrete π-rotations form the basis of quantum algorithms. Another common single-qubit gate is the Hadamard gate (H), essential for creating superposition states from computational basis states:

$$H = \frac{1}{\sqrt{2}} \begin{bmatrix} 1 & 1 \\ 1 & -1 \end{bmatrix}, \quad H|0\rangle = \frac{|0\rangle + |1\rangle}{\sqrt{2}}, \quad H|1\rangle = \frac{|0\rangle - |1\rangle}{\sqrt{2}}. \tag{1.6}$$

Geometrically, H corresponds to a $\pi/2$ rotation about the y-axis followed by a π rotation about the x-axis, mapping pole-to-equator states (see Fig. 1.1(b)).

1.1.3 Physical Requirements for Quantum Computation

Having introduced the basic theoretical foundations of quantum computation, we now turn to the practical considerations for building a physical quantum computer. David P. DiVincenzo outlined a set of criteria [17] that any physical system must satisfy to be considered as a suitable candidate for building a quantum computer. These criteria are:

1. **Scalable physical system with well-defined qubits:** The system must be scalable to a large number of qubits.

2. **Ability to initialize the qubits to a simple fiducial state, such as $|0\rangle$:** Qubit initialization is crucial for starting computations.

3. **Long relevant decoherence times, much longer than the gate operation time:** Qubits must maintain their quantum coherence for sufficiently long durations to perform meaningful computations.

4. **A universal set of quantum gates:** The ability to implement a universal set of quantum gates allows for arbitrary quantum computations.

5. **Qubit-specific measurement capability:** The ability to measure the state of individual qubits is necessary to extract the results of a computation.

These criteria provide a roadmap for the development of practical quantum computers and highlight the key challenges in realizing this technology. At the moment, there are many architectures for realizing quantum computers, including nuclear spin in silicon [18, 19], nitrogen-vacancies centers in diamonds [20, 21], quantum dots with semiconductor materials [22, 23], ultra-cold atoms [24, 25] and trapped ions [26, 27], all of which use microscopic systems to store and control quantum information. On the other hand, superconducting devices use millimeter-sized circuit elements to realize quantum computing [28–31]. One of the main advantages of superconducting circuits is their design flexibility and the fact that their fabrication process is compatible with established lithographic techniques for conventional integrated circuits, which has a matured semiconductor industry that can support scaled-up processes in the future. Moreover, superconducting circuits operate at microwave frequencies, where technological development has been abundant in the form of telecommunications and reliable instruments are commercially available. On top of that, superconducting systems have a coherence time on the order of microseconds, much greater than the time to perform quantum operations (gate) that is tens of nanoseconds on average, thus enabling the implementation of deep circuits and complex algorithms.

1.2 Fault-Tolerant Quantum Computation

Superconducting circuits have emerged as a leading platform for quantum computation, with recent progress demonstrating their potential [32–34]. How-

ever, realizing the full potential of quantum algorithms for solving practically relevant problems requires scaling to thousands or even millions of qubits with extremely low error rates. Current superconducting processors operate with error rates between 10^{-2} and 10^{-3} [34], significantly higher than the 10^{-18} achieved by classical computers. This discrepancy motivates the development of fault-tolerant quantum computation, a paradigm that allows for error detection and correction during the computation itself.

1.2.1 Errors in Quantum Computation

The fragile nature of quantum states makes them highly susceptible to noise, errors, and decoherence, posing significant challenges to the realization of scalable quantum computers. Unlike classical bits, qubits cannot be copied due to the no-cloning theorem [35], making traditional error correction techniques inapplicable. Even small error rates can accumulate rapidly during complex quantum computations, leading to computational failure [36]. The primary sources of errors in physical qubits can be categorized as follows:

- **Decoherence:** This is the loss of quantum coherence due to interaction with the environment. It manifests in two primary forms:
  - **Energy relaxation (T_1):** This process describes the decay of a qubit from the excited state $|1\rangle$ to the ground state $|0\rangle$, releasing energy to the environment. The probability $p_{|1\rangle}(t)$ of finding a qubit in the $|1\rangle$-state when it is undergoing energy relaxation follows the exponential decay function $p_{|1\rangle}(t) = p_{|1\rangle}(0)e^{-t/T_1}$, where $p_{|1\rangle}(0)$ is the initial probability and T_1 is the decay time constant.
  - **Pure Dephasing (T_ϕ):** This process describes the loss of phase coherence when the qubit is in a superposition state, without energy exchange with the environment. It effectively randomizes the relative phase between $|0\rangle$ and $|1\rangle$. An observable decoherence time T_2 that combines the effects of both T_1 and T_ϕ is given by $\frac{1}{T_2} = \frac{1}{2T_1} + \frac{1}{T_\phi}$.
- **Measurement errors:** These are errors that occur during the measurement of the qubit state. They can arise from imperfections in the measurement apparatus or from interactions with the environment during the measurement process.

- **Gate errors:** These are imperfections in the execution of quantum gates, which cause deviations from the intended unitary transformations. Gate errors can be further classified as:
    - **Coherent errors:** These are systematic errors that arise from miscalibration of control pulses or other deterministic imperfections. They can, in principle, be corrected through improved control techniques.
    - **Incoherent errors:** These are stochastic errors due to fluctuations in the environment or other random processes. They are more difficult to correct.

The performance of quantum operations is often characterized by their fidelity, which quantifies how close the implemented gate is to the ideal gate. A fidelity of unity represents a perfect gate. For a single-qubit gate U, the fidelity F with respect to the ideal gate V can be defined as:

$$F(U,V) = \frac{1}{d}\text{Tr}(U^\dagger V),$$ (1.7)

where d is the dimension of the Hilbert space (2 for a single qubit) and Tr denotes the trace operator [37]. For mixed states ρ and σ, the fidelity can be expressed as [37]:

$$F(\rho,\sigma) = \left(\text{Tr}\sqrt{\sqrt{\rho}\,\sigma\sqrt{\rho}}\right)^2.$$ (1.8)

Achieving high fidelity gates and long coherence times (high T_1 and T_2) are crucial for realizing fault-tolerant quantum computation.

1.2.2 Quantum-Error Correction Codes

To overcome the challenges posed by these errors, fault-tolerant quantum computation (FTQC) provides a framework for performing reliable quantum computations even in the presence of noise [12, 38, 39]. FTQC achieves this by encoding logical qubits into highly entangled states of many physical qubits [40, 41]. This encoding enables the detection and correction of errors without directly measuring or collapsing the quantum state. The key idea is to distribute the quantum information of a logical qubit across multiple physical qubits in such a way that errors affecting individual physical qubits can be

(a)   (b)
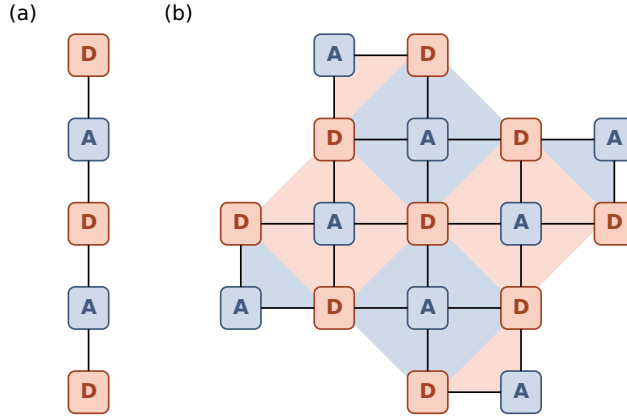
Figure 1.2: Layout of physical qubits in quantum-error-correction codes
(a) A distance-3 repetition code with 5 physical qubits that can protect the logical state against either bit-flip or phase-flip errors. "D" and "A" denote data and ancilla qubits, respectively. **(b)** A distance-3 surface code consists of 17 physical qubits, which can protect the logical states from both bit-flip and phase-flip errors simultaneously. The blue and red backgrounds indicate the X and Z-type plaquettes respectively.

detected and corrected without destroying the encoded quantum information. The goal of FTQC is to ensure that the overall logical error rate is sufficiently low to allow long and complex computations to succeed reliably.

A simple example of an error correction scheme is the classical repetition code. In this code, a classical bit 0 is encoded as 000, and a bit 1 is encoded as 111. If a single-bit flip error occurs (e.g., 000 becomes 010), a majority vote can recover the original bit based on the most frequent value of the three. However, this simple approach cannot be directly applied to quantum information due to the no-cloning theorem and the continuous nature of quantum errors. A direct measurement of the qubit will collapse its quantum state, rendering it useless in further computations. Instead, quantum error correction (QEC) codes utilize entanglement and clever encoding schemes to protect quantum information. The simplest example of a QEC code is the three-qubit bit-flip code, as shown in Fig. 1.2(a). In this code, logical qubit states $|\bar{0}\rangle$ and $|\bar{1}\rangle$ are encoded as:

$$|\bar{0}\rangle = |000\rangle, \tag{1.9}$$

$$|\bar{1}\rangle = |111\rangle, \tag{1.10}$$

in the three data qubits. If a bit-flip error (represented by the Pauli-X operator σ_x) occurs on one of the physical qubits, we can detect it using repeated measurements on the ancilla qubits. These measurements do not reveal the encoded quantum information but provide information or syndromes of the error. For instance, if the first qubit flips, $|000\rangle$ becomes $|100\rangle$. By measuring the parity of the first two qubits and the last two qubits (using operators like Z_1Z_2 and Z_2Z_3, where Z is the Pauli-Z operator), we can detect the error without determining whether the encoded state was $|\bar{0}\rangle$ or $|\bar{1}\rangle$. The measured outcomes on the ancilla qubits are called the error syndromes, and each outcome corresponds to a specific error happening on the data qubits.

However, quantum information is susceptible to more than just bit-flip errors. In addition to bit-flip errors (X errors), quantum states can also experience phase-flip errors (Z errors) and combinations of both (Y errors). The three-qubit bit-flip code described above only protects against bit-flip errors. A similar three-qubit phase-flip code can be constructed to protect against phase-flip errors, encoding $|\bar{0}\rangle = |+++\rangle$ and $|\bar{1}\rangle = |---\rangle$, where $|\pm\rangle = (|0\rangle \pm |1\rangle)/\sqrt{2}$.

An evolution of the repetition code that can protect against both bit-flip and phase-flip errors simultaneously is the surface code [40–43], shown in Fig. 1.2(b). The surface code has been shown experimentally to be a promising platform in recent implementation with superconducting qubits, notably by researchers from ETH and Google [32–34, 44, 45]. In these codes, qubits are arranged on a two-dimensional lattice, and errors are detected by measuring stabilizers, which are multi-qubit Pauli operators. In the surface code, data qubits are located on the vertices of the lattice, and ancilla qubits are located on the faces (plaquettes). There are two types of plaquettes: X-type plaquettes and Z-type plaquettes. The X(Z)-type stabilizer measures the product of X(Z) operators on two or four surrounding data qubits. The syndrome measurements, performed by measuring the ancilla qubits, reveal the location of errors on the data qubits. By repeatedly performing these measurements, errors can be tracked and corrected. Surface codes are particularly attractive due to their high error thresholds and their planar layout, which is suitable

for many physical implementations.

1.2.3 Physical-Error Threshold

Fault-tolerant quantum computation (FTQC) requires that physical error rates for all operations, including qubit control, gate execution, and measurement, remain below specific thresholds, such that increasing code distance L, i.e., corresponding to the number of the encoding physical qubits, suppresses the logical error rate exponentially instead of introducing new errors [41, 46, 47]. For many quantum error correction (QEC) codes, such as the surface code, this threshold lies in the range of 10^{-3} to 10^{-2}, depending on the specific noise model, implementation, and choice of the decoder [40, 41, 48]. Each component of the quantum processor contributes to the overall error budget [32, 33, 44, 45]:

- **Single-qubit gates** must have error rates below 10^{-3} to 10^{-4}, corresponding to fidelities in the range of 99.9% [49, 50]. Superconducting qubits routinely achieve this level of performance through precise pulse shaping, calibration, and error mitigation techniques.

- **Two-qubit gates** are more error-prone due to their longer duration and increased complexity. The threshold for two-qubit gate error rates is typically 10^{-2} to 10^{-3} [51, 52]. State-of-the-art superconducting systems achieve fidelities above 99.5%, with ongoing improvements targeting above 99.9%.

- **Measurement errors** must be below 10^{-2} to 10^{-3}, corresponding to fidelities exceeding 99% to 99.9% [53, 54]. Fast measurement is equally important to reduce the overall time for QEC cycles. For superconducting qubits, dispersive readout with Purcell filtering and quantum-limited parametric amplifiers allows measurement times on the order of 10 to 100 nanoseconds [55, 56].

- **Control crosstalk error** must be below 10^{-3} to 10^{-4} to prevent correlated errors from propagating [57, 58]. Shielding against magnetic flux, qubit frequency allocation schemes, and pulse shaping techniques are used to minimize crosstalk in qubit control.

- **Leakage errors**, where the qubit population is excited to a non-comput
  ational state, must also be minimized [59, 60]. Contributions include
  sub-optimized single and two-qubit gates, colliding qubit frequencies,
  and measurement-induced transitions.

By meeting these thresholds across all components, superconducting qubit
platforms are approaching the fault-tolerance regime, enabling scalable quan-
tum computation with robust error correction. However, realizing these comp
onent-level performances in a functional, fault-tolerant quantum computer ne-
cessitates a massive system engineering effort to integrate these components
and control a large number of qubits with high precision and stability.

1.3 Thesis Focus and Outline

Advancing towards fault-tolerant quantum computing requires expanding the
capabilities and enhancing the performance of quantum control and readout.
This work, therefore, focuses on improving high-fidelity qubit readout and
enabling essential operations such as on-demand qubit state reset and leakage
population reduction. These advancements pave the way for more robust and
scalable quantum computing with superconducting qubits.

Chapter 2 lays the theoretical foundation for this work by introducing key
concepts, beginning with the Josephson junction and its implementation as
a Cooper-pair box (CPB). The discussion then progresses to fixed-frequency
and tunable transmon qubits. This chapter provides the necessary background
for subsequent investigations and also introduces the basic single-qubit oper-
ations, readout schemes, and benchmarking techniques that are further ex-
plored in **Paper D**.

Chapter 3 focuses on improving qubit readout through both software and
hardware enhancements. Readout speed is significantly increased by incor-
porating a common-mode Purcell bandpass filter into the readout circuit,
which protects the qubit state from decay while enabling a stronger coupling
between the qubit and its readout resonator. The signal-to-noise ratio can
be further improved by integrating the travelling-wave parametric amplifier
(TWPA) developed in **Paper F** into the measurement chain, contributing to
a faster readout speed. Concurrently, readout fidelity is boosted by leverag-
ing the higher energy levels of transmons and employing multiple microwave
readout tones, as detailed in **Paper A**.

Chapter 4 delves into the subject of two-qubit gates, examining the theoretical model of a pair of qubits coupled via a tunable coupler. This coupling scheme enables the implementation of three key two-qubit gates: iSWAP, CPHASE, and SWAP, as detailed in **Papers C, D, and E**.

Chapter 5 explores qubit reset and leakage reduction, the central topic of **Paper B**, implemented using a pair of fixed-frequency qubits coupled via a tunable coupler. These operations are crucial for the future development of quantum error correction codes on the same chip architecture as the 25-qubit chip presented in **Paper C**.

Finally, **Chapter 6** concludes the thesis with a comprehensive summary of the various aspects of superconducting qubit quantum computing discussed in the preceding chapters. This concluding chapter also places these individual contributions within the broader context of advancing towards fault-tolerant quantum computing.

Superconducting Qubits and Circuit Elements

Superconducting qubits have evolved through several designs, each with unique characteristics. Early designs included the charge qubit, encoding information in the presence or absence of Cooper pairs [61, 62]; the flux qubit, utilizing magnetic flux states [63, 64]; and the phase qubit, exploiting the phase difference across a Josephson junction [65]. While these qubit types have significantly contributed to the development of superconducting quantum technologies, the transmon qubit has become the predominant choice due to its favorable balance of coherence and control [66]. The transmon is derived from the superconducting charge qubit, effectively a Cooper-pair box (CPB) with a large shunt capacitance. This design results in a set of slightly anharmonic energy levels [66], enabling selective manipulation of excitations between the ground ($|0\rangle$) and excited ($|1\rangle$) states, which are well-separated from higher energy levels and define the computational subspace. Recently, the fluxonium qubit has garnered significant interest due to its high coherence and gate fidelity [67], enabling high-fidelity two-qubit gates as demonstrated by recent experiments [68]. For discussions in this thesis, the focus will be on the transmon qubits.

This chapter explores the fundamental elements of superconducting qubits.
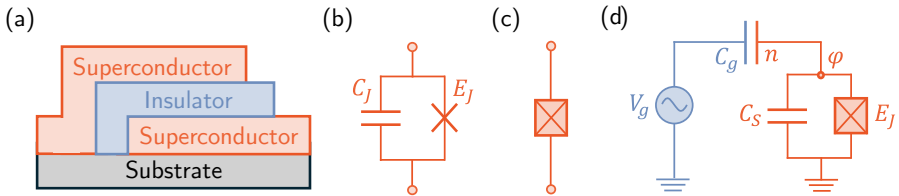
Figure 2.1: Structure and circuit of a Josephson junction.(a) Superconductor-insulator-superconductor layers of a single Josephson junction. The thickness of superconductor layer is on the order of 100 nm, whilst that of the insulator layer is approximately 2 nm. The substrate is typically silicon or sapphire. **(b)** The circuit diagram of the Josephson junction, consisting of a non-linear inductor with Josephson energy E_J and a small self-capacitance C_J. **(c)** The simplified circuit element for a Josephson junction. **(d)** Circuit model of the gated Cooper-pair box. The red indicates the island of the CPB.

Section 2.1 introduces the Cooper-pair box (CPB) and its Hamiltonian, then analyzes the energy levels within the transmon regime, demonstrating how this leads to a fixed-frequency qubit. Section 2.2 proceeds to examine the coplanar waveguide as a medium for non-destructive qubit readout. Finally, Section 2.3 explores the control elements used to excite and manipulate single-qubit quantum states.

2.1 Cooper-Pair Box

The Cooper-pair box (CPB) [69, 70] was the first charge qubit ever developed. The CPB, consists of two key components: 1) a Josephson junction: a non-linear, non-dissipative element formed by a metal-insulator-metal structure (typically Al/AlOx/Al), illustrated in Fig. 2.1. The junction is characterized by the Josephson energy E_J related to the critical current I_C across the junction and a self-capacitance C_J, typically on the order of 1 fF. Below the critical temperature of the material, the insulating barrier layer allows tunnelling of Cooper pairs, generating a potential energy term proportional to $\cos(\phi)$, where ϕ is the superconducting phase difference across the junction; 2) a capacitor: a shunt capacitance C_S in parallel with the Josephson junction, providing an electrostatic energy term. Thus, in combination with C_J, the total capacitance is $C = C_J + C_S$. The value of the total capacitance leads
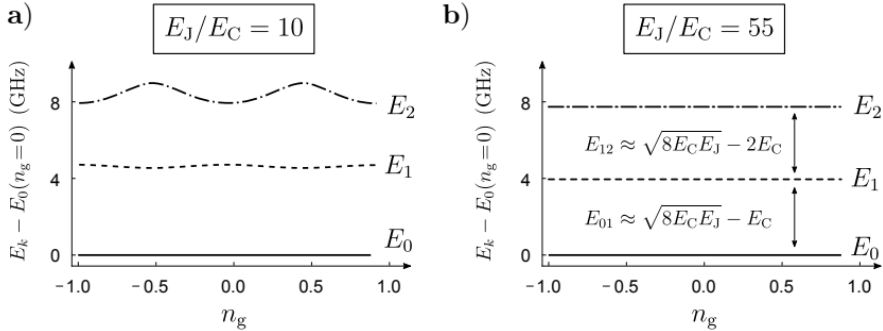
Figure 2.2: Gate charge dependent energy spectrum. **(a)** CPB regime $(E_J/E_C = 10)$. **(b)** Transmon regime $(E_J/E_C = 55)$.

to various regimes of superconducting qubits by adjusting the ratio between the charging energy E_C of the total capacitance and the Josephson energy E_J. For a typical CPB, the E_J/E_C ratio ranges approximately from one to ten [70].

The CPB Hamiltonian combines the contributions of the Josephson junction and the capacitor. In terms of the charge n, which is the number of Cooper pairs on the capacitor, and the superconducting phase ϕ, the Hamiltonian is

$$\hat{H} = 4E_C\hat{n}^2 - E_J\cos(\hat{\phi}). \tag{2.1}$$

$E_C = \frac{e^2}{2C}$ is the charging energy, which quantifies the electrostatic energy of a single Cooper pair on the capacitor and $E_J = \frac{\Phi_0 I_C}{2\pi}$ is the Josephson energy, which defines the potential energy associated with the phase difference across the junction. The superconducting flux quantum, Φ_0, is defined as $\Phi_0 = h/2e = 2.07 \cdot 10^{-15}$ Tm^{-2}. The charge $\hat{n}$ and phase $\hat{\phi}$ operators are conjugate operators satisfying the commutation relation $[\hat{\phi}, \hat{n}] = i$. The term $-E_J\cos(\phi)$ creates a periodic potential with wells in ϕ. The depth of these wells is determined by E_J, while the curvature at the minima is influenced by the ratio E_J/E_C.

The CPB can be coupled to the environment via a capacitor C_g, which can be driven by a potential difference V_g, as shown in Fig. 2.1(d). The circuit Hamiltonian is modified to include this contribution:
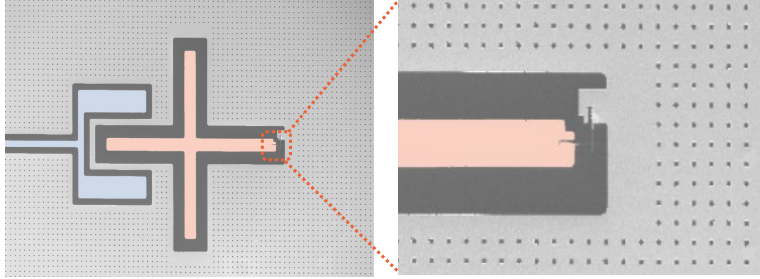
Figure 2.3: Transmon physical structure. Optical micrography of a transmon qubit, a special case of CPB. The blue area indicates the capacitor pad connector to other control elements such as a readout resonator, while the red area indicates the island of transmon qubit. The orange square highlights the location of the Josephson junction.

$$\hat{H} = 4E_C(\hat{n} - n_g)^2 - E_J \cos(\hat{\phi}), \tag{2.2}$$

where $n_g = C_g V_g/2e$ is the charge accumulated on the gate capacitor due to the applied voltage V_g. The energy spectrum of the system can be expressed in terms of Mathieu characteristic function [28, 71]. The solution for two scenarios, $E_J/E_C = 10$ and $E_J/E_C = 55$, are shown in Fig. 2.2. In the CPB regime, where $E_J/E_C = 10$, the energy levels depend strongly on n_g, which leads to its sensitivity to gate charge noise. Therefore, for a more suitable candidate as a qubit for quantum computation, we will examine the other regime $E_J/E_C = 55$ more closely.

2.1.1 Transmon Qubits

For $E_J/E_C = 55$, the system enters what is referred to as the transmon regime [66], where the energy levels vary only weakly as a function of n_g, as shown in Fig. 2.2(b), making it robust against charge fluctuations. The eigenstates of the transmon are primarily localized in phase space ϕ, reducing the dependence on the offset charge n_g. The phase variable ϕ behaves as a quasi-continuous degree of freedom within each well, suppressing the qubit's sensitivity to charge noise.

In this regime, we can rewrite the Hamiltonian in Eq. (2.2) by assuming $n_g = 0$ and expanding the $\cos(\hat{\phi})$ term in Eq. (2.2) as a perturbation in ϕ if we only consider the small oscillations of ϕ up to the 4th order:

$$\hat{H} \approx 4E_C \hat{n}^2 + \frac{1}{2} E_J \hat{\phi}^2 - \frac{E_J}{4!} \hat{\phi}^4. \tag{2.3}$$

In order to solve for the energy level E_n, the $\hat{n}$ and $\hat{\phi}$ conjugate operators can be replaced with lowering and raising operators $\hat{a}$ and $\hat{a}^\dagger$ [5]:

$$\hat{\phi} = \left(\frac{2E_C}{E_J}\right)^{\frac{1}{4}} (\hat{a} + \hat{a}^\dagger), \tag{2.4}$$

$$\hat{n} = -\frac{i}{2} \left(\frac{2E_C}{E_J}\right)^{-\frac{1}{4}} (\hat{a} - \hat{a}^\dagger). \tag{2.5}$$

Then the transmon Hamiltonian becomes

$$\hat{H} = \sqrt{8E_J E_C}\, \hat{a}^\dagger \hat{a} - \frac{E_C}{12} \left(\hat{a} + \hat{a}^\dagger\right)^4. \tag{2.6}$$

The second term is a small contribution and thus can be treated with perturbation theory. The eigenenergies of the transmon Hamiltonian can thus be approximated as:

$$E_n = \hbar\omega_n \approx \sqrt{8E_J E_C} \cdot n - \frac{E_C}{2} \left(n^2 + n\right),$$

where n indexes the eigenstates ($n = 0, 1, 2, \ldots$) giving the eigenfrequencies ω_n. The transmon's anharmonicity η is defined as the difference in spacing between successive energy levels, which is:

$$\eta = \Delta\omega_{n+1,n+2} - \Delta\omega_{n,n+1} = (\omega_{n+2} - \omega_{n+1}) - (\omega_{n+1} - \omega_n) = -\frac{E_C}{\hbar}. \tag{2.7}$$

The weak anharmonicity, $-E_C/\hbar$, ensures that the transmon behaves as a qubit, allowing selective manipulation between $|0\rangle$ and $|1\rangle$ without significant leakage to higher levels.

The optical micrography of the physical structure of a transmon is shown in Fig. 2.3. The cross-shaped capacitance is shunted to the ground via the
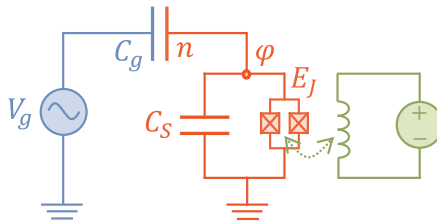
Figure 2.4: Flux-tunable transmon. Comparing to a fixed-frequency qubit, there are two Josephson junction in parallel, and a DC line is added to be able to thread magnetic flux through the loop formed by the two junctions in order to tune the frequency of qubit.

Josephson junction. There are many degrees of freedom in the physical geometry and circuit design of the transmon, which is an area of great interest [72].

2.1.2 Flux-tunable Transmon Qubits

The transmon circuit can be further modified for increasing flexibility. Adding another Josephson junction in parallel creates a so-called superconducting quantum interference device (SQUID), which enables the resonant frequency of the qubit to be tuned in situ [73, 74]. This feature is useful to evaluate frequency configuration during design iterations, probe defects in the environment, and most importantly, to enable high on/off ratio coupling between qubits for implementation of two-qubit gates.

Physically, a SQUID consists of two Josephson junctions connected in parallel, forming a loop where magnetic flux can be threaded through, as shown in Fig. 2.4. This is typically achieved by sending a current in a coplanar waveguide shorted near the SQUID loop through a mutual inductance. The Hamiltonian of the tunable transmon can be written as

$$\hat{H} = 4E_C \hat{n}^2 - E_{J_1} \cos \hat{\phi}_1 - E_{J_2} \cos \hat{\phi}_2, \tag{2.8}$$

where E_{j_i} and ϕ_i is the Josephson energy and phase difference across each junction, respectively. The phase ϕ_1 is related to ϕ_2 by the external flux Φ_{ext} due to the quantization of magnetic field in terms of flux quantum $\Phi_0 = \frac{h}{2e}$. Thus, a constant operator can be defined as $2\pi\Phi_{\text{ext}}/\Phi_0 = \hat{\phi}_1 - \hat{\phi}_2$, while the
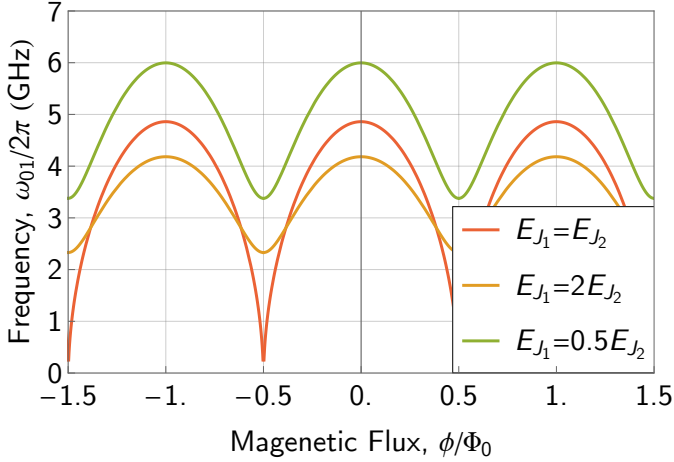
Figure 2.5: Flux dependent SQUID frequency. Resonant frequencies ω_{01} of flux-tunable transmons as a function of the magnetic flux for different SQUID E_{J1}/E_{J2} asymmetry.

effective phase difference can be defined as $\varphi = \hat{\phi}_1 + \hat{\phi}_2$. The Hamiltonian can be re-arranged in a similar form as the case with a single junction,

$$\hat{H} = 4E_C\hat{n}^2 - E_J(\Phi_{\text{ext}})\cos\hat{\varphi}, \tag{2.9}$$

albeit with the flux depended Josephson energy $E_J(\Phi_{\text{ext}})$ being

$$E_J(\Phi_{\text{ext}}) = (E_{J_1} + E_{J_2})\left|\cos\left(\pi\frac{\Phi_{\text{ext}}}{\Phi_0}\right)\right|\sqrt{1 + \left(\frac{E_{J1} - E_{J2}}{E_{J_1} + E_{J_2}}\right)^2 \tan^2\left(\pi\frac{\Phi_{\text{ext}}}{\Phi_0}\right)} \tag{2.10}$$

The qubit frequency can be similarly derived as

$$\omega_{01} = \frac{1}{\hbar}\left(\sqrt{8E_C E_J(\Phi_{\text{ext}})} - E_C\right), \tag{2.11}$$

which is dependent on the flux through the SQUID loop with a periodicity of a flux quantum Φ_0, as shown in Fig. 2.5. The frequency range of the tunable SQUID can be modified by choosing a corresponding ratio between E_{J_1} and E_{J_2} to suit the design need. For example, at the maximal or mini-

(a)

(b)
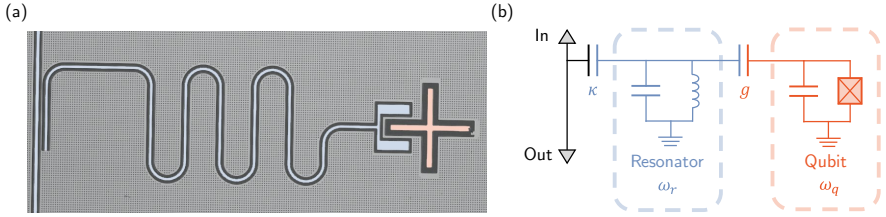
Figure 2.6: Readout circuit model. **(a)** Optical micrograph of the readout resonator coupled to a transmon qubit. **(b)** The equivalent circuit model of the readout resonator and the transmon. The resonator is coupled to the qubit via a capacitor with strength g, and to the input/output feedline with strength κ.

mal frequency, the SQUID is insensitive to flux fluctuation to the first order, improving the coherence property of the qubit, which is so-called the qubit 'sweet-spot'. Therefore, in the case of a tunable transmon, it is preferred to design the tunability curve such that the sweet-spot frequency targets the desired operating range [75].

2.2 Readout Resonators

Readout resonators are central to the measurement of superconducting qubits, as they provide an interface between the quantum state of the qubit and the classical measurement apparatus [76, 77]. They are implemented as coplanar waveguides [78] or lumped-element resonators [79] in a 2D planar geometry, as illustrated in Fig. 2.6. The resonant frequency of the readout resonator, denoted as ω_r, is chosen to be detuned from the qubit frequency ω_q to enable a dispersive interaction via direct capacitive coupling while minimizing direct energy exchange [76, 77]. In this configuration, the interaction between the qubit and the resonator is described by the Jaynes-Cummings Hamiltonian:

$$\hat{H} = \hbar\omega_r \hat{a}^\dagger \hat{a} + \frac{\hbar\omega_q}{2}\hat{\sigma}_z + \hbar g(\hat{a}^\dagger \hat{\sigma}_- + \hat{a}\hat{\sigma}_+),$$

where $\hat{a}^\dagger$ and $\hat{a}$ are the creation and annihilation operators of the resonator mode, $\hat{\sigma}_z$, $\hat{\sigma}_-$, and $\hat{\sigma}_+$ are the Pauli operators representing the qubit, and g is the coupling strength. When the detuning $\Delta = \omega_q - \omega_r$ satisfies the condition $|\Delta| \gg g$, the system enters the dispersive regime. In this regime, the qubit

and resonator no longer exchange energy directly, and the Hamiltonian can be approximated as:

$$\hat{H}_{\text{disp}} = \hbar\omega_r \hat{a}^\dagger \hat{a} + \frac{\hbar\omega_q}{2}\hat{\sigma}_z + \hbar\chi\hat{a}^\dagger \hat{a}\hat{\sigma}_z, \qquad (2.12)$$

where $\chi = g^2/\Delta$ is the dispersive shift, which quantifies the qubit-state-dependent frequency shift of the resonator. This interaction enables a mechanism where the state of the qubit modifies the effective frequency of the resonator, creating a shift of $\pm\chi$ depending on whether the qubit is in the $|0\rangle$ or $|1\rangle$ state.

This treatment assumes the qubit to be an ideal two-level system. In reality, the dispersive shift is dependent on the presence of higher energy levels of the transmon. Taking that into account, the dispersive shift of the resonator, depending on the qubit being in $|0\rangle$ and $|1\rangle$, can be expressed as

$$\chi_{01} = \frac{g^2}{\Delta(1 + \Delta/\eta)}, \qquad (2.13)$$

where η is the anharmonicity of the transmon.

These two expressions of dispersive shift can be observed through different experiments. The strength of χ can be extracted by measuring the bare frequency of the resonator, $\omega_{\text{r,bare}}$, which is achieved by finding a stable resonator frequency at high drive power [80], as shown in Fig. 2.7. At low power, the qubit is ideally at $|0\rangle$, excluding thermal excitation, representing the scenario where the resonator is coupled to the ground state of qubit $\omega_{\text{r,coupled}} = \omega_{\text{r},|0\rangle}$. Therefore, the dispersive shift $\chi = g^2/\Delta$ can be approximate as $\omega_{\text{r,coupled}} - \omega_{\text{r,bare}}$. This experiment can be performed as a means to see if the qubit that the resonator is coupled to is functional or not. If there is no change in resonator frequency at high power, then the qubit is likely to be defective.

Next, the qubit-state dependent dispersive shift χ_{01} is characterized by preparing the qubit in either $|0\rangle$ or $|1\rangle$ before probing the resonator frequency response. A typical response for different qubit states is illustrated in Fig. 2.8. The difference in resonator frequency corresponds to the relation $|\omega_{\text{r},|0\rangle} - \omega_{\text{r},|1\rangle}| = |2\chi_{01}|$, which is stated previously. Combining these two methods, we can reliably calculate the qubit-resonator coupling strength g to compare with the design parameters and understand the qubit and readout performance.
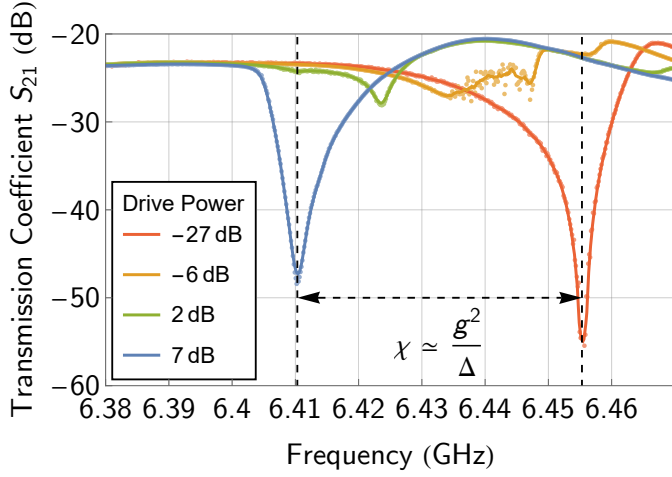
Figure 2.7: Readout resonator response at various readout drive power.
The resonator frequency shifts between two stable regimes as drive power increases.
The difference between low and high power frequency $\omega_{r,coupled} - \omega_{r,bare}$ is approximately the dispersive shift $\chi = g^2/\Delta$ of a two-level system.
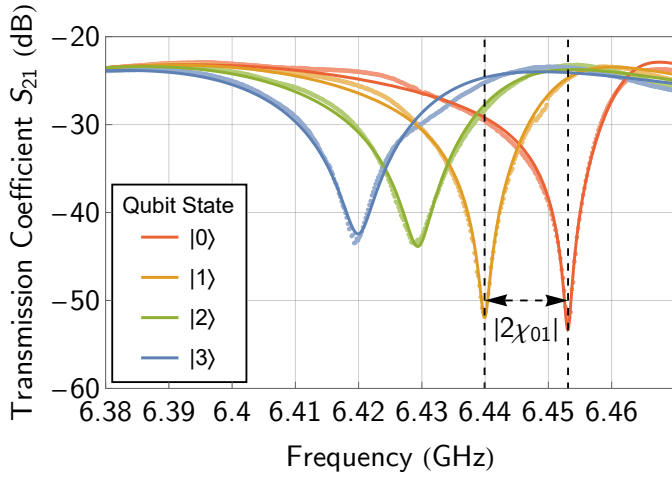
Figure 2.8: Qubit-state depended resonator response. The difference in resonator frequency between qubit being at $|0\rangle$ and $|1\rangle$ corresponds to the dispersive shift χ_{01}.

2.3 Single-Qubit Controls

Initially, the qubit is most likely at its quantum ground state according to the Boltzmann distribution for a typical transmon with a frequency higher than 2 GHz in a 10 mK environment. To control the state of the qubit, a microwave drive signal is sent to the qubit via a co-planar waveguide terminated near the transmon island, forming a capacitive coupling. The shape of the drive pulse can be expressed as

$$V_\mathrm{d}(t) = A\varepsilon(t)\sin(\omega_\mathrm{d}t + \phi), \tag{2.14}$$

where A is the amplitude of the pulse, ω_d is the carrier frequency of the drive, typically identical to the qubit frequency, ϕ is the phase of the drive, and $\epsilon(t)$ is the envelope of the pulse. To minimize the bandwidth of the pulse and avoid driving unwanted transitions, a Gaussian envelope is typically chosen,

$$\epsilon(t) = e^{-\frac{1}{2\sigma^2}(t-t_0)^2}, \tag{2.15}$$

where σ is the width of the pulse and t_0 indicates the center of the pulse in time domain. The Hamiltonian of the driven qubit system in the two-level computational subspace can be derived as

$$\hat{H} = \hat{H}_q + \hat{H}_d = \underbrace{-\frac{\hbar\omega_q}{2}\hat{\sigma}_z}_{\hat{H}_q} + \underbrace{\hbar\Omega\epsilon(t)\sin(\omega_d t + \alpha)\hat{\sigma}_y}_{\hat{H}_d}, \tag{2.16}$$

where $\sigma_{x,y,z}$ are the Pauli operators and we define the Rabi frequency as

$$\Omega = \frac{2E_C}{\hbar}\frac{C_g}{e}\left(\frac{E_J}{2E_C}\right)^{1/4} A, \tag{2.17}$$

that is proportional to the drive amplitude A as well as the capacitance C_g between the control line and the transmon island. The Rabi frequency indicates the coupling strength between the drive signal and the qubit. To understand the evolution of the driven qubit state, we first move to the rotating frame of the drive signal ω_d, where the transformed qubit state is $|\psi'\rangle = e^{-i\omega_d\hat{\sigma}_z t/2}$. Then, assuming that the drive frequency is near-resonant with the qubit frequency, we can neglect higher frequency terms in the Hamiltonian, performing what is typically referred to as the rotating wave approxi-

mation. These simplifications lead to

$$\hat{H}'(t) = -\frac{\hbar(\omega_q - \omega_d)}{2}\hat{\sigma}_z + \frac{\hbar\Omega}{2}\epsilon(t)(\hat{\sigma}_x \cos\ \phi + \hat{\sigma}_y \sin\ \phi). \qquad (2.18)$$

We then have full control over the quantum state vector on the Bloch sphere mentioned in Sec. 1.1.2 by carefully selecting the amplitude A and phase ϕ of the control pulse. Specifically, the amplitude A controls the angle of rotation and the phase ϕ sets the axis of rotation. For example, a rotation around $\{X, Y\}$-axis corresponds to a phase ϕ of $\{0, \pi/2\}$. On the other hand, rotation around the Z-axis can be implemented as a virtual gate by adjusting the reference frame of subsequent operations rather than applying an explicit physical pulse [58].

2.3.1 Single-qubit Gate Calibration

In experiments, we employ the following protocol to calibrate the single-qubit related operations in order to reach the optimal gate performance:

- **Pulse parameter calibration.** We can find the appropriate π-pulse amplitude with a Rabi experiment where the drive amplitude A is swept for a fixed pulse duration. The drive frequency ω_d can be precisely calibrated to match with the qubit frequency ω_q with a Ramsey experiment. This procedure is usually repeated to ensure the accuracy of the single qubit drive pulse [81].

- **DRAG correction.** The Derivative Removal by Adiabatic Gate (DRAG) technique addresses leakage errors to the $|2\rangle$-level and phase error caused by the AC Stark shift during microwave-driven qubit control [81–83]. DRAG suppresses these effects by modifying the pulse envelope across both quadratures (I and Q). The standard DRAG waveform is defined as:

$$\epsilon_{\text{DRAG}}(t) = \epsilon(t) + i\alpha\frac{d\epsilon(t)}{dt} + \beta\frac{d^2\epsilon(t)}{dt^2}, \qquad (2.19)$$

where $\epsilon(t)$ is the original Gaussian or cosine-shaped envelope, α scales the first derivative (quadrature correction), and β suppresses residual $|2\rangle$-population via second-order terms [81, 83]. The derivative terms
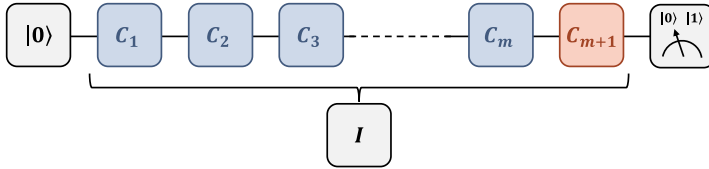
Figure 2.9: Scheme of a m-Clifford sequence for single-qubit gate randomized benchmarking. Each C_i is chosen randomly from the single-qubit Clifford group. With the C_{m+1} recovery Clifford gate, the sequence ideally condenses into an identity operation.

create destructive interference for $|2\rangle$ transitions while compensating for the Stark shift.

- **Single shot readout optimization.** The readout pulse amplitude and frequency are tuned in order to achieve the maximal single shot state identification fidelity to distinguish between $|0\rangle$ and $|1\rangle$ [84, 85]. Furthermore, the three-level readout that includes the $|2\rangle$ state is later calibrated, resulting in the optimized state assignment probability. More details on single-shot readout optimization are introduced in Chapter 3.

2.3.2 Single-Qubit Randomized Benchmarking

After the calibration procedure, we perform single-qubit gate randomized benchmarking to have a quantitative measure of the gate performance [86]. The randomized benchmarking sequence is constructed from m single-qubit gates that are randomly chosen from the single qubit Clifford group that includes $\pi/2$, π, $3\pi/2$ rotations around the X, Y and Z axes as well as the Hadamard gate [87]. Each Clifford gate is then decomposed into π and $\pi/2$ gate pulses in the experiment. Therefore, one Clifford gate contains a total of 1.875 physical single qubit gates on average. After m gates have been applied, the recovery Clifford gate is added, which inverts the operation of the whole sequence, ideally returning the qubit to the ground state. The recovery Clifford gate exists within the Clifford group as well. At the end of the $m+1$ element long sequence, the value of the σ_Z operator is measured with single-shot readout. The entire sequence generation and measurement procedure is typically repeated 50 times to acquire a significant sample size among the entire Clifford sequence space [88].

27
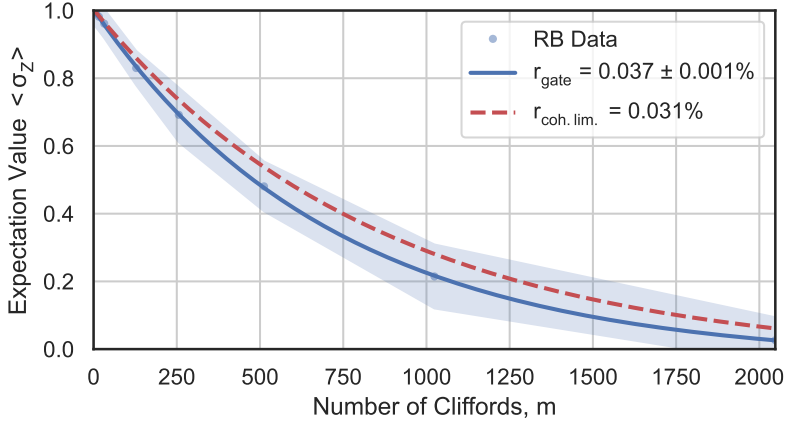
Figure 2.10: The measured sequence fidelity $F = \langle \sigma_Z \rangle$ is plotted as a function of number of Cliffords m in the sequence. Each point in the measurement is averaged over 50 randomly generated m-Clifford sequences.

The sequence fidelity F is measured as the expectation value of the single-qubit correlator $\langle \sigma_Z \rangle$ of the target qubit and as a function of the sequence length m. As illustrated in Fig. 2.10, the result can be fitted with an exponential decay from $\langle \sigma_Z \rangle = 1$, where the qubit is in the ground state, to $\langle \sigma_Z \rangle = 0$, where the qubit is in a maximally mixed state in the $|0\rangle$ and $|1\rangle$ basis. The data can be fitted with the equation

$$\langle \sigma_Z(m) \rangle = A p^m + B, \tag{2.20}$$

where $1 - p$ is the rate of depolarization per Clifford gate and the parameters A and B contain the state preparation and measurement errors as well as the contribution from leakage out of the computational subspace [88]. The gate error per Clifford can be estimated from the depolarizing rate p with

$$r_{\mathrm{RB}} = \frac{d-1}{d}(1-p), \tag{2.21}$$

where $d = 2^n$ is the dimensionality of the Hilbert space and $n = 1$ is the number of qubits. For the results shown in Fig. 2.10, the best fitted parameters are $1 - p = (0.1381 \pm 0.0012)\%, A = 1.038 \pm 0.004, B = -0.035 \pm 0.004$

and $r_{\mathrm{RB}} = (0.0691 \pm 0.0006)\%$. The small B suggests that the leakage due to the single qubit gates are negligible. Since there are 1.875 single qubit gates in each Clifford, the error per gate can be further calculated to be $r_{\mathrm{gate}} = r_{\mathrm{RB}}/1.875 = (0.0368 \pm 0.0003)\%$. To understand the limitation on the fidelity of the single qubit gate, we calculate the contribution of decoherence by using the following equation that is generalized for a system with N qubits,

$$\bar{r}^N_{\mathrm{coh.lim.}} = 1 - \frac{d}{2(d+1)}\tau \sum_{k=1}^{N}(\Gamma_1^k + \Gamma_\phi^k), \qquad (2.22)$$

where Γ_1^k (Γ_ϕ^k) is the relaxation (dephasing) rate of the qubit k [89]. For this particular qubit, the coherence limit on the gate error is calculated to be 0.0309% for a 20 ns gate, contributing to 84 % of the total gate error. The performance is on par with the state-of-the-art quantum processors with superconducting qubits [34].

CHAPTER 3

Fast High-fidelity Qubit Readout

With the recent demonstrations of quantum error correction [32, 33, 44, 45], superconducting circuits are one of the leading platforms towards the realization of a fault-tolerant quantum computer [36, 40, 41]. However, despite the remarkable progress, achieving fast and high-fidelity single-shot readout of the qubits' states remains a challenge. As a comparison, while the two-qubit-gate fidelities are approaching the 0.1% error threshold [90–93], readout errors are typically at the 1% level for two-state readout [54, 94–96]. Similarly, the implementation of high-fidelity single- and two-qubit gates takes between 10 and 100 ns [92, 93, 97], while a readout measurement can take from hundreds of nanoseconds to a few microseconds [54, 94–97]. Notably, readout performances with fidelity $> 99\%$ in less than 100 ns readout time have been achieved in [54, 96]. Further improvement in the readout of superconducting qubits is therefore crucial to reliably cross the threshold of efficient error correction, which is estimated to be less than 0.5% for the break-even point [41]. Moreover, having a fast and high-fidelity measurement scheme can boost the repetition rate for both quantum-computing and quantum-communication applications [98–102] and is essential for achieving fast reset protocols [96, 103].

In superconducting circuits, as discussed in Section 2.2, the state of a super-

conducting qubit is typically read out by detecting the dispersive frequency shift of a resonator coupled to the qubit [77]. The predominant source of error is the relaxation of the qubit from the excited ($|1\rangle$) to the ground ($|0\rangle$) state during the readout. On short time scales, this error grows almost linearly with the ratio between the readout time τ_r and the qubit relaxation time T_1 [54], and can be mitigated by reducing τ_r. It is worth noting that various high-power readout schemes have been exploited to decrease the measurement time [104, 105]. Furthermore, Purcell filters [53, 106, 107] and quantum-limited or near-quantum-limited amplifiers [108–111] have been implemented and, with the combination of both, a readout fidelity exceeding 99 % within 100 ns has been demonstrated [54, 94, 112].

In this Chapter, building on the basic principles of dispersive readout, we start with investigating Purcell filter design for faster and higher fidelity readout. Then, the implementation of an improved readout scheme that boosts the state-assignment fidelity and reduces the contribution of decay error during readout is discussed in full detail. Finally, we examine the integration of a travelling-wave parametric amplifier(TWPA) into our readout chain and characterize the improvement in readout speed.

3.1 Purcell Filter for Fast Readout

The speed and performance of dispersive readout depend on the coupling strength κ between the resonator and the external measurement line. A strongly coupled resonator (lower quality factor $Q = \omega/\kappa$) allows for faster readout but can introduce additional noise and decoherence. Conversely, a weakly coupled resonator (higher Q) ensures less disturbance but results in slower measurement [77]. Optimizing this trade-off is critical for achieving high-performance readout.

While dispersive readout is effective, it introduces potential sources of decoherence, primarily due to the coupling of the qubit to the measurement environment through the resonator. One significant risk is the Purcell effect, which arises when the qubit radiatively decays into the resonator and, through it, into the measurement line [77, 107]. This decay reduces the qubit's relaxation time T_1 and can become particularly severe for fast readout configurations with strongly coupled resonators.
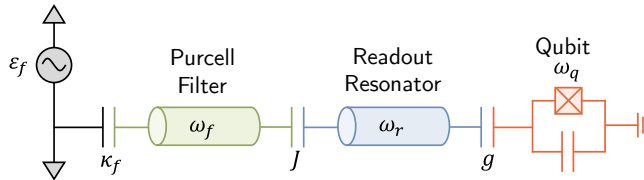
Figure 3.1: Readout circuit scheme with the additional Purcell filter. Both the readout resonator and the Purcell filter are represented as distributed element coplanar waveguide resonators, with a capacitive coupling of strength J. The Purcell filter is centered at frequency ω_f and coupled to the feedline with strength κ_f.

The Purcell effect is governed by the decay rate [77]:

$$\Gamma_P = \kappa \frac{g^2}{\Delta^2},$$

which shows that increasing κ (to enable fast readout) also increases Γ_P, directly impacting the qubit's coherence.

A Purcell filter is employed to enable fast readout without sacrificing qubit coherence. The filter suppresses the decay of the qubit excitation into the feedline by introducing a frequency-selective impedance mismatch that is effectively a bandpass filter around the resonator frequency. This allows the resonator to remain strongly coupled to the qubit for fast readout while protecting the qubit from Purcell-induced decoherence [107], thus reducing Γ_P without sacrificing either κ or g. This engineered suppression enables high-fidelity, fast readout — a critical requirement for quantum error correction and scalable architectures [53].

3.1.1 Common-mode Purcell filter

To understand how the Purcell filter functions, we start by analyzing the readout resonator-Purcell bandpass filter system with input-output theory [113]. We consider the system sketched in Fig. 3.1, where a qubit of frequency ω_q is coupled to a readout resonator of frequency ω_r with strength g. The resonator is coupled to the Purcell filter, centered at frequency ω_f with coupling J. The Purcell filter is coupled to the feedline with a coupling κ_f. The equations of motion of the classical field amplitudes $\alpha(t)$ and $\beta(t)$ in the readout resonator

and in the Purcell filter resonator are, respectively [107],

$$
\begin{aligned}
\dot{\alpha}(t) &= -i\Delta_{rd}\alpha(t) - iJ\beta(t) - \frac{\gamma_a}{2}\alpha(t), \\
\dot{\beta}(t) &= -i\Delta_{fd}\beta(t) - iJ^*\alpha(t) - \frac{\kappa_f}{2}\beta(t) - i\epsilon_f(t).
\end{aligned}
\tag{3.1}
$$

$\Delta_{rd}\,(\Delta_{fd}) = \omega_{r(f)} - \omega_d$ is the detuning between the resonator frequency ω_r (band-pass center frequency ω_f) and the driving tone at frequency ω_d. J, and its complex conjugate J^*, represent the coupling strength between the readout resonator and the Purcell filter. κ_f is the Purcell filter bandwidth and γ_a is the non-radiative loss rate of the resonator. $\epsilon_f(t)$ is the electric field strength of the driving tone of frequency ω_d, which can be time-dependent for pulsed readout. Note that for simulation, the equations are written in the rotating frame $e^{-i\omega_d t}$ of a monochromatic readout drive frequency, which applies for a continuous readout drive tone. In addition, the three field amplitudes α, β, and ϵ_f are normalized such that $|\alpha|^2$ and $|\beta|^2$ represent the average photon number in the readout resonators and the Purcell filter, respectively. $|\epsilon_f|^2$ is normalized accordingly as well.

We find the steady-state response of the filter on the time scale longer than κ_f^{-1} by solving the equations of motion with the conditions $\dot{\alpha}(t) = 0$ and $\dot{\beta}(t) = 0$. For an ideal resonator, we assume the loss γ_a to be zero to simplify the expression. We find the analytical solution of the steady-state electric field inside the coupled Purcell-resonator system as

$$
\beta(\omega_d) = \frac{\Delta_{rd} \cdot \epsilon_f}{(i\Delta_{fd} + \frac{\kappa_f}{2})i\Delta_{rd} + |J|^2}.
\tag{3.2}
$$

The transmitted field strength at the output of the Purcell filter is given by $\gamma_{tr} = \beta\kappa_f/2$. We calculate γ_{tr} as a function of the drive frequency ω_d, which can then be used to fit the results in either HFSS simulation or readout spectroscopy measurements.

To calculate the dynamic response of the field inside the readout resonator, we only assume a quasi-steady state for the Purcell filter, i.e., $\dot{\beta}(t) = 0$, and solve for $\beta(t)$ in Eq. (3.1) as a function of $\alpha(t)$,

$$
\beta(t) = \frac{-iJ\alpha(t) - i\epsilon_f}{\kappa_f/2 + i\Delta_{fd}}.
\tag{3.3}
$$

We then substitute the expression back into the full equation of motion in Eq. (3.1) and organize the terms in the following form:

$$\dot{\alpha}(t) = -i(\Delta_{rd} + \delta\omega_r)\alpha(t) - \frac{\kappa_r}{2}\alpha(t) - i\epsilon_r, \tag{3.4}$$

with an effective linewidth of the readout resonator κ_r, a shift $\delta\omega_r$ of the bare resonator frequency due to the coupling to the Purcell filter, and an effective drive amplitude inside the readout resonator ϵ_r. These parameters are given by

$$
\begin{aligned}
\kappa_r &= \frac{4|J|^2}{\kappa_f}\frac{1}{1+(2\Delta_{fd}/\kappa_f)^2}, \\
\delta\omega_r &= -\frac{|J|^2 \cdot \Delta_{fd}}{(\kappa_f/2)^2 + \Delta_{fd}^2} = -\frac{\Delta_{fd}}{\kappa_f}\kappa_r, \\
\epsilon_r &= \frac{iJ}{\kappa_f/2 + i\Delta_{fd}}\epsilon_f.
\end{aligned}
\tag{3.5}
$$

Therefore, the qubit excitation decaying through the resonator could be interpreted as driving the resonator at $\omega_d = \omega_q$ with a decay rate

$$\kappa_q = \frac{4|J|^2}{\kappa_f}\frac{1}{1+(2\Delta_{fq}/\kappa_f)^2}, \tag{3.6}$$

where $\Delta_{fq} = \omega_f - \omega_q$. The qubit Purcell limit on the T_1 decay is given in [77]

$$\Gamma_{1,\text{Purcell}} \approx \kappa\frac{g^2}{(\omega_r - \omega_q)^2}. \tag{3.7}$$

With $\kappa = \kappa_q$, we find,

$$\Gamma_{1,\text{Purcell}} \approx \frac{4|J|^2\kappa_f}{\kappa_f^2 + 4(\omega_f - \omega_q)^2}\frac{g^2}{(\omega_r - \omega_q)^2}. \tag{3.8}$$

Therefore, $\Gamma_{1,\text{Purcell}}$ can be engineered to be significantly longer than the case with the readout resonator directly coupled to the feedline with a rate κ, while the dispersive shift χ can be sufficiently large to enable fast readout.

Multiple resonators can be coupled within the bandwidth of a single Purcell

filter by choosing a corresponding resonance frequency ω_f and linewidth κ_f. Designs with a common Purcell filter provide various advantages in scalability compared to designs having one Purcell filter for each readout resonator. The main advantage is that it reduces the physical footprint on the chip, freeing up space that can instead be used to route control lines to further avoid drive crosstalk. The filter resonator is incorporated into the feedline in a straightforward fashion as a $\lambda/2$ resonator with a capacitor at each end. The fabrication accuracy of the resonator frequencies is less crucial to readout performance since the bandwidth of the Purcell filter κ_f is large, so the filter is insensitive to a small drift in resonator frequency.

One main concern about the common Purcell filter is that the crosstalk between the readout resonators could increase: the measurement could induce phase errors on the untargeted qubits with resonators coupled to the same filter. This effect could be mitigated with pulse schemes to compensate for the phase shift. At the same time, one could overcome this by designing the circuit such that qubits are separated into different physical filter lines depending on their designation, e.g., ancilla or data qubit.

3.1.2 Multiplexed Readout Implementation

We now demonstrate the operation of a 3-qubit device with a common Purcell filter. The fabricated circuit schematic is shown in Fig. 3.2. The device consists of three fixed-frequency transmon qubits [66] with transition frequencies $\omega_{q_i}/2\pi$ at 5.36, 5.40, and 5.46 GHz for $i = 1, 2, 3$, respectively. There is no direct coupling element between the qubits. Each qubit is coupled with a strength g_i to a readout resonator of frequency $\omega_{r_i}/2\pi = 6.45, 6.61$, and 6.74 GHz. The three resonators are coupled with a strength J_i to a common Purcell filter that is embedded in the readout feedline [53]. The Purcell-to-resonator coupling rates $J_i/2\pi$ are designed to be at 60 MHz, while the qubit-resonator coupling rates $g_i/2\pi$ are much larger, about 250 MHz. The Purcell filter is centered at $\omega_f/2\pi = 6.726$ GHz with a linewidth of $\kappa_f/2\pi = 820.9$ MHz. Further detail about the experimental setup can be found in **Paper A**.

The initial characterization includes the measurement of the forward scattering parameter S_{21} of the three resonators and the Purcell filter as a function of driving frequency. The results are shown in Fig. 3.3 and fitted with Eq. (3.2). The measured and extracted parameters of the sample used in our
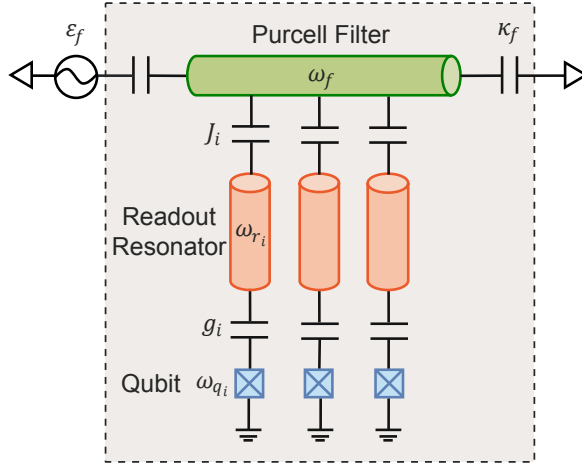
Figure 3.2: Circuit schematic of the common-mode Purcell filter. The Purcell filter is a $\lambda/2$ coplanar waveguide resonator centered at ω_f, defined by a capacitor on each side. The filter is embedded in the readout feedline, and driven by the field ϵ_f. The output capacitance, represented by the Purcell-filter linewidth κ_f, is around an order of magnitude larger than the input capacitance such that the signal is guided towards the output port to measure transmission. Multiple resonators of resonant frequency ω_{r_i} couple to the Purcell filter with strength J_i within the filter bandwidth. The individual resonators are capacitively coupled with strength g_i to the qubits with transition frequency ω_{q_i}.

Parameters		R1	R2	R3	PF
Resonator frequency	$\omega_r/2\pi$ (GHz)	6.454	6.606	6.744	6.726
Effective linewidth	$\kappa_r \left(\kappa_f\right)/2\pi$ (MHz)	16.6	11.0	12.4	820.9
Readout-Purcell coupling	$J/2\pi$ (MHz)	70.1	57.1	60.6	

Table 3.1: Measured resonator parameters for the Purcell filter and the three readout resonators.

experiment are listed in Tables 3.1 and 3.2. The qubit relaxation time T_1 is Purcell-limited according to the calculation based on Eq. (3.7), which is lower than the design value and what is normally achieved in our lab [114], due to a shift in qubit frequencies during the fabrication process. The Purcell rates are thus overestimated due to the relatively small detunings between the qubits

Parameters		Q1	Q2	Q3
Qubit frequency	$\omega_q/2\pi$ (GHz)	5.358	5.395	5.456
Qubit anharmonicity	$\eta/2\pi$ (MHz)	-192	-198	-199
Qubit-readout coupling	$g/2\pi$ (MHz)	231	235	263
Dispersive shift	$\chi/2\pi$ (MHz)	7.3	6.3	7.0
T_1 Purcell limit	T_P (μs)	1.8	3.06	2.26
Average relaxation time	$\overline{T}_1$ (μs)	3.6	6.2	3.8
Average Ramsey decay time	$\overline{T}_2^*$ (μs)	1.7	1.7	2.0
Average Echo decay time	$\overline{T}_2^e$ (μs)	1.8	2.1	2.2
Thermal population	$P_{th}(\%)$	1.9%	2.0%	1.6%
Single-qubit gate fidelity	$\mathcal{F}_{1Q}(\%)$	99.04%	99.59%	99.48%

Table 3.2: Measured qubit parameters, coherence properties, and single-qubit performance for the three qubits.

and the resonators [107].

3.2 Exploiting Higher Energy Levels

Qubit-excited-state decay is a major error source during readout. To minimize such an error, qubit-state measurements must be performed in the shortest possible time [54, 94]. We implement a shelving scheme that exploits the higher energy qubit levels [65, 95, 106, 115–119]. The pulse scheme is shown in Fig. 3.4(a); a π_{12} and a π_{23} pulse are applied consecutively prior to the readout pulse so that the qubit population originally in the $|1\rangle$ state is transferred to the $|3\rangle$ state before readout. Thus, the qubit population that was in $|1\rangle$ will take a longer time to decay to $|0\rangle$ as the main relaxation channel is through cascading single-photon emission down the energy ladder, as illustrated in Fig. 3.4(b).

To quantify the possible decrease in error due to the shelving technique, we measure the population of the ground state $p_0(t)$ as a function of the delay time t when the qubit is prepared in $|0\rangle$, $|1\rangle$, $|2\rangle$, and $|3\rangle$ ($t = 0$ means that there is no delay between the last shelving pulse and the readout pulse). State preparation and measurement (SPAM) errors are mitigated by applying the inverse of the assignment matrix to the measurement results [120]. Then, the most probable physical state is acquired with a maximum likelihood estimator [121]. The duration of the readout pulse τ_r is minimized by optimizing the readout-pulse amplitude without introducing significant readout-induced mix-
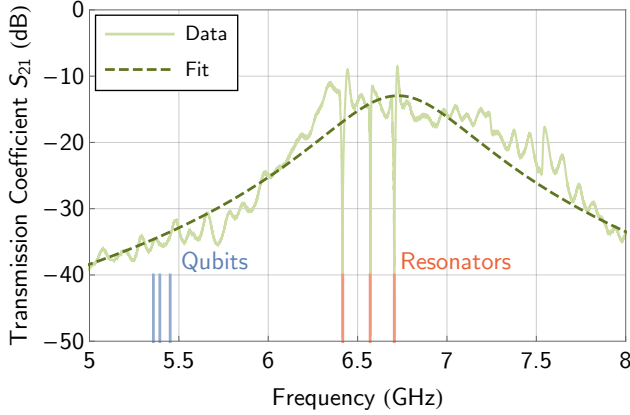
Figure 3.3: Transmission coefficient S_{21} as a function of the driving frequency ω_d. The data is shown as the solid line and the fit to Eq. (3.2) is the dashed line, where the resonator-Purcell coupling J is neglected. The vertical lines indicate the frequencies of the qubits (blue) and the readout resonators (red). The qubits are outside the passband of the Purcell filter and are therefore protected from relaxation into the environment.

ing that contributes to the readout errors [122, 123]. The duration of our optimized readout pulse [124–126] is $\tau_r = 140\,\text{ns}$. The data for Qubit 2 is shown in Fig. 3.4(c). We find that when the qubit is prepared in $|1\rangle$, the $|1\rangle$-state population decays during the readout by an amount $\epsilon = 1 - e^{-\tau_r/T_{01}} = 2.24\,\%$, with relaxation time $T_{01} = 6.18\,\mu\text{s}$, giving a significant contribution to the readout error.

To calculate the population $p_i(t)$ in the $|i\rangle$ state we write down the following rate equations:

$$\begin{aligned}
\dot{p_0}(t) &= p_1(t)/T_{01} + p_2(t)/T_{02} + p_3(t)/T_{03}, \\
\dot{p_1}(t) &= -p_1(t)/T_{01} + p_2(t)/T_{12} + p_3(t)/T_{13}, \\
\dot{p_2}(t) &= -p_2(t)/(T_{12} + T_{02}) + p_3(t)/T_{23}, \\
\dot{p_3}(t) &= -p_3(t)/(T_{23} + T_{13} + T_{03}),
\end{aligned} \tag{3.9}$$

where T_{ij} is the relaxation rate from the $|j\rangle$ to the $|i\rangle$ state as illustrated in the level diagram of Fig. 3.4(b). In principle, the anharmonicity of the transmon
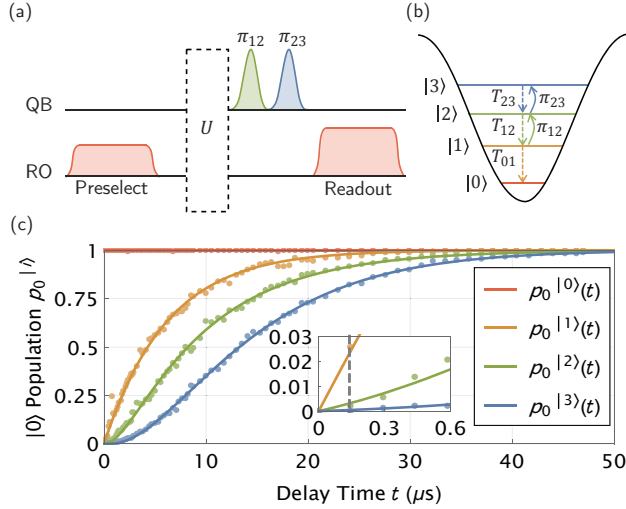
Figure 3.4: Schematics and implementation of the shelving technique. (a)
A π_{12} and a consecutive π_{23} pulse are inserted between any experimental sequence
U and the readout pulse. **(b)** Qubit population can be transferred to the desired
energy level with consecutive π_{ij} pulses. The population in state $|j\rangle$ decays to $|i\rangle$
with a rate $1/T_{ij}$. **(c)** The ground state $|0\rangle$ population p_0 of qubit Q_2 is plotted as a
function of the delay time t after the transmon is initially prepared in $|0\rangle$, $|1\rangle$, $|2\rangle$, or
$|3\rangle$. The delay time t is counted from the end of the last qubit shelving pulse in the
sequence. Points represent experimental data for Q_2 while continuous lines show fits
of the data according to the solutions of the expanded rate equations including all
non-sequential rates [115], which are given by Eq. (3.13) and Eq. (3.14). The inset
shows the population at short time scales with the dashed line marking the duration
$\tau_r = 140\,\text{ns}$ of the readout pulse.

is sufficient such that non-sequential decay through multi-level channels is
exponentially suppressed. For example, the contribution of direct decay from
$|2\rangle$ to $|0\rangle$ is found to be two orders of magnitude smaller than that from $|2\rangle$ to
$|1\rangle$ [115]. For simplicity, we initially neglect the non-sequential decay terms
and solve for the evolution of any $|i\rangle$-state population as a function of time t
when the qubit is initialized in the $|j\rangle$ state, denoted as $p_i^{|j\rangle}(t)$. Specifically,
we first solve for $p_0^{|2\rangle}(t)$ and assume $p_2^{|2\rangle}(0) = 1$ in the absence of any error
and neglect the effect of higher-energy levels by using the initial conditions

$p_0^{|2\rangle} = p_1^{|2\rangle} = p_3^{|2\rangle} = 0$. We find:

$$p_0^{|2\rangle}(t) = 1 - \frac{T_{01}\, e^{-t/T_{01}}}{T_{01} - T_{12}} + \frac{T_{12}\, e^{-t/T_{12}}}{T_{01} - T_{12}}, \tag{3.10}$$

where $T_{12} \approx \frac{1}{2}T_{01}$ for typical transmon parameters [115, 127]. The second and third terms in Eq. (3.10) are two decaying functions with opposite signs, hence the net result is no longer purely exponential. We also solve the rate equations of the system in Eq. (3.9) for $p_0^{|3\rangle}$, when the qubit is prepared in $|3\rangle$, with the initial conditions $p_0^{|3\rangle} = p_1^{|3\rangle} = p_2^{|3\rangle} = 0$, and find the following:

$$
\begin{aligned}
p_0^{|3\rangle}(t) = 1 &- \frac{T_{01}{}^2\, e^{-t/T_{01}}}{(T_{01} - T_{12})(T_{01} - T_{23})} \\
&+ \frac{T_{12}{}^2\, e^{-t/T_{12}}}{(T_{01} - T_{12})(T_{12} - T_{23})} \\
&- \frac{T_{23}{}^2\, e^{-t/T_{23}}}{(T_{01} - T_{23})(T_{12} - T_{23})}.
\end{aligned}
\tag{3.11}
$$

This equation contains a combination of exponential decays with different signs as well. Fig. 3.4(c) shows the measured population $p_0^{|1\rangle}$, $p_0^{|2\rangle}$ and $p_0^{|3\rangle}$ as a function of the delay time. We first used Eqs. (3.10) and (3.11) to fit the data. However, at short timescales, the theory does not describe well the data (see the dashed lines in Fig. 3.5). We then perform the same derivations while including all non-sequential decays in the rate equations. To calculate the population $p_i(t)$ in the $|i\rangle$ state we use the full rate equations in Eq. (3.9) without neglecting any term. The full solution for $p_0^{|2\rangle}(t)$ and $p_0^{|3\rangle}(t)$ are the following:

$$p_0^{|1\rangle}(t) = 1 - \Gamma_{12}, \tag{3.12}$$

$$p_0^{|2\rangle}(t) = 1 - \frac{\Gamma_{12}\, e^{-\Gamma_{01}t} + (\Gamma_{02} - \Gamma_{01})\, e^{-(\Gamma_{02} + \Gamma_{12})t}}{\Gamma_{01} - \Gamma_{02} - \Gamma_{12}}, \tag{3.13}$$
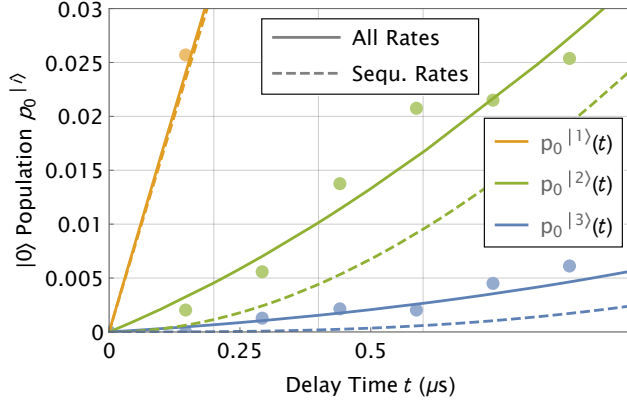
Figure 3.5: Higher energy levels decay measurement and fit, at short time scale. The ground state $|0\rangle$ population p_0 is plotted as a function of the delay time t after the transmon is initially prepared in $|0\rangle$, $|1\rangle$, $|2\rangle$, or $|3\rangle$. The delay time t is counted from the end of the last qubit shelving pulse in the sequence. Points represent experimental data for Qubit 2. The continuous lines show fits of the data according to the solutions of the expanded rate equations including all non-sequential rates shown in Eqs. (3.12-3.15) [115], while the dashed lines represent the fits with only sequential rates included in the equation.

$$
\begin{aligned}
p_0^{|3\rangle}(t) = 1 &- \frac{(-\Gamma_{12}\Gamma_{23} + \Gamma_{13}\delta_0)\, e^{-\Gamma_{01}t}}{\delta_0\delta_1} \\
&+ \frac{(-\Gamma_{01} + \Gamma_{02})\Gamma_{23}\, e^{-(\Gamma_{02}+\Gamma_{12})t}}{\delta_0(\delta_2 + \Gamma_{23})} \\
&- \frac{[(\Gamma_{01} + \Gamma_{03})\,\delta_2 + (\Gamma_{02} - \Gamma_{03})\Gamma_{23}]\, e^{-\delta_3 t}}{\delta_1(\delta_2 + \Gamma_{23})},
\end{aligned}
\tag{3.14}
$$

where $\Gamma_{ij} = 1/T_{ij}$ and

$$
\begin{aligned}
\delta_0 &= \Gamma_{01} - \Gamma_{02} - \Gamma_{12}, \\
\delta_1 &= -\Gamma_{01} + \Gamma_{03} + \Gamma_{13} + \Gamma_{23}, \\
\delta_2 &= -\Gamma_{02} + \Gamma_{03} - \Gamma_{12} + \Gamma_{13}, \\
\delta_3 &= \Gamma_{03} + \Gamma_{13} + \Gamma_{23}.
\end{aligned}
\tag{3.15}
$$

Equations (3.12-3.15) are used to fit the data in Fig. 3.4(c) with a higher precision, as shown in Fig. 3.5. It is clear that adding the non-sequential terms improves the fitting at low time scales (see continuous lines in Fig. 3.5)[115]. We find excellent agreement between the data and the full model, and extract the following relaxation times: $T_{01} = 6.55\,\mu\mathrm{s}$, $T_{12} = 5.27\,\mu\mathrm{s}$, $T_{23} = 5.10\,\mu\mathrm{s}$, $T_{02} = 50\,\mu\mathrm{s}$, $T_{13} = 125\,\mu\mathrm{s}$, and $T_{03} = 350\,\mu\mathrm{s}$.

For Qubit 2, we find that the readout error from the $|1\rangle$ state is reduced from $2.24\,\%$ to $0.057\,\%$ after the application of a π_{12} pulse, and to $8.7\times10^{-4}\,\%$ after a π_{23} pulse. This is calculated by taking the difference between $p_0^{|2\rangle}(t = \tau_r)$ and $p_0^{|2\rangle}(0)$ in Fig. 3.4(a). The remaining error is equivalent to the decay error of a qubit with $T_{01} = 85.8\,\mu\mathrm{s}$ using the standard readout method, achieving an order-of-magnitude improvement. For a longer-lived qubit, the percentage of decay errors that can be suppressed with shelving continues to grow closer to unity [119]. However, other error contributions will likely become more prominent at this level.

Before performing readout calibration, we optimize the parameters of the π_{12} and π_{23} pulses similar to the standard method developed for the π_{01} pulse. The pulses have a cosine envelope with lengths set to be $50\,\mathrm{ns}$ as a starting point. We first prepare the qubit in $|1\rangle$ and conduct Rabi and Ramsey-like experiments between the higher energy levels to optimize the amplitude and frequency of the drive pulse. For shorter pulse lengths a proper derivative removal by adiabatic gate (DRAG) [81, 82] needs to be calibrated for the π_{12} and π_{23} pulses as well.

With the state-preparation pulses calibrated, we acquire the responses of the readout resonator when the qubit is prepared in $|0\rangle$, $|1\rangle$, $|2\rangle$, and $|3\rangle$, respectively, illustrated in Fig. 3.6(a). We plot the in-phase and quadrature parts of the spectroscopy result, as shown in Fig. 3.6(b).

3.3 Two-State Readout with a Primary Tone

For the two-state readout, we only use one tone, which is referred to as the primary tone, for optimal readout performance. Later, we introduce a secondary tone to perform three-state readout. We start by fine-tuning the readout frequency of the primary tone to maximally separate the 2D in-phase and quadrature (IQ) histograms corresponding to the $|0\rangle$ and $|1\rangle$ states, as shown in Fig. 3.7(a). Higher energy levels are indistinguishable from $|1\rangle$ in

(a)

(b)
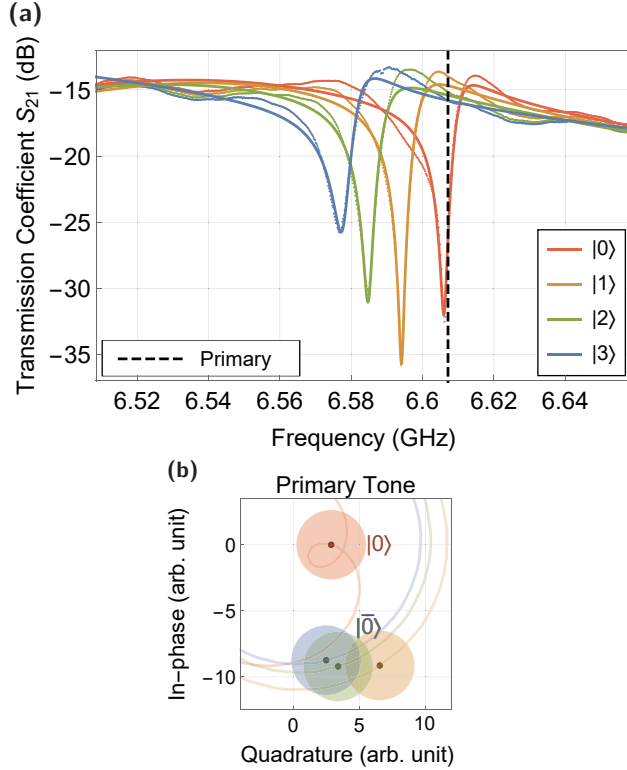
Figure 3.6: Transmission coefficient S_{21} as a function of the driving frequency ω_d centered around Resonator 2. (a) Qubit-state-dependent transmission S_{21} of resonator R2 when Qubit 2 is prepared in $|0\rangle, |1\rangle, |2\rangle$, and $|3\rangle$, respectively. The colored dots represent the measured data while the solid lines show the fitted function. The vertical dashed lines represent the optimal readout frequency for the primary tone.**(b)** Estimated readout response of the primary tone at its optimal frequency. The solid lines represent the in-phase and quadrature data shown in (a). The disks of respective color represent the estimated Gaussian envelope of the signal taking into account the added thermal noise.

this configuration, and we can only distinguish between $|0\rangle$ and $|\bar{0}\rangle$ (NOT $|0\rangle$). To calibrate the readout, we prepare the qubit in either $|0\rangle$ or $|1\rangle$ and add the π_{12} and π_{23} pulses to transfer the $|1\rangle$-state population to the $|3\rangle$ state before the readout, as illustrated in Fig. 3.4(a). To discard the results
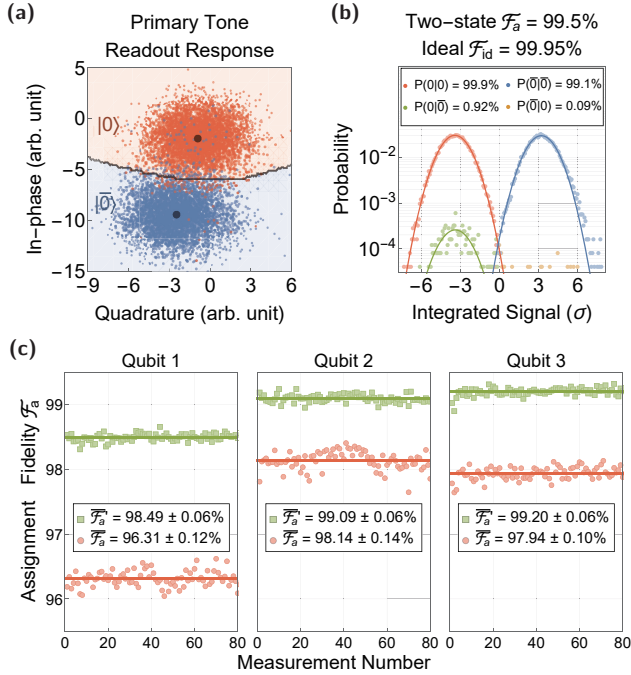
Figure 3.7: Single-shot readout results of discriminating between $|0\rangle$ and $|\overline{0}\rangle$. **(a)** Integrated readout signal in the IQ plane with Qubit 2 prepared in $|0\rangle$ and $|1\rangle$. With the consecutive π_{12} and π_{23} pulses implemented prior to a 140 ns readout, we distinguish between $|0\rangle$ and $|\overline{0}\rangle$ (NOT $|0\rangle$). **(b)** The IQ-plane signals in (a) are projected onto an optimal axis, and the resulting histogram is fitted with a Gaussian distribution. The horizontal axis is normalized by the standard deviation σ. The calculated assignment fidelity $\mathcal{F}_a$ and ideal fidelity $\mathcal{F}_{id}$ are shown above the plot. The conditional probabilities $P(i|j)$ represent the probabilities of measuring state $|i\rangle$ given that the qubit is prepared in state $|j\rangle$. **(c)** Simultaneously measured single-shot readout assignment fidelities for the three qubits with $(\overline{\mathcal{F}_a'})$ and without $(\overline{\mathcal{F}_a})$ the application of the π_{12} and π_{23} pulses. The error statistics are calculated from the standard deviation of the measured set.

for which the initial state is not $|0\rangle$, we include a preselection pulse, i.e., an additional readout measurement before the sequence starts [54, 128]. Through this preselection procedure, thermal and residual populations in the qubits are filtered from the outcomes.

We perform simultaneous readout of all three qubits and calculate the single-qubit readout assignment fidelity $\mathcal{F}_a = 1 - [P(0|\overline{0}) + P(\overline{0}|0)]/2$, where $P(i|j)$ is the classification probability, i.e., the probability that the $|i\rangle$ state is assigned given that the $|j\rangle$ state is initially prepared. This measure of readout fidelity takes all the error contributions into account, including imperfect state preparation before the readout sequence. The assignment fidelity for 80 repetitions, each containing 50,000 shots, is shown in Fig. 3.7(c) with $(\overline{\mathcal{F}_a'})$ and without $(\overline{\mathcal{F}_a})$ implementation of the shelving technique. The data demonstrate a reduction in the overall error rate by 57 % on average for the three qubits with the introduced readout scheme. We also compute the ideal readout fidelity $\mathcal{F}_{id}$ by integrating the overlapping area of the Gaussian probability distributions after projecting the IQ data onto an optimal axis [129]:

$$\mathcal{F}_{id} = \frac{1}{2}\left[1 + \mathrm{erf}\left(\sqrt{\frac{SNR^2}{8}} \right) \right], \tag{3.16}$$

where the signal-to-noise ratio is

$$SNR = \frac{\left| \langle S_0 \rangle - \langle S_{\overline{0}} \rangle \right|}{\sigma_{S_0}}, \tag{3.17}$$

with S_i being the set of measurement outcomes and $\sigma_{S_0}^2$ being the variance of the data set. For Qubit 2, the best assignment fidelity is 99.5 % while the ideal fidelity exceeds 99.95%; see Fig. 3.7(b) for detailed histograms. In particular, the readout errors associated with the $|0\rangle$- and the $|\overline{0}\rangle$-state are $\epsilon_{|0\rangle} = P(\overline{0}|0) = 0.09\%$ and $\epsilon_{|\overline{0}\rangle} = P(0|\overline{0}) = 0.92\%$, respectively. The error from qubit decay during readout contributes to 0.03% of the $|\overline{0}\rangle$-state error $\epsilon_{|\overline{0}\rangle}$. This suggests that the fidelity is predominantly limited by other sources of error. The most dominant source of error is due to imperfect state preparation and application of the shelving pulses [54]. This contribution is at least 58% of the $\epsilon_{|\overline{0}\rangle}$ error and is calculated based on the coherence limit of the qubit and serves as a lower bound. The measurement-induced mixing is the next dominant source of error. We estimate this contribution to be at most 10% of $\epsilon_{|\overline{0}\rangle}$, since this affects both $\epsilon_{|0\rangle}$ and $\epsilon_{|\overline{0}\rangle}$ equally [122, 123].

3.4 Three-State Readout with Two Tones

As shown in Fig. 3.6, choosing the optimal readout frequency to attain the best two-state assignment fidelity leaves other higher-energy states indistinguishable from each other. However, the information of the $|2\rangle$-state population is crucial to detect leakage errors during gate calibrations and algorithms [32]. To access this information, we introduce an additional readout pulse with a readout frequency, referred to as secondary tone, that maximizes the separation between $|1\rangle$ and $|2\rangle$. This pulse is multiplexed with the primary pulse to perform the readout measurements simultaneously.

We also use the π_{12} and π_{23} pulses to implement the shelving scheme. As the initial $|1\rangle$-level population is transferred to the $|3\rangle$ state and the $|2\rangle$-population is transferred to the $|1\rangle$ state, an error in $|1\rangle$-state assignment will occur if a cascade of decays happens from $|3\rangle$ to $|1\rangle$. The contribution of decay error during readout is reduced, leading to an improvement in assignment fidelity. To quantify the improvement, we need to solve Eq. (3.9) for the evolution of population $p_1^{|3\rangle}(t)$. The analytical solution is

$$
\begin{aligned}
p_1^{|3\rangle}(t) = & \frac{T_{01}{}^2\, e^{-t/T_{01}}}{(T_{01} - T_{12})(T_{01} - T_{23})} \\
& - \frac{T_{01}\, T_{12}\, e^{-t/T_{12}}}{(T_{01} - T_{23})(T_{12} - T_{23})} \\
& + \frac{T_{01}\, T_{23}\, e^{-t/T_{23}}}{(T_{01} - T_{12})(T_{12} - T_{23})}.
\end{aligned}
\tag{3.18}
$$

With the qubit being in the $|3\rangle$ state ($p_3^{|3\rangle}(0) = 1$), the effective population accumulation in $|1\rangle$ after a readout time of $\tau_r = 140$ ns is $0.035\,\%$. This is two orders of magnitude smaller than the error from a direct decay of the $|2\rangle$-state population with rate $1/T_{12}$, corresponding to $2.65\,\%$. Therefore, the contribution to the three-state readout error should be reduced by a similar factor.

The secondary tone is tuned up in the presence of the primary pulse. An initial estimate for the secondary readout frequency is where the $|1\rangle$- and $|2\rangle$-state responses are maximally separated in the IQ-plane. Similar to the primary tone, we find the readout frequencies that maximize $|1\rangle$-$|2\rangle$ separation for the secondary tone, as shown in Fig. 3.8. As the readout tones are

(a)

(b)
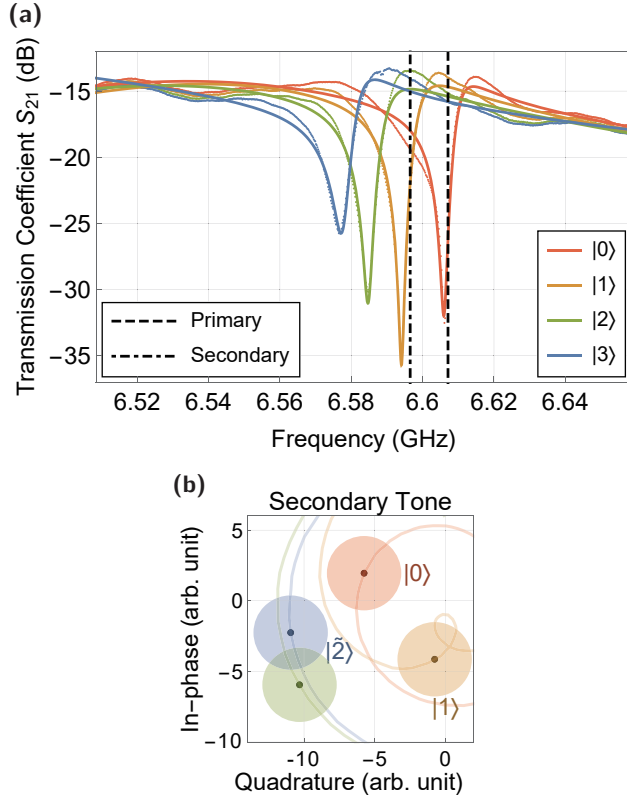
Figure 3.8: Readout Frequency Optimization for the Secondary tone (a)
The vertical lines represent the optimal readout frequencies for the primary (dashed
line) and secondary tone (dash-dotted line). **(b)** Estimated readout response of the
secondary tone at optimal frequency.

multiplexed into a single pulse, the frequency and phase of the secondary tone
are fine-tuned to minimize the effect on the measurement performance of the
primary tone.

We then fine-tune this frequency such that $|0\rangle$ and $|3\rangle$ are distinguishable
from each other as well. After optimization, the two readout pulses are typ-
ically a few MHz apart and are multiplexed in a single waveform for the
readout. The transmitted signal is then processed with standard multiplexed
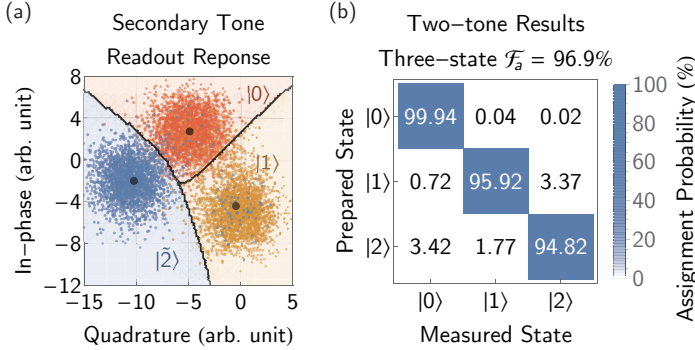
Figure 3.9: Single-shot readout results for discriminating between the $|0\rangle$, $|1\rangle$, **and** $|2\rangle$ **state. (a)** Integrated single-shot readout signal of the secondary tone for Qubit 2. The $|0\rangle$ and $|1\rangle$ states are distinguishable from the rest, while $|2\rangle$ and $|3\rangle$ have significant overlap, and are therefore being combined into a single classification: $|\tilde{2}\rangle$. The frequency of the primary tone is identical to that shown in Fig. 3.7, which maximizes the distinction between $|0\rangle$ and $|\bar{0}\rangle$. The dots indicate the centers of the Gaussian distributions. **(b)** Three-state assignment matrix with the two-tone readout for Qubit 2, reconstructed using a neural network. Note that the most significant error contributions in the two-tone readout are the misclassification between $|2\rangle$ and $|0\rangle$ as well as that between $|1\rangle$ and $|2\rangle$.

readout techniques [94]. We obtain two complex voltages after signal integration, each containing a pair of in-phase and quadrature values. Overlap errors are then filtered by comparing the results in post-processing. The response of the secondary tone when Qubit 2 is prepared in $|0\rangle$, $|1\rangle$, $|2\rangle$, and $|3\rangle$, with 50,000 repetitions per state, is shown in Fig. 3.9(a). Since $|2\rangle$ and $|3\rangle$ are indistinguishable, we combine the results together and relabel them as the $|\tilde{2}\rangle$-state.

3.4.1 State Discrimination

We then formulate two methods to combine the results from the primary and secondary readout pulses to reconstruct the population initially prepared in $|0\rangle$, $|1\rangle$, and $|2\rangle$. The first method is a truth table (see Table 3.3) that takes the individual measurement results from the two tones as a pair of input values. There exists a unique initial state that is compatible with both results. For example, if the primary result is $|\bar{0}\rangle$ and the secondary result is $|1\rangle$, then the

Primary Result	Secondary Result	Before Readout	Initial State
$\vert 0 \rangle$	$\vert 0 \rangle$	$\vert 0 \rangle$	$\vert 0 \rangle$
$\vert \bar{0} \rangle$	$\vert 1 \rangle$	$\vert 1 \rangle$	$\vert 2 \rangle$
$\vert \bar{0} \rangle$	$\vert \tilde{2} \rangle$	$\vert 2 \rangle$	$\vert 1 \rangle$
$\vert 0 \rangle$	$\vert \bar{0} \rangle$	Overlap Error	
$\vert \bar{0} \rangle$	$\vert 0 \rangle$		

Table 3.3: Truth table of the selection rule for the two-tone readout. The first two columns are the discrimination results from the two readout tones, respectively. There is a unique initial state if the results agree with each other. Otherwise, the shots where the two readout results disagree will be counted towards overlap error and discarded.

initially prepared state must be $\vert 2 \rangle$. In case these two results cannot reach a common decision due to overlap error, the measurement is discarded.

The second method to discriminate the qubit state utilizes a feedforward neural network (FNN) that was specifically developed for multiplexed readout [130] and treats the two data sets as a single system. The input to the neural network combines the in-phase ($I[n]$) and quadrature ($Q[n]$) data from the nth integrated signal of the two tones into a four-element vector $\{I_1[n], Q_1[n], I_2[n], Q_2[n]\}$. After being trained with a calibration data set, the neural network is able to classify two-tone results and give the initial qubit state as the output.

We utilize a feedforward neural network (FNN) with two hidden layers to discriminate the qubit state using the combined two-tone results. The choice of using an FNN over other methods such as support-vector machine (SVM) or non-linear support-vector machine (NSVM) is justified by the fact that an FNN could achieve greater performance when discriminating more than two states as well as better scalability [130]. The FNN is also capable of transfer learning, where retraining of the network during future re-calibration of the system is significantly more efficient [131]. On the other hand, an SVM or NSVM will need to be retrained from scratch every time. The advantage of using FNN is significant enough to warrant a wider application [130, 132, 133].

The network is implemented with Wolfram Mathematica. The input layer contains four nodes corresponding to the in-phase and quadrature components of the two-tone results, $\{I_1[n], Q_1[n], I_2[n], Q_2[n]\}$, of each individual

single-shot measurement n. The first hidden layer contains 16 nodes, while the second layer has 8 nodes. Each node, comprised of the hidden layers, is filtered by a scaled exponential linear unit (SELU), which acts as the nonlinear activation function. Finally, the output layer contains three nodes, representing the probability of the qubit being in state $|0\rangle$, $|1\rangle$, and $|2\rangle$, respectively. We specify an epoch of 100 and a learning rate of 0.0005 with a batch size of 64 as a starting point. The network is then trained with 8000 samples and validated by 2000 samples.

The resulting assignment matrix, shown in Fig. 3.9(b), demonstrates an assignment fidelity of 96.9 % for the three-state readout. This result shows a significant improvement over the average 94.2 % assignment fidelity that we find using only a single readout pulse at an optimal readout frequency to distinguish between $|0\rangle$, $|1\rangle$, and $|2\rangle$, with the overall error rate reduced by 47 %. The amount of suppression is achieved with the neural network that consistently outperforms the truth table by 13 % in overall error rate reduction.

A feature of the resulting assignment matrix is that the population originally in $|2\rangle$ has a higher probability of being misidentified as $|0\rangle$ than as $|1\rangle$, which is due to the shelving technique. Since the initial $|2\rangle$-state population is transferred to $|1\rangle$ before measurement, decaying to the ground state is more likely than the excitation back to higher energy levels.

3.4.2 Readout Crosstalk

We also investigate the effect of increased photon population in the resonators due to the secondary tone. A large photon number leads to significant measurement-induced mixing and readout crosstalk that contribute to the overall readout error [94, 134]. We optimize the readout amplitude such that readout errors due to measurement-induced mixing remain small with the addition of the secondary tone. To investigate readout crosstalk, we determine the measurement-induced dephasing with and without the secondary tone [94]. The results are shown in Fig. 3.10. We find that the probabilities of a phase error in untargeted qubits are a factor of three larger on average due to the increase in photon number. Mitigation strategies may be required if this contribution becomes significant for error-correction algorithms.

In the design of future devices, qubits could be grouped into physically separated readout lines depending on their designation, e.g., ancilla or data qubits,
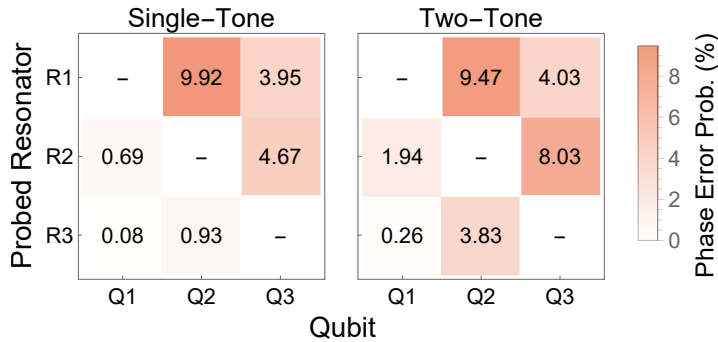
Figure 3.10: Measurement-induced dephasing matrix for single-tone and two-tone readout. Each element represents the qubit dephasing while a pulse is targeting one of the readout resonators (R1, R2, or R3). Note that for the two-tone case, resonator R1 was not driven by an additional tone, so that it served as a benchmark measurement.

and whether their measurements occur simultaneously. Moreover, the induced crosstalk could be further mitigated with other techniques such as machine-learning algorithms for discrimination and readout pulse shaping [130, 132, 135].

3.5 TWPA Performance Characterization

To achieve high-fidelity readout, quantum-limited amplifiers [136] with a high gain are desired. They are typically built as superconducting nonlinear oscillators or transmission lines and have demonstrated high gain with near-quantum-limited noise performance [137–141], becoming an essential part of the circuit Quantum Electrodynamics (cQED) [142] toolbox. While Josephson parametric amplifiers (JPAs) have shown high gain and near-quantum-limited noise performance [108, 143–149], they typically have a high gain over a narrow band, making them unsuitable for multiplexed readout in large-scale quantum computers.

The capability of quantum-limited noise performance and a high gain in a wide band is provided by the travelling-wave parametric amplifier (TWPA) [150–152]. The basic principle for amplification of the TWPA is based on frequency-mixing between a weak signal and a strong wave, the pump, when they co-
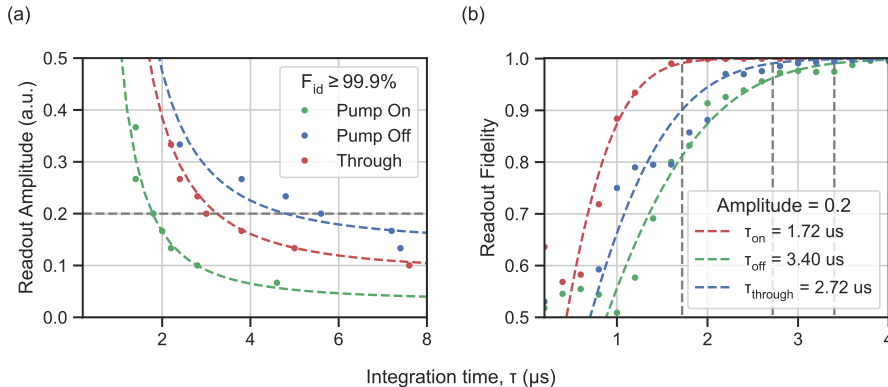
Figure 3.11: Qubit readout fidelity as a function of measurement time and readout amplitude. **(a)** Readout amplitude as a function of optimal integration duration using the TWPA with the pump on, off and with the through. The fit is of the function $A \propto 1/\sqrt{\tau}$. **(b)** Measured readout fidelity a as function of the integration time at a readout amplitude of 0.2, fitted with the error function of integration time τ with constants, $erf(\tau)$.

propagate through a nonlinear medium. When a phase-matching condition between the pump, the signal and the idler is fulfilled, this can result in exponential spatial growth of the signal amplitude.

We characterise a small footprint travelling-wave parametric amplifier (TWPA), with more details presented in **Paper F**. The TWPA is built with magnetically flux-tunable superconducting nonlinear asymmetric inductive elements (SNAILs) and parallel-plate capacitors. It implements three-wave mixing (3WM) with resonant phase matching (RPM), a small cutoff frequency for high gain per unitcell and impedance matching networks for large bandwidth impedance matching. The device has 200 unitcells and a physical footprint of only $1.1 \, \text{mm}^2$, yet demonstrating an average parametric gain of $19 \, \text{dB}$ over a $3 \, \text{GHz}$ bandwidth, with an average effective signal-to-noise ratio improvement of $10 \, \text{dB}$ and a clear speedup of qubit readout time.

In order to characterize the improved readout performance from the TWPA, we use the TWPA in the readout chain of a two-qubit device [114]. The device consists of two fixed-frequency transmon qubits [66] with transition frequencies $\omega_{q_i}/(2\pi)$ at 3.848 and $3.384 \, \text{GHz}$ for $i = 0$ and 1, respectively. The qubits are coupled via a tunable coupler element, which is not used in

this experiment, thus we can consider the qubits uncoupled.

Each qubit is coupled to a dedicated readout resonator of frequency $\omega_{r_i}/(2\pi) = $ 6.482 and 6.261 GHz with a strength $g/(2\pi) \approx 35$ MHz. The transmitted signal is measured through the readout line. We prepared the two qubits in $|0\rangle$ and $|1\rangle$ states respectively and characterised their single-shot readout performance with multiplexed readout. The measurement results of each qubit state are fitted with a Gaussian function and the ideal readout fidelity $\mathcal{F}_{\text{id}}$ was calculated as given in Eqs. (3.16) and (3.17) [129, 153].

We set a fixed readout pulse amplitude and sweep the integration time of the readout data acquisition process. The resulting readout fidelity for Qubit 1 with TWPA pump on, pump off and with a through is shown in Fig. 3.11(a) as an example. The total energy needed to achieve sufficient SNR is constant, which can be fitted with a functional form of $E \propto t \cdot A^2$, where A is the readout amplitude. The linecut at a fixed amplitude is shown in Fig. 3.11(b), where the data can be approximately fitted with a Gaussian error function to extract the dependence between the readout fidelity and integration time [54].

To reach an ideal readout fidelity of 99.9 %, it takes 2.8 µs of integration time with the through, while we only need 1.6 µs with the TWPA with the pump on, achieving almost a factor of two improvement in the readout speed. With the pump off, the time increases to 3.0 µs. It is worth noting that the performance is also more robust at the shorter integration time with the TWPA, indicating that a shorter readout time is achievable. With a device designed with a larger qubit-readout dispersive coupling strength χ, resonator decay strength κ, and incorporating Purcell filters, it is still possible to reduce the readout duration greatly [153].

3.6 Summary

In conclusion, we have demonstrated that exploiting the higher energy levels of the qubit together with the implementation of a secondary readout tone lead to an improved readout-assignment fidelity of 99.5 % (96.9 %) for two-state (three-state) discrimination within 140 ns of readout time, reducing the overall error rate by 57 % (47 %) compared to our baseline. This result could be further improved with the use of a quantum-limited parametric amplifier, as the one showcased in Section 3.5.

The proposed pulse scheme is straightforward to implement in any measurement sequence to improve readout fidelity. Our scheme is also fully compatible with quantum error correction algorithms that involve rapid, high-fidelity measurements of ancilla qubits. In the case of the surface code, single-qubit and measurement operations ideally do not disturb the encoded logical state stored on data qubits. The proposed techniques will only be performed on the ancilla qubits. Additionally, we envisage that to be fully utilized in the surface-code algorithm, the readout scheme could be accompanied by a reset protocol that targets higher-excited states after the measurement [96].

To further develop these readout techniques, more complex methods in the construction of the primary and secondary readout tones could be explored. Sophisticated deep neural-network methods could also be employed to aid state classification of the two-tone readout results [130]. The possibility to generalize these techniques to further boost fidelity for multiplexed readout is a promising prospect for the future investigation of quantum computing with superconducting qubits.

CHAPTER 4

Expanding Two-Qubit Gate Sets

To implement any gate-based sophisticated quantum algorithms, fast, high-fidelity two-qubit gates are instrumental, and the motivation for further development in this regard is of great interest to both academia and industry [154]. The pioneers in this endeavor demonstrated an adiabatic controlled-phase (CPHASE, CZ) gate in 2009 [155]. This specific type of adiabatic CPHASE gate was designed for a pair tunable transmon qubits, which were adjusted in frequency by applying magnetic flux through the respective qubit SQUID loop. To implement the CPHASE gate, the $|11\rangle$ and $|20\rangle$ levels of the two qubits were tuned close to resonance for a certain interaction time. To prevent always-on interaction between the qubits, a third coupling element was employed to mediate the interaction, which was a coplanar resonator in this case. The current limitation of this gate performance arises from the leakage to the qubits $|2\rangle$-level, which is inherent to this type of CZ gate due to the mechanism involving population exchange. Furthermore, the coherence of the tunable qubits also poses an upper bound on the gate fidelity due to increased sensitivity to flux noise. Therefore, finding alternatives to circumvent or mitigate these limitations is a highly active area of research [156].

To this end, several coupling schemes to implement two-qubit gates have

Figure 4.1: Three types of two-qubit coupling scheme. Fixed-frequency and tunable elements are represented by green and red blocks, respectively. **(a)** Tunable qubits coupled via fixed resonator coupler. **(b)** Fixed-frequency qubits with gate activated by microwave drives. **(c)** Fixed-frequency qubits coupled via tunable coupler.

been successfully demonstrated with similarly high fidelity on the level of 99 % or higher. These coupling schemes can generally be divided into three categories [156] as shown in Fig. 4.1. The first category (Fig. 4.1(a)) uses the tunable transmon qubits as mentioned previously with a fixed-frequency coupling element. The two-qubit gates are implemented by tuning respective energy levels into resonance [155, 157–160]. The fidelity of this type of CZ gate reached 99 % for the first time in 2014 [157, 161]. The second category (Fig. 4.1(b)) operates with fixed-frequency qubits using an all-microwave control scheme for implementing the two-qubit gate. With this layout, the gate is typically implemented by driving one qubit at the frequency of the other qubit, which is known as the cross-resonance gate [162–166]. Although fixed frequency qubits can provide longer coherence time, this gate typically requires a longer operation time in comparison to what have been demonstrated with the first category of coupling schemes. [156].

In this Chapter, the discussion is focused on the third category of two-qubit gates (Fig. 4.1(c)), which utilizes either parametric modulation or adiabatic tuning of the magnetic flux applied to the additional coupling element in order to induce a tunable coupling between the qubits. Several demonstrations of two-qubit gates based on this type of scheme have been presented with relatively high fidelity [167–171]. This tunable coupling architecture has been viewed as a promising alternative to implement high-fidelity two-qubit gates [172], achieving fidelity on the level of 99.9 % with recent developments [72, 173]. We will layout the theoretical background and experimental implementation of two-qubit parametric gates, introducing the calibration procedure and benchmarking experiments in the process.
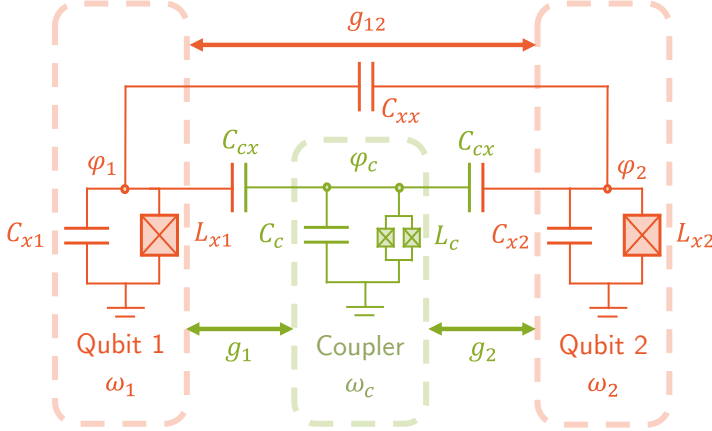
Figure 4.2: The circuit model representing the two-path tunable coupling scheme. The circuit elements that comprise the qubits and the coupler are marked in red and green respectively. There is a direct capacitive connection between each pair of the three elements, with g_1, g_2 and g_{12} indicating the corresponding coupling rates.

4.1 Two-qubit Tunable Coupling Scheme

In order to explore the options enabled by the addition of a tunable coupling element between the two fixed-frequency qubits, we utilize the circuit design outlined in Fig. 4.2, consisting of two computational qubits and a tunable coupling element. Without losing generality, the two qubits are allowed to interact directly with each other with the coupling strength g_{12} and each of them is also coupled to the central coupler with a rate of g_1 and g_2 respectively. In the circuit diagram, the three transmon elements are represented by two lumped elements in parallel: a non-linear inductor L_{xi}, and a capacitor C_{xi}. The direct coupling channel between the qubits is mediated by the capacitance C_{xx} while the one between each qubit to the coupler is mediated by C_{cx}. The theoretical features of this scheme and possible implementations of different types of two-qubit gates will be examined carefully in the following sections.

4.1.1 Circuit Quantization

To quantitatively determine the coupling rates and non-linear interaction strength in a system of capacitors and Josephson junctions, we can start with the Lagrangian of the circuit model assuming all three elements are tunable for the most general cases,

$$
\begin{aligned}
\mathcal{L} &= T - U \\
T &= \frac{1}{2} \vec{\dot{\phi}}^T \mathbf{C} \vec{\dot{\phi}} \\
U &= \sum_{i=1,2,c} E_{J,i}(\Phi_{\text{ext,i}}) \cos[\frac{\phi_i}{\Phi_0}],
\end{aligned}
\tag{4.1}
$$

where T and U are the kinetic and potential energy respectively. In the kinetic part of the Lagrangian, the node flux vector $\vec{\phi}$ and the capacitance matrix $\mathbf{C}$, obtained from Fig. 4.2, are

$$
\vec{\phi} = \begin{bmatrix} \phi_1 \\ \phi_2 \\ \phi_c \end{bmatrix}, \mathbf{C} = \begin{bmatrix} C_{x1} + C_{xx} + C_{cx} & -C_{xx} & -C_{cx} \\ -C_{xx} & C_{x2} + C_{xx} + C_{cx} & -C_{cx} \\ -C_{cx} & -C_{cx} & C_{xx} + 2C_{cx} \end{bmatrix}.
\tag{4.2}
$$

The node flux ϕ_i for the respective element is used as the generalized coordinate of the system and C_{xi} is the transmon capacitance as denoted in Fig. 4.2. For the potential energy, the tunable Josephson energy $E_{J,i}(\Phi_{\text{ext,i}})$, depending on the external flux $\Phi_{\text{ext,i}}$ threading through the respective SQUID loop, is

$$
E_{J,i}(\Phi_{ext,i}) = \frac{E_{J,i,L} + E_{J,i,R}}{1 + r} \sqrt{1 + r^2 + 2r \cos(2\frac{\Phi_{ext,i}}{\Phi_0})}.
\tag{4.3}
$$

The $E_{J,i,L}$ and $E_{J,i,R}$ are the Josephson energy of the left and right junction, and $r = \frac{E_{J,i,L}}{E_{J,i,R}}$ is the asymmetry between them. The canonical conjugates to the node flux ϕ_i are the node charges q_i that are treated as the generalized momentum,

$$
q_i = \frac{\partial \mathcal{L}}{\partial \dot{\phi}_i} = \mathbf{C}_{ii} \dot{\phi},
\tag{4.4}
$$

and $\overrightarrow{q} = \mathbf{C}\dot{\overrightarrow{\phi}}$. With the Legendre transformation, the Hamiltonian can be derived from the Lagrangian as

$$H = \sum_i q_i \dot{\phi}_i - \mathcal{L} = \frac{1}{2}\overrightarrow{q}^T \mathbf{C}^{-1} \overrightarrow{q} + U \tag{4.5}$$

where the inverse capacitance matrix $\mathbf{C}^{-1}$ is

$$\mathbf{C}^{-1} = \frac{1}{\|\mathbf{C}\|} \begin{bmatrix} n_{11} & n_{12} & n_{1c} \\ n_{21} & n_{22} & n_{2c} \\ n_{c1} & n_{c2} & n_{cc} \end{bmatrix}. \tag{4.6}$$

The $\|\mathbf{C}\|$ is the norm of the capacitance matrix $\mathbf{C}$ and n_{ij} is the inverse matrix element that contributes to the coefficient of the term $q_i q_j$ from capacitive coupling. We can quantize the generalized coordinates ϕ_i and momenta q_i with

$$\hat{\phi}_i = \sqrt{\frac{\hbar}{2\omega_i L_i}}(\hat{a}_i + \hat{a}_i^\dagger),$$
$$\hat{q}_i = -i\sqrt{\frac{\hbar\omega_i L_i}{2}}(\hat{a}_i - \hat{a}_i^\dagger), \tag{4.7}$$

where L_i is the inductance of the Josephson junction, $\hat{a}_i$ and $\hat{a}_i^\dagger$ are the annihilation and creation operator of the respective element. The Hamiltonian can be re-arranged into the form

$$H = \sum_{i=1,2,c} (\omega_i a_i^\dagger a_i - \frac{\eta_i}{2} a_i^\dagger a_i^\dagger a_i a_i) + \sum_{i,j=1,2,c} g_{ij}(a_i^\dagger a_j + a_i a_j^\dagger - a_i^\dagger a_j^\dagger - a_i a_j), \tag{4.8}$$

that includes frequency ω_i and anharmonicity η_i of the transmon element as well as the co-rotating terms, $a_i^\dagger a_j$ and $a_i a_j^\dagger$, and counter-rotating terms, $a_i^\dagger a_j^\dagger$ and $a_i a_j$, that describe the interaction between them. The qubit or coupler frequency ω_i as well as the anharmonicity η_i are proportional to the respective diagonal terms n_{ii}, whereas the coupling rate between the element g_{ij} is proportional to the sum of corresponding off-diagonal terms $n_{ij} + n_{ji}$.

From this Hamiltonian, we can calculate the desired coupling strength for a chosen set of device parameters in the experimental realization of the tunable

coupling scheme.

4.1.2 Circuit Hamiltonian

For a more intuitive understanding of the features of this system, we can simplify the Hamiltonian in Eq. (4.8) with several assumptions. Firstly, the higher energy levels of the elements do not contribute to the interactions within the first excitation manifold. Secondly, only the co-rotating terms are kept for the exchange interactions after the rotating wave approximation. The third assumption is that the coupler is in the ground state at all times. The resulting Hamiltonian, in the two-qubit subspace, can be written as

$$H = \sum_{i=1,2} \frac{1}{2}\omega_i\sigma_i^z + \frac{1}{2}\omega_c\sigma_{\rm c}^z + \sum_{i=1,2} g_i(\sigma_i^+\sigma_{\rm c}^- + \sigma_i^-\sigma_{\rm c}^+) + g_{12}(\sigma_1^+\sigma_2^- + \sigma_1^-\sigma_2^+), \quad (4.9)$$

in the Pauli basis representation, where σ_i^z, σ_i^+ and σ_i^- are Pauli-Z, rising and lowing operators for the respective elements. There are two channels of interaction between the qubits: the direct coupling g_{12} and an indirect path via the virtual exchange interaction mediated by the coupler, arising from the coupling from each qubit to the coupler, g_1 and g_2. Assuming the qubit frequency is lower than that of the coupler, $\Delta_i = \omega_i - \omega_{\rm c} < 0$ and $|\Delta_i| \gg g_i$, such that the coupling is dispersive, the effective coupling strength of the indirect channel could be calculated with the Schrieffer-Wolff transformation,

$$S = e^{\sum_{i1,} \frac{g_{i2}}{\Delta_i}(\sigma_i^+\sigma_{\rm c}^- + \sigma_i^-\sigma_{\rm c}^+)}, \quad (4.10)$$

which decouples the coupler from the system. The resulting expression of the two-qubit Hamiltonian including the fourth-order contributions is

$$\widetilde{H} = SHS^\dagger = \sum_{i=1,2} \frac{1}{2}\widetilde{\omega}_i\sigma_i^z + J_{\rm DC}(\sigma_1^+\sigma_2^- + \sigma_1^-\sigma_2^+), \quad (4.11)$$

with

$$\widetilde{\omega}_i = \omega_i + \frac{g_i^2}{\Delta_i}, \quad (4.12)$$

$$J_{\mathrm{DC}} = \frac{g_1 g_2}{2}\left(\frac{1}{\Delta_1} + \frac{1}{\Delta_2} - \frac{1}{\Sigma_1} - \frac{1}{\Sigma_2}\right) + g_{12}, \qquad (4.13)$$

and

$$\Delta_i = \omega_i - \omega_c, \Sigma_i = \omega_i + \omega_c. \qquad (4.14)$$

The $\widetilde{\omega}_i$ is the shifted qubit frequency due to the coupling to the coupler. The effective-qubit coupling J_{DC} has two contributions: g_{12} from the direct qubit-qubit coupling, which is always positive; the other term with the coefficient $\frac{g_1 g_2}{2}$ comes from the indirect coupling via the coupler. Since we choose to operate at $\Delta_i < 0$, the sign of the indirect coupling term is always negative. Therefore, there is a competition between the two coupling channels and the sign and magnitude of J_{DC} can be adjusted with the coupler frequency ω_{c} through Δ_i and Σ_i.

Theoretically, there always exists a specific coupler frequency ω_c^{off} such that the effective coupling $J_{\mathrm{DC}} = 0$ if $g_{12} > 0$, as shown in Fig. 4.3. The only physical limitation is that this frequency is still within the range of the flux tunability of the coupler. Although it is ideal to operate within the dispersive regime that satisfies $|\Delta_i| \gg g_i$ to prevent qubit population leaking into the coupler, it is still possible to have the switch-off point at ω_c^{off} in a system with significantly larger direct coupling strength g_{12} in the weakly dispersive regime where $|\Delta_i| > g_i$.

Additionally, the validity of the Schrieffer-Wolff transformation and thus the derivation of the effective coupling strength relies on the third assumption that the coupler remains in its ground state at all times. Therefore, the effect of coupler excitations such as thermal population need to be directly calculated from the full Hamiltonian of the entire system shown in Eq. (4.8).

4.2 Parameteric Gate Mechanisms

With the shown circuit, on top of the static effective J_{DC} coupling mentioned above, there are more possible coupling mechanisms enabled by the dynamic J_{AC} from parametric modulation of the coupler flux bias, which will be introduced in this section. From this coupling mechanism, at least three types of two-qubit gates can be constructed, which are parametric iSWAP [170], CPHASE [174] and SWAP [175]. In this section, the main mechanism for all
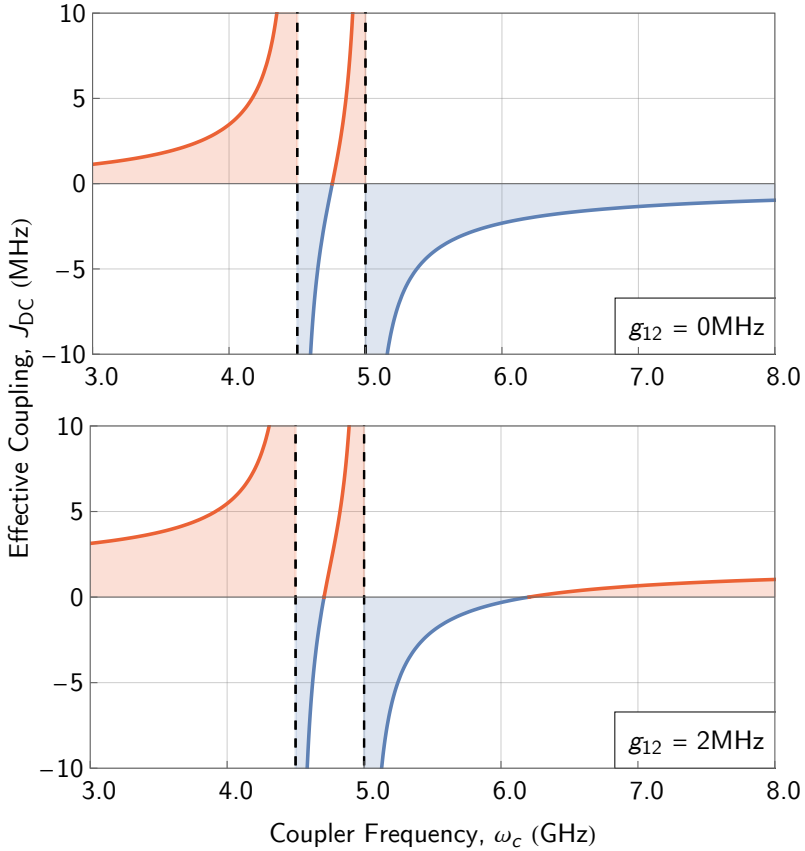
Figure 4.3: Effective qubit-to-qubit coupling strength J_{DC} as a function of coupler frequency. Depending on the strength of the direct coupling between the two qubits, g_{12}, there exist two regimes: 1) in the upper plot, $g_{12} = 0$, so there is no J_{DC} cancellation point for couplers being above the qubit frequencies; 2) in the lower plot, $g_{12} = 2$ MHz, J_{DC} cancellation point is at $\omega_{\mathrm{c,0ff}} = 6.2$ GHz. The part with negative(positive) J_{DC} is shown in blue(red).

three gates will be discussed as well as their specific features and advantages.

4.2.1 Parametric iSWAP

First, we will discuss the two parametric coupling gates. Since the coupler is flux-tunable, its frequency dependence is

$$\omega_c(\Phi) = \omega_c(0)\sqrt{|\cos(\frac{\pi\Phi}{\Phi_0})|}, \qquad (4.15)$$

where Φ_0 is the flux quantum. If a sinusoidal flux-bias modulation of amplitude A_0 and frequency ω_Φ is applied to the coupler, the total flux is then

$$\Phi(t) = \Theta + A_0\cos(\omega_\Phi t), \qquad (4.16)$$

where Θ is the constant DC flux applied to bias the coupler at a chosen frequency. Assuming that the modulation amplitude is much smaller than one flux quantum, $A_0 \ll \Phi_0$, the shifted qubit frequency derived in Eq. (4.12), $\widetilde{\omega}_i(\Phi(t))$, can be expanded to second order in $A_0\cos(\omega_\Phi t)$ as

$$\begin{aligned}
\widetilde{\omega}_i(\Phi(t)) &\approx \widetilde{\omega}_i(\Theta) + \frac{\partial\widetilde{\omega}_i}{\partial\Phi}\bigg|_{\Phi=\Theta} A_0\cos(\omega_\Phi t) + \frac{1}{2}\frac{\partial^2\widetilde{\omega}_i}{\partial\Phi^2}\bigg|_{\Phi=\Theta} (A_0\cos(\omega_\Phi t))^2 \\
&= \widetilde{\omega}_i(\Theta) - \frac{A_0^2}{4}\frac{\partial^2\widetilde{\omega}_i}{\partial\Phi^2}\bigg|_{\Phi=\Theta} + \frac{\partial\widetilde{\omega}_i}{\partial\Phi}\bigg|_{\Phi=\Theta} A_0\cos(\omega_\Phi t) + \frac{\partial^2\widetilde{\omega}_i}{\partial\Phi^2}\bigg|_{\Phi=\Theta}\frac{A_0^2}{4}\cos(2\omega_\Phi t).
\end{aligned}$$
$$(4.17)$$

The additional terms in the Eq. (4.17) comparing to the unmodulated qubit frequency are a second-order DC shift and two oscillating terms at ω_Φ and $2\omega_\Phi$ respectively. Since this representation is calculated from the definition of the Taylor expansion, the same results apply to $J(\Phi(t))$ as well:

$$\begin{aligned}
J(\Phi(t)) &\approx J(\Theta) + \frac{\partial J}{\partial\Phi}\bigg|_{\Phi=\Theta} A_0\cos(\omega_\Phi t) + \frac{1}{2}\frac{\partial^2 J}{\partial\Phi^2}\bigg|_{\Phi=\Theta} (A_0\cos(\omega_\Phi t))^2 \\
&= J(\Theta) - \frac{A_0^2}{4}\frac{\partial^2 J}{\partial\Phi^2}\bigg|_{\Phi=\Theta} + \frac{\partial J}{\partial\Phi}\bigg|_{\Phi=\Theta} A_0\cos(\omega_\Phi t) + \frac{\partial^2 J}{\partial\Phi^2}\bigg|_{\Phi=\Theta}\frac{A_0^2}{4}\cos(2\omega_\Phi t).
\end{aligned}$$
$$(4.18)$$

Inserting the expansion for $\widetilde{\omega}_i$ (Eq. (4.17)) and $J(\Phi)$ (Eq. (4.18)), the effective Hamiltonian derived in Eq. (4.11) becomes

65

$$\widetilde{H} = H_0 + H_1,$$

$$H_0 = \sum_{i=1,2} \frac{1}{2} \left[\widetilde{\omega}_i(\Theta) - \frac{A_0^2}{4} \frac{\partial^2 \widetilde{\omega}_i}{\partial \Phi^2} + \frac{\partial \widetilde{\omega}_i}{\partial \Phi} A_0 \cos(\omega_\Phi t) + \frac{\partial^2 \widetilde{\omega}_i}{\partial \Phi^2} \frac{A_0^2}{4} \cos(2\omega_\Phi t) \right] \sigma_i^z,$$

$$H_1 = \left[J(\Theta) - \frac{A_0^2}{4} \frac{\partial^2 J}{\partial \Phi^2} + \frac{\partial J}{\partial \Phi} A_0 \cos(\omega_\Phi t) + \frac{\partial^2 J}{\partial \Phi^2} \frac{A_0^2}{4} \cos(2\omega_\Phi t) \right] (\sigma_1^+ \sigma_2^- + \sigma_1^- \sigma_2^+),$$

$$(4.19)$$

with all derivatives with respect to Φ evaluated at $\Phi = \Theta$. Moving to the rotating frame of the respective qubit frequency, the oscillating parts in $\omega(\Phi(t))$ is averaged out to be zero. The effect of static term in $J(\Phi(t))$ is also suppressed if the qubits are not on resonance, $|\Delta_{|10\rangle - |01\rangle}| = |\omega_1 - \omega_2| \neq 0$ and the coupling is small comparing to the qubit detuning $|\Delta_{|10\rangle - |01\rangle}| \gg J(\Theta)$. In this case, the Hamiltonian can be simplified to

$$H_0 = \sum_{i=1,2} \frac{1}{2} \left[\widetilde{\omega}_i(\Theta) - \frac{A_0^2}{4} \frac{\partial^2 \widetilde{\omega}_i}{\partial \Phi^2} \right] \sigma_i^z,$$

$$H_1 = \left[\frac{\partial J}{\partial \Phi} A_0 \cos(\omega_\Phi t) + \frac{\partial^2 J}{\partial \Phi^2} \frac{A_0^2}{4} \cos(2\omega_\Phi t) \right] e^{i\widetilde{\Delta}_{|10\rangle - |01\rangle} t} (\sigma_1^+ \sigma_2^- + \sigma_1^- \sigma_2^+),$$

$$(4.20)$$

$$\widetilde{\Delta}_{|10\rangle - |01\rangle} = \left[\widetilde{\omega}_1(\Theta) - \widetilde{\omega}_2(\Theta) \right] - \frac{A_0^2}{4} \left[\frac{\partial^2 \widetilde{\omega}_1}{\partial \Phi^2} - \frac{\partial^2 \widetilde{\omega}_2}{\partial \Phi^2} \right], \qquad (4.21)$$

where $\widetilde{\Delta}_{|10\rangle - |01\rangle}$ is the qubit-qubit frequency detuning including the second-order terms from the effect of the coupler modulation drive found in Eq. (4.12). Therefore, when the modulation frequency ω_Φ is on resonance with the detuning $\widetilde{\Delta}_{|10\rangle - |01\rangle}$, the interaction part of Hamiltonian is

$$H_1 = J_{\text{AC}}(\sigma_1^+ \sigma_2^- + \sigma_1^- \sigma_2^+) = J_{\text{AC}}(|10\rangle \langle 01| + |01\rangle \langle 10|) = \frac{1}{2} J_{\text{AC}}(\sigma_1^X \sigma_2^X + \sigma_1^Y \sigma_2^Y).$$

$$(4.22)$$

with

$$J_{\text{AC}} = A_0 \frac{\partial J}{\partial \Phi}, \qquad (4.23)$$

Equation (4.22) describes an XX-YY exchange interaction between the
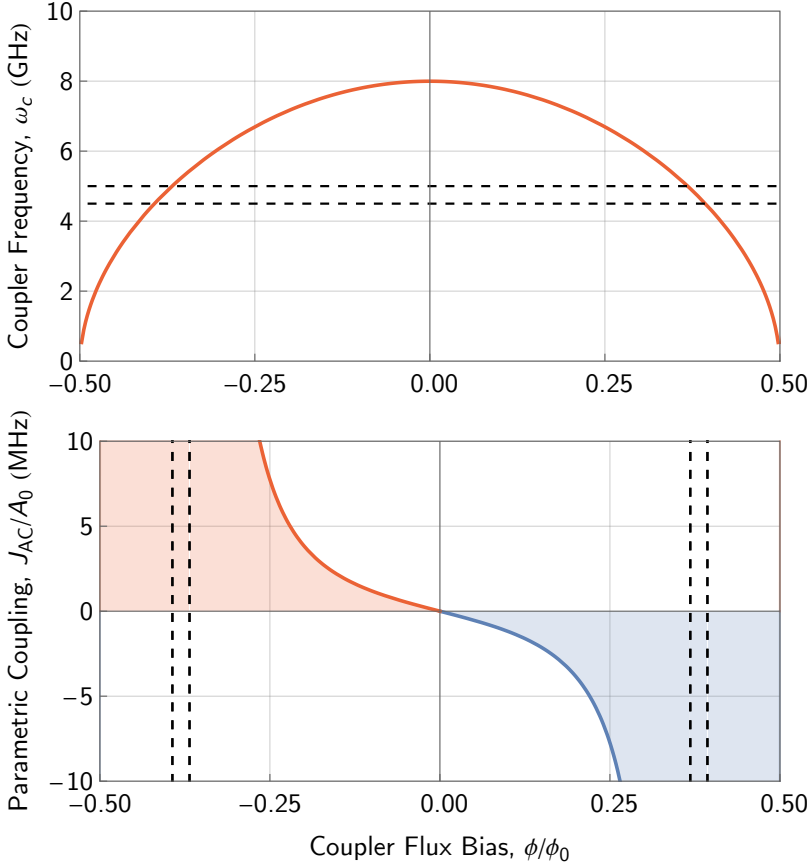
Figure 4.4: Coupler bias point and parametric coupling strength. The upper plot shows the coupler frequency ω_c as a function of coupler flux bias ϕ. The two Josephson junctions in the coupler SQUID loop are symmetric and the maximal coupler frequency is designed to be 8 GHz. The dashed lines represent the frequencies of the two coupled qubits. The lower plot shows the parametric coupling rate J_{AC}/A_0 as a function of coupler flux bias ϕ. Since J_{AC} is proportional to the first derivative of the coupler flux tunability curve, the coupling rate is antisymmetric and exactly zero at the sweet spot of the coupler. The dashed line represents where the coupler will be on resonant with the qubits in frequency.

qubits, with an effective coupling strength J_{AC} induced by the coupler flux-bias modulation that depends on the modulation strength in flux quanta A_0 and the first derivative of J with respect to Φ. There is also a resonant interaction if $2\omega_\Phi = \widetilde{\Delta}_{|10\rangle - |01\rangle}$ is fulfilled, but with a different coupling strength. The values for the parametric coupling rates J_{AC}/A_0 as a function of coupler flux bias Φ are shown in Fig. 4.4 for a coupler with 8 GHz maximum frequency coupled to two qubits with frequencies 5 GHz and 4.5 GHz and $g_{12} = 0$.

In the two-qubit basis where

$$|00\rangle = \begin{bmatrix} 1 \\ 0 \\ 0 \\ 0 \end{bmatrix}, |01\rangle = \begin{bmatrix} 0 \\ 1 \\ 0 \\ 0 \end{bmatrix}, |10\rangle = \begin{bmatrix} 0 \\ 0 \\ 1 \\ 0 \end{bmatrix}, |11\rangle = \begin{bmatrix} 0 \\ 0 \\ 0 \\ 1 \end{bmatrix}, \tag{4.24}$$

the matrix form of the Hamiltonian is simply

$$\widetilde{H} = \begin{bmatrix} 0 & 0 & 0 & 0 \\ 0 & 0 & J_{AC} & 0 \\ 0 & J_{AC} & 0 & 0 \\ 0 & 0 & 0 & 0 \end{bmatrix}, \tag{4.25}$$

which only couples $|10\rangle$ and $|01\rangle$ qubit states. The unitary propagator after interacting for a time τ is

$$\widehat{U}(\tau) = e^{\frac{iH\tau}{\hbar}} = \begin{bmatrix} 1 & 0 & 0 & 0 \\ 0 & \cos(J_{AC}\tau) & i\sin(J_{AC}\tau) & 0 \\ 0 & i\sin(J_{AC}\tau) & \cos(J_{AC}\tau) & 0 \\ 0 & 0 & 0 & 1 \end{bmatrix}. \tag{4.26}$$

Therefore, by fine tuning the amplitude of the modulation A_0 and gate time τ_0 such that $J_{AC} \cdot \tau_0 = \pi$, as illustrated in Fig. 4.5, we can perform an iSWAP gate on the two qubits given by the unitary propagator

$$\widehat{U}(\tau_0) = \begin{bmatrix} 1 & 0 & 0 & 0 \\ 0 & \cos(\pi) & i\sin(\pi) & 0 \\ 0 & i\sin(\pi) & \cos(\pi) & 0 \\ 0 & 0 & 0 & 1 \end{bmatrix} = \begin{bmatrix} 1 & 0 & 0 & 0 \\ 0 & 0 & i & 0 \\ 0 & i & 0 & 0 \\ 0 & 0 & 0 & 1 \end{bmatrix} = \widehat{U}_{iSWAP}. \tag{4.27}$$
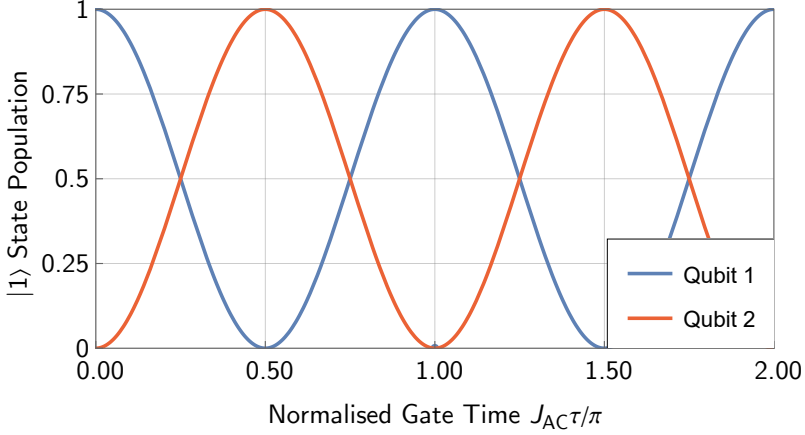
Figure 4.5: The evolution of the excited state population of each qubit as a function of the normalized interaction time $J_{\mathrm{AC}}\tau_0/\pi$. At first, the Qubit 1 population (blue) is in the excited state while that of the Qubit 2 (red) is in the ground state. The plot indicates that after $J_{\mathrm{AC}}\tau_0/\pi = 1$ of interaction, the $|1\rangle$-level population of the qubits are completely swapped.

4.2.2 Parametric CPHASE (CZ)

This method can be used to find similar exchange interactions between any states in the same excitation manifold. Therefore, in the second excitation manifold of the two-qutrit system consisting of the $|11\rangle$, $|20\rangle$ and $|02\rangle$ states, the Hamiltonian in Eq. (4.20) becomes

$$
\widetilde{H} = \left[\frac{\partial \widetilde{J}}{\partial \Phi} A_0 \cos(\omega_\Phi t) + \frac{\partial^2 \widetilde{J}}{\partial \Phi^2} \frac{A_0^2}{4} \cos(2\omega_\Phi t) \right] \cdot \left[e^{i\widetilde{\Delta}_{|11\rangle - |02\rangle} t} (|20\rangle\langle 11| + |11\rangle\langle 20|) \right],
\tag{4.28}
$$

with

$$
\widetilde{\Delta}_{|11\rangle - |02\rangle} = \left[\widetilde{\omega}_1(\Theta) - \eta_1 - \widetilde{\omega}_2(\Theta) \right] - \frac{A_0^2}{4} \left[\frac{\partial^2 \widetilde{\omega}_1}{\partial \Phi^2} - \frac{\partial^2 \widetilde{\omega}_2}{\partial \Phi^2} \right] = \widetilde{\Delta}_{|10\rangle - |01\rangle} - \eta_1,
\tag{4.29}
$$

where $\eta_i = \omega_{eg,i} - \omega_{ef,i}$ is the anharmonicity of the qubit, and $\widetilde{J}$ is the effective static coupling strength between $|11\rangle$ and $|20\rangle$ level mediated by the

coupler. The Hamiltonian for the interaction between $|11\rangle$ and $|02\rangle$ has the same form of Eq. (4.20) with a different $\widetilde{J}$ and $\widetilde{\Delta}_{|11\rangle-|02\rangle} = \widetilde{\Delta}_{|10\rangle-|01\rangle} + \eta_2$. For each case, the coupling strength $\widetilde{J}$ needs to be calculated from the generalized Tavis-Cummings methods for multi-level qubits for the levels involved in the interaction [155]. Therefore, when ω_Φ is on resonance with either $\widetilde{\Delta}_{|11\rangle-|02\rangle}$ or $\widetilde{\Delta}_{|11\rangle-|02\rangle}$, the Hamiltonian can be simplified to

$$\widetilde{H} = \widetilde{J}_{\mathrm{AC}}(|20\rangle\langle 11| + |11\rangle\langle 20|), \tag{4.30}$$

with

$$\widetilde{J}_{\mathrm{AC}} = A_0 \frac{\partial \widetilde{J}}{\partial \Phi}. \tag{4.31}$$

The $\widetilde{H}$ is a 9×9 matrix, including the interaction between all states from the two qutrits. Truncating the Hamiltonian $\widetilde{H}$ down to two qubit states yields

$$\widehat{U}(\tau) = \begin{bmatrix} 1 & 0 & 0 & 0 \\ 0 & 1 & 0 & 0 \\ 0 & 0 & 1 & 0 \\ 0 & 0 & 0 & \cos(\widetilde{J}_{\mathrm{AC}}\tau) \end{bmatrix}. \tag{4.32}$$

Similar to the construction of the iSWAP gate, the amplitude A_0 and interaction time τ can be tuned to realize a 2π rotation between $|11\rangle$ and $|20\rangle$ or $|02\rangle$ level such that all population is returned to $|11\rangle$ level, which means $\cos^2(\widetilde{J}_{\mathrm{AC}}\tau_0) = 1$ and consequently $\widetilde{J}_{\mathrm{AC}}\tau_0 = \pi$. Therefore, the unitary will introduce a π phase shift to the $|11\rangle$ state while leaving the other computational states unchanged, implementing a CZ gate on the two qubits. The CZ unitary can be written as:

$$\widehat{U}(\tau_0) = \begin{bmatrix} 1 & 0 & 0 & 0 \\ 0 & 1 & 0 & 0 \\ 0 & 0 & 1 & 0 \\ 0 & 0 & 0 & \cos(\widetilde{J}_{\mathrm{AC}}\tau_0) \end{bmatrix} = \begin{bmatrix} 1 & 0 & 0 & 0 \\ 0 & 1 & 0 & 0 \\ 0 & 0 & 1 & 0 \\ 0 & 0 & 0 & -1 \end{bmatrix} = \widehat{U}_{\mathrm{CZ}} \tag{4.33}$$

In summary, as illustrated in Fig. 4.6, by choosing the coupler modulation frequency ω_Φ to be resonant with either $\widetilde{\Delta}_{|10\rangle-|01\rangle}$ or $\widetilde{\Delta}_{11-02(20)}$, we can im-
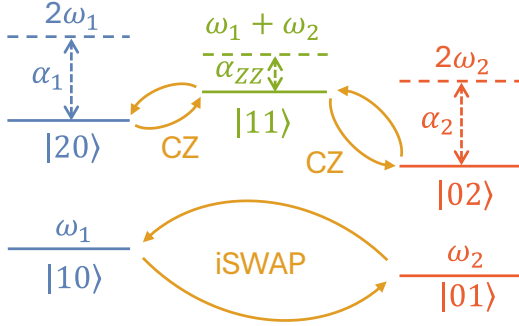
Figure 4.6: The level diagram of the system. The energy levels of Qubit 1 and Qubit 2 are shown in blue and red respectively. Additionally, the relevant level detunings for the implementation of the parametric iSWAP and the CZ gates are indicated as well.

plement two different types of two-qubit gate: iSWAP and CPHASE. In order to have a fast gate with a gate time τ of around 100 ns, the effective coupling strength due to parametric modulation $J_{\text{AC}} \propto \frac{\partial J_{\text{DC}}}{\partial \Phi} \backsim \frac{g_1 g_2}{\Delta^2}$ needs to be on the order of a few MHz. Ideally, the gate should operate within the regime where J_{DC} is predominately linear with respect to Φ to avoid any higher order effect from the modulation. For implementations with small qubit-qubit detuning, it will be necessary to achieve cancellation of the static J_{DC} to a negligible level during the idling time to prevent any undesired residual exchange interaction that could contribute to the gate error.

4.2.3 Parametric SWAP

One important gate that is not native to most [176, 177] quantum processors is the SWAP gate. This gate is useful in systems without long-range or all-to-all couplings between qubits, which is typical for superconducting quantum processor architectures. The SWAP gate allows a two-qubit operation between two distant qubits to be performed by repeatedly swapping the states [178, 179] within a chain of qubits, until the desired qubit states come adjacent to one another [179]. Moreover, the SWAP-like family of gates is the only two-qubit gate type that is guaranteed to avoid creating entanglement for any separable input state [180].
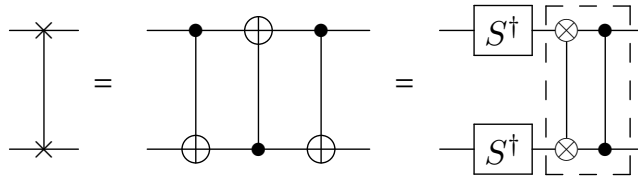
Figure 4.7: SWAP gate decomposition. A SWAP gate can be decomposed either into three consecutive CNOT gates or in a combination of iSWAP and CZ gates with additional single qubit gates. The iSWAP and CZ gate can be applied either consecutively or simultaneously.

With both iSWAP and CZ gates implemented, there is an extra advantage in the compilation of quantum circuits that contain SWAP gates. A SWAP gate can be decomposed into three CZ gates that can be implemented natively on most state-of-the-art quantum processors. Now, a more efficient decomposition is possible with a combination of an iSWAP and a CZ gate as shown in Fig. 4.7. Furthermore, the CZ gate commutes with the iSWAP gate, thus they can be applied in any order, or even simultaneously since the parametric flux pulses that drive the CZ and iSWAP gates each targets different frequencies. Detailed demonstration of this decomposition can be found in **Paper E**. Such enhancements are particularly crucial considering NISQ-era gate-error constraints given the high number of consecutive gates that must be implemented during the course of an algorithm [2, 176, 178, 179]. Besides NISQ, an augmented gate set may become useful in quantum error correction, where encoding and decoding segments can benefit from circuits designed to minimize the impact of SWAP gates [181].

To understand the compilation process, we can consider the unitary $U_{\mathrm{iSWAP-CZ}} = \mathrm{CZ} \cdot \mathrm{iSWAP}$,

$$U_{\mathrm{iSWAP-CZ}} = \begin{pmatrix} 1 & 0 & 0 & 0 \\ 0 & 0 & i & 0 \\ 0 & i & 0 & 0 \\ 0 & 0 & 0 & -1 \end{pmatrix} \begin{pmatrix} 1 & 0 & 0 & 0 \\ 0 & 0 & i & 0 \\ 0 & i & 0 & 0 \\ 0 & 0 & 0 & -1 \end{pmatrix} = \begin{pmatrix} 1 & 0 & 0 & 0 \\ 0 & 0 & i & 0 \\ 0 & i & 0 & 0 \\ 0 & 0 & 0 & -1 \end{pmatrix}.$$

(4.34)

If we use the conjugate transpose gates $S^\dagger$ on both qubits to convert the

off-diagonal i elements into 1 while also removing the negation on $|11\rangle$, where

$$(S^\dagger)^{\otimes 2} = \begin{pmatrix} 1 & 0 \\ 0 & -i \end{pmatrix}^{\otimes 2} = \begin{pmatrix} 1 & 0 & 0 & 0 \\ 0 & -i & 0 & 0 \\ 0 & 0 & -i & 0 \\ 0 & 0 & 0 & -1 \end{pmatrix}, \qquad (4.35)$$

we get that

$$(S^\dagger)^{\otimes 2} U_{\mathrm{iSWAP-CZ}} = \begin{pmatrix} 1 & 0 & 0 & 0 \\ 0 & -i & 0 & 0 \\ 0 & 0 & -i & 0 \\ 0 & 0 & 0 & -1 \end{pmatrix} \begin{pmatrix} 1 & 0 & 0 & 0 \\ 0 & 0 & i & 0 \\ 0 & i & 0 & 0 \\ 0 & 0 & 0 & -1 \end{pmatrix} = \begin{pmatrix} 1 & 0 & 0 & 0 \\ 0 & 0 & 1 & 0 \\ 0 & 1 & 0 & 0 \\ 0 & 0 & 0 & 1 \end{pmatrix}.$$

$$(4.36)$$

Equation 4.36 is identical to the SWAP unitary matrix. Since the $S^\dagger$ gates are implemented as 0 ns virtual-Z gates, such a SWAP sequence may be as short as the duration of either one iSWAP or one CZ gate. In **Paper E**, we present the implementation of this particular parametric SWAP gate in detail.

4.3 Parametric Gate Implementation

Equipped with the tools and understanding developed in the previous section, we can implement the tunable coupling scheme illustrated in Fig. 4.2. All three types of two-qubit gates that have been discussed can in principle be implemented with the same pair of fixed-frequency qubits. In particular, the capacitance C_i, Josephson energy E_j of each qubit are chosen such that the qubit's transition frequency is within the range of 4 to 5 GHz, compatible with current state-of-the-art designs. The coupler is designed to be tuned over a large range, starting from 7.5 GHz. The readout resonators are designed to be between 6 to 7 GHz for the qubits. The initial target for the qubit-coupler coupling rates, g_1 and g_2, are on the order of tens of MHz. The measured parameters of the chosen sample used for the gate characterization in the later sections are listed in Table 4.1.

The fabricated sample with the listed parameters is illustrated in Fig. 4.8. There are three elements on the sample: two transmons operating as computational qubits, and another transmon between them serving as the coupler.

	E_j/h (GHz)	E_c/h (GHz)	C_{cx} (fF)	$g_i/2\pi$ (MHz)
Qubit 1	15.3	232.5	2.4	47
Qubit 2	18.1	143.4	4.4	64

Table 4.1: Designed Josephson junction energy E_j/h, charging energy E_c, the qubit and the coupler capacitance C_{cx} and calculated qubit-coupler interaction strength g_i for the two qubits.
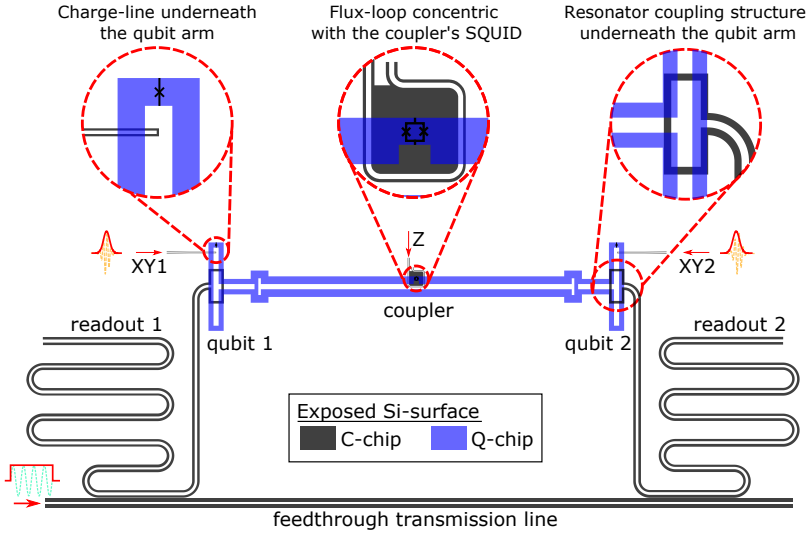
Figure 4.8: Two-qubit flip-chip device. Illustration of two fixed-frequency transmon qubits and one frequency-tunable coupler, located on the Q-chip, and control lines (charge- or XY-line, flux- or Z-line), $\lambda/4$ readout resonators, and a feedthrough transmission line, located on the C-chip. The shaded area corresponds to the exposed silicon surface on each chip. The left inset shows the charge-lines (C-chip), opposite the qubit arm (Q-chip). The middle inset shows the flux-loop (C-chip), concentric with the SQUID loop of the coupler (Q-chip). The right inset shows the open-ended part of the readout resonator (C-chip), opposite the qubit (Q-chip). More details on this device are presented in **Paper C**.

As designed, the qubits are single-junction fixed-frequency transmons and the coupler is tunable in frequency via the flux threaded through its SQUID loop. The qubit excitation is driven via their respective charge line that is capac-
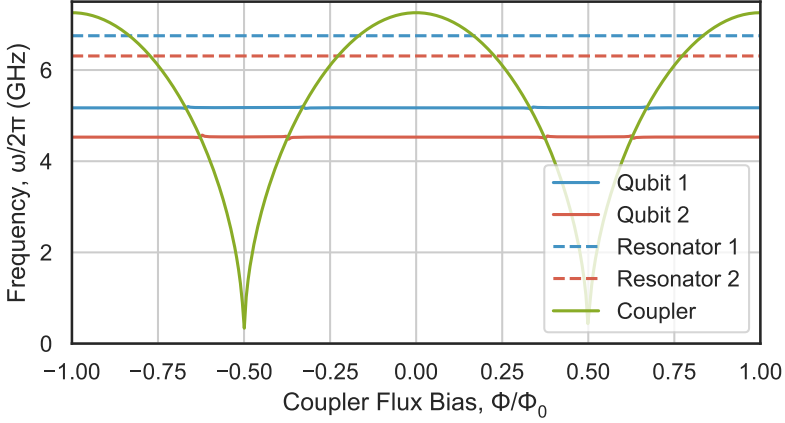
Figure 4.9: The flux dependence of the frequency of Qubit 1 (blue), Qubit 2 (red) and the coupler (green) fitted from flux sweep measurement. The chosen parking position of each element as listed in Table 4.2 is marked by the corresponding dashed line. Additionally, the frequency of the readout resonators for Qubit 1 and Qubit 2 are indicated as the dashed blue and red lines respectively.

	$\omega_{\mathrm{q}}/2\pi$ (GHz)	$\eta/2\pi$ (MHz)	T_1 (μs)	T_2^* (μs)
Qubit 1	5.176	-256	30.6	60.3
Qubit 2	4.534	-158	83.8	90.8

Table 4.2: Extracted frequencies and coherence times for the qubits. Qubit-qubit detuning $\Delta_{|10\rangle-|01\rangle}$ is 642 MHz.

	$\omega_{\mathrm{r}}/2\pi$ (GHz)	$\kappa/2\pi$ (MHz)	$\chi/2\pi$ (MHz)	$n_{\mathrm{th.},|e\rangle}$ (%)	$n_{\mathrm{th.},|f\rangle}$ (%)
Qubit 1	6.752	0.427	0.132	2.1	0.4
Qubit 2	6.308	0.294	0.088	2.3	0.3

Table 4.3: Readout properties of the qubits. The measured thermal populations are determined by direct single-shot readout.

itively coupled to the qubit. By design, the qubits have a direct capacitive coupling channel to the coupler but not to each other. They are also coupled to their respective readout resonator via a capacitor.

The frequency dependence for the applied flux-bias is measured for the cou-

pler, using qubit and resonator spectroscopy measurements. Fig. 4.9 shows the results fitted with Eq. (4.3) to determine the values for the maximal Josephson energies $E_{\text{j,max}}/h$, which are listed in Table 4.2. Additionally, the readout resonators for Qubit 1 and Qubit 2 are approximately located at 6.7 GHz and 6.3 GHz, shown as blue and red dashed lines in Fig. 4.9 respectively. The measured qubit coherence and readout properties are shown in Table 4.2 and Table 4.3. The coupler parking position is chosen such that the coupler frequency ω_c satisfies the condition

$$\omega_c = \omega_q + a \cdot \omega_{CZ}, \tag{4.37}$$

where ω_{CZ} is the CZ drive frequency, which can be either Δ_{20-11} or Δ_{02-11} [182]. We perform all gate characterization experiments at this parking position.

After the completion of single-qubit gate calibration, the following procedure is utilized to optimize the performance of two-qubit gates. For this implementation, all the parametric gates use similar interaction mechanisms and the types of flux pulse only differ in the frequency of the parametric flux drive. In the following sections, the parametric CPHASE gates will be the focus of our discussion, including the experimental results for the Chevron pattern, conditional phase and dynamic phase measurement, CMA-ES optimization, and randomized benchmarking.

4.3.1 Chevron Pattern Measurement

As a starting point for further optimization, the preliminary pulse parameters for the parametric CPHASE gate can be obtained by measuring the population exchange between the $|11\rangle$ and $|20\rangle$ ($|02\rangle$) level, following the application of the parametric flux pulse. The flux pulse has three main adjustable parameters: its length τ, modulation frequency ω_Φ and amplitude A_0. As shown in Fig. 4.10, both qubits are prepared in the ground state at the start of the experiment and then pulsed to the excited state. The flux pulse length τ and modulation frequency ω_Φ are swept between a chosen range while the amplitude A_0 of the pulse is fixed. The population of the qubit excited state is measured at the end of the sequence and plotted against the pulse length τ and modulation frequency ω_Φ in a 2D density plot as illustrated in Fig. 4.11.

Two horizontal line cuts of the Chevron pattern shown in Fig. 4.11 along
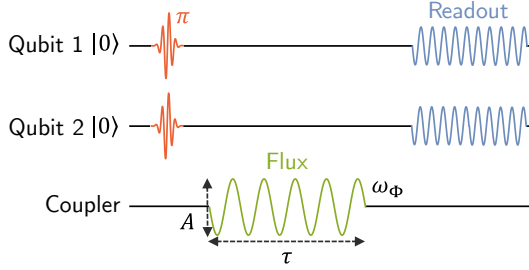
Figure 4.10: The pulse sequence for the Chevron pattern measurement with the parametric two-qubit gate. Either two parameters between the amplitude A_0, frequency ω_Φ and length τ of the flux pulse can be swept, while the remaining one is fixed. There are two short buffer periods before and after the flux pulse. The population of the qubits is measured at the end.
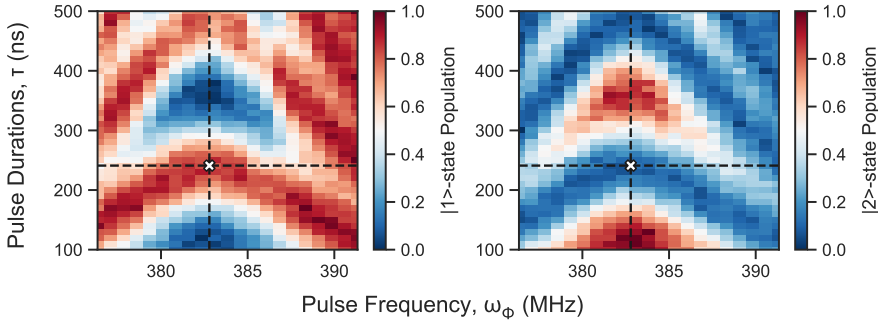
Figure 4.11: Chevron pattern with pulse frequency and duration sweeped. The measured $|1\rangle$ and $|2\rangle$- state population of Qubit 1 with the pulse scheme shown in Fig. 4.10 for a parametric CPHASE gate. The white cross indicates the required length and frequency to achieve full population exchange between the $|11\rangle$ and $|20\rangle$ states.

with the fitted model is illustrated in Fig. 4.12, with the results at $\omega_\Phi/2\pi = 378.6$ MHz and $\omega_\Phi/2\pi = 383.1$ MHz shown in red and blue respectively. As discussed in Section 4.2.2, for the CPHASE gate operation, ideally the population in the $|11\rangle$ level is completely swapped to the $|20\rangle$ level and fully recovered to $|11\rangle$ after an oscillation period of 2π. Therefore, we can extract the desired
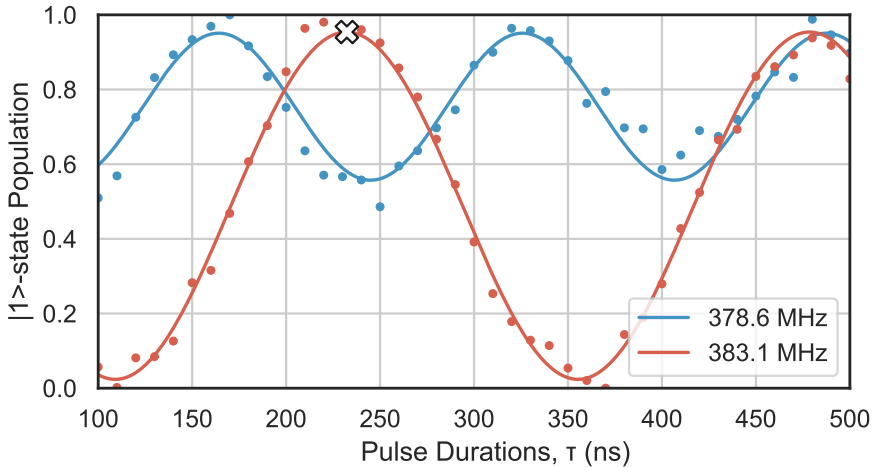
Figure 4.12: Off and on-resonant parametric drive response. The horizontal line cuts of the Chevron pattern in Fig. 4.11 at off-resonant ($\omega_\Phi/2\pi = 378.6$ MHz) and on-resonant ($\omega_\Phi/2\pi = 383.1$ MHz), which is shown in red and blue respectively. The white cross in the on-resonant curve (red) marks the same point as in Fig. 4.11, where the $|1\rangle$-level population is fully swapped to the $|2\rangle$-level and returned to the original state with an additional π phase shift.

pulse parameter with a closer examination of the population exchange as a function of pulse length at $\omega_\Phi/2\pi = 383.1$ MHz, where the condition on population exchange is fulfilled. As an example, for this dataset, the optimal pulse length is 241.0 ns with a fixed modulation amplitude of $A_0 = 0.05\Phi_0$.

Alternatively, having two-qubit gates of equal length across the chip is preferable to benefit the compilation of larger quantum circuits. Therefore, it is possible to fix the duration first to a reasonable value and sweep pulse amplitude and frequency instead. The resulting parameters space is shown in Fig. 4.13. In this case, to achieve a 256 ns gate, the pulse length in this measurement is first fixed to half of the target length, i.e. 128 ns. The parameters for maximal population swapping are easily identifiable as marked in the plot. Then, the pulse with the same frequency ω_Φ and amplitude A with double the starting length will induce a complete population swap between $|20\rangle$ and $|11\rangle$-state and back. These values will serve as the starting point for further gate calibration.

Figure 4.13: Chevron pattern with pulse frequency and amplitude sweeped. The measured $|1\rangle$ and $|2\rangle$- state population of Qubit 1 with the pulse scheme shown in Fig. 4.10 for a parametric CPHASE gate. The white cross indicates the required length and frequency to achieve full population exchange between the $|11\rangle$ and $|20\rangle$ state.
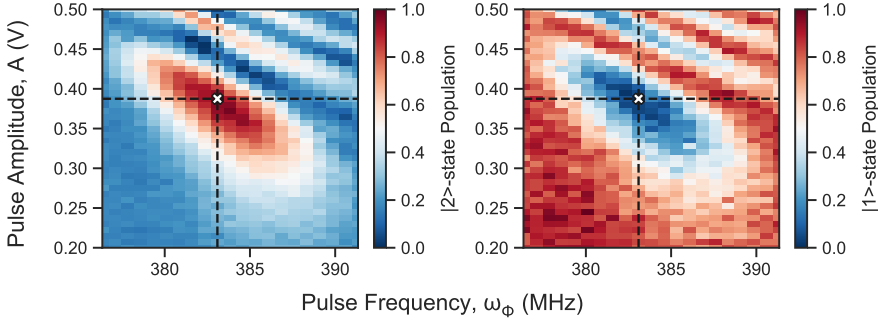
4.3.2 Conditional Phase Measurement

With the pulse parameters properly calibrated, we can continue to measure the conditional phase induced by the gate. The experimental scheme is illustrated in Fig. 4.14. In the plot, Qubit 1 is treated as the control qubit, and Qubit 2 as the target qubit, and the sequence can be repeated again with control and target qubit swapped to calibrate both instances the gate can be applied. Both qubits are prepared in the ground state at the start of the experiment. The gate flux pulse is applied to the coupler and a Ramsey-type experiment with a set of $\pi/2$-pulses is performed on the target qubit with the control qubit either in $|0\rangle$ or $|1\rangle$. The sweeping parameter of the Ramsey experiment is the phase of the second $\pi/2$-pulse, whereas the waiting time between the two pulses is fixed. The populations of both qubits are measured at the end of the experiment and plotted against the corresponding phase of the second Ramsey $\pi/2$-pulse.

The results are measured with three level single-shot readout with preselection. The measured excited state population of the target qubit that undergoes the Ramsey experiment is shown in Fig. 4.15 as an example. The conditional phase is acquired from the phase shift of the Ramsey signal when the gate is turned on or off depending on the state of excitation of the control qubit, which are shown in blue and red respectively. Ideally, the conditional
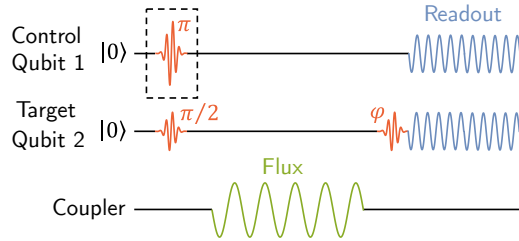
Figure 4.14: The pulse sequence of the conditional phase calibration.
First, the two qubits are prepared in the ground state. The π pulse on the control qubit switches the gate on or off and a Ramsey experiment is performed on the target qubit. The flux pulse on the coupler is a sinusoidal modulation with no DC component.
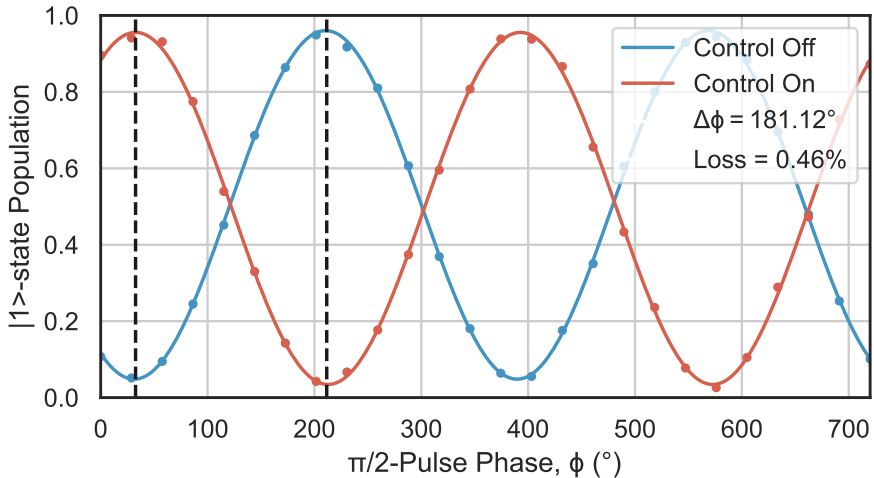
Figure 4.15: Conditional phase measurement. The measured $|1\rangle$-level population of Qubit 2 when the π-pulse on the control qubit is on (red) or off (blue) plotted against the phase of the second $\pi/2$-pulse. The results are fitted with a sinusoidal function and the relative phase difference and the change in maximal amplitude are extracted between the Ramsey signals, which are the conditional phase and population loss respectively.
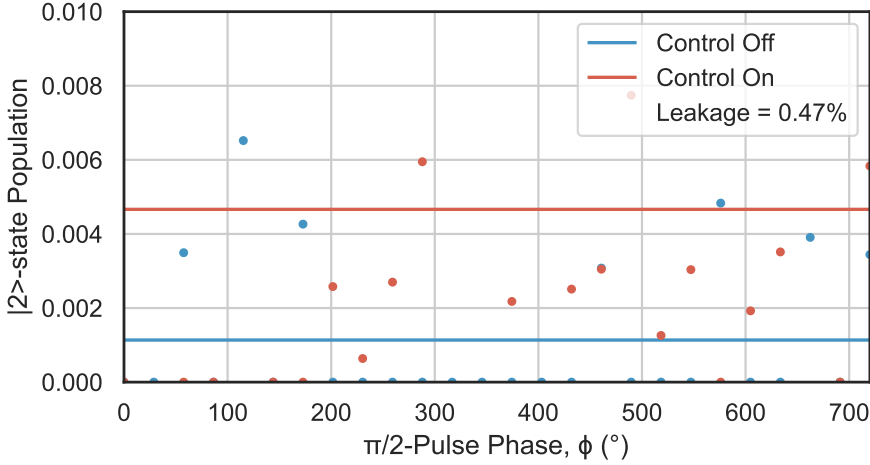
Figure 4.16: Leakage during conditional phase measurement. The measured |2⟩-level population of Qubit 1 when the gate is on (red) or off (blue) is plotted against the phase of the second $\pi/2$-pulse. The horizontal line indicates the mean value for each set of measurements. The leakage extracted is from the difference in the average |2⟩-level population between the two sets, shown as a solid line of the respective color.

phase is calibrated to be 180° by tuning and optimizing all three pulse parameters.

The population loss of the |11⟩ state after the gate operation can be obtained by comparing the maximal amplitude of the Ramsey signal of the target qubit when the gate is on or off. However, there are a multitude of error mechanisms that contribute to the measured population loss, such as decoherence of the qubits during the gate and unwanted coherent processes that involve population exchange between the |1⟩-state and other energy levels. Although the population loss only provides limited information regarding the source of errors, it can still serve as a general measure for the performance of the gate.

The leakage population outside of the computational subspace can be estimated from the measured |2⟩-state population of the control qubit after the conditional phase measurement sequence. An example of the measured result is shown in Fig. 4.16. By comparing the average level of the |2⟩-state population with the gate on (red) and off (blue), the leakage rate per gate can
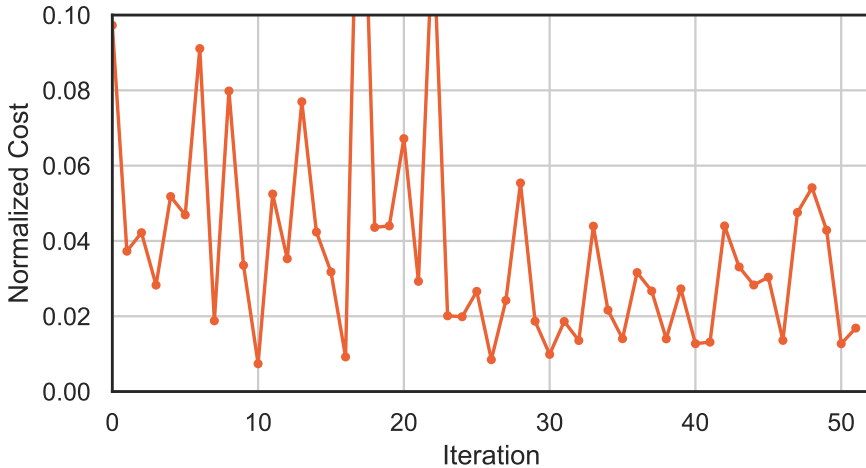
Figure 4.17: The evolution of gate performance during 50 iterations of CMA-ES optimization. The normalized cost function is calculated from $\sqrt{((\text{conditional phase} - 180°)/180°)^2 + (\text{leakage})^2 + (\text{population loss})^2}$.

be obtained, providing a direct measure of the potential error contribution to gate performance.

4.3.3 CMA-ES Flux Pulse Optimization

We tune-up the parametric CPHASE gate with the transition between $|11\rangle$ and $|20\rangle$. For the chosen frequency configuration, listed in Table 4.2, the required modulation frequency is around 381.1 MHz, which is verified with the Chevron pattern illustrated in Fig. 4.11. Manual calibration of the pulse parameters, including the modulation amplitude A_0 and frequency Φ_0, is done with the conditional phase sweep using the appropriate scheme for the parametric CPHASE gate as shown in Fig. 4.14. The target is to achieve a 180° conditional phase shift with minimal population loss and leakage during the gate. These settings are used as the starting position for the CMA-ES algorithm.

Using the conditional phase measurement once more, we can employ a classical *Covariance Matrix Adaptation Evolution Strategy* (CMA-ES) algorithm to numerically optimize the CPHASE gate with a stochastic process [183]. The

cost function used by the CMA-ES includes the deviation of conditional phase from 180°, population loss in the target qubit and leakage measured in the control qubit. The starting pulse parameters are tuned manually with the pulse length sweep of the conditional phase mentioned earlier. Generally, all pulse parameters specific to the type of CPHASE gate are tuned by several iterations of the CMA-ES process to minimize the cost function and output an optimal set of parameters. As an example, Fig. 4.17 shows the resulting conditional phase, leakage and population loss for 20 iterations of CMA-ES optimization. The values of the cost function can be represented by the norm, which is calculated as $\sqrt{((\text{conditional phase} - 180°)/180°)^2 + (\text{leakage})^2 + (\text{population loss})^2}$. For each factor, the mean of each iteration is indicated in purple dots and gradually converges towards the minimal value. Further details regarding the CMA-ES algorithm are described in the work of Hansen et. al.[184].

4.3.4 Dynamic Phase Measurement

On the other hand, the coupler pulse is also likely to affect the qubit frequencies and induce an extra phase shift to the individual qubit independent of the conditional phase. To measure the single qubit dynamic phase, each qubit is prepared in the ground state and then a Ramsey-type experiment is performed while the gate pulse is switched on or off, as illustrated in Fig. 4.18.

The measured results are shown in Fig. 4.19 and the dynamic phase for the respective qubit is directly obtained by finding the phase difference of the two Ramsey signals. Afterwards, the dynamic phase is corrected by applying a virtual-Z gate on the respective qubit after the gate when the tuned-up CPHASE gate is used as a component in another sequence.

After the dynamic phase calibration has been performed, the gate is ideally fully optimized and ready to be examined in order to characterize the gate performance.

4.3.5 Standard and Interleaved Randomized Benchmarking

In order to have a direct measure of the gate error, we perform the standard and interleaved randomized benchmarking (RB) with the two-qubit CPHASE gate [88]. The procedure is similar to the single-qubit randomized benchmarking described in Section 2.3.2. In this case, the difference is that the Clifford group used to generate the sequence contains both single-qubit gates
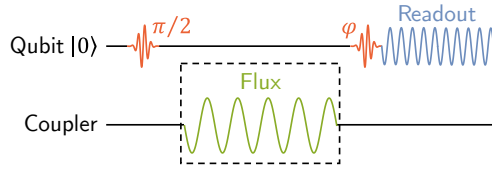
Figure 4.18: Dynamic phase measurement scheme. The pulse sequence of the dynamic phase measurement. The qubit is prepared in the ground state and a Ramsey experiment is performed while the flux pulse to the coupler is either on or off. The experiment is repeated on both qubits involved in the gate.
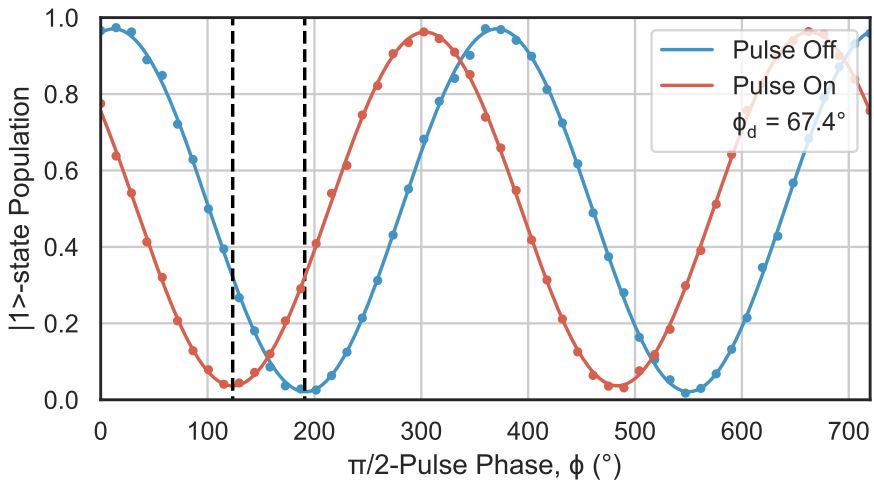
Figure 4.19: Dynamic phase measurement result. The measured Ramsey signal when the pulse is on or off is plotted against the phase of the second $\pi/2$-pulse. From the fitted sinusoidal function the relative phase difference can be extracted, which is the dynamic phase from the effect of the gate flux pulse.

and two-qubit gates such as C-NOT, iSWAP and SWAP like gates [157]. All of these three types can be decomposed into the target CPHASE gate and single qubit gates as indicated in Fig. 4.20. In total, for a two-qubit system, there are $24^2 = 576$ possible combinations for single qubit gates, $24^2 \times 3^2 = 5184$ gates in C-NOT and iSWAP like classes and $24^2 = 576$ gates in SWAP-like class [185]. Therefore, the total number of possible gates in the two-qubit Clifford
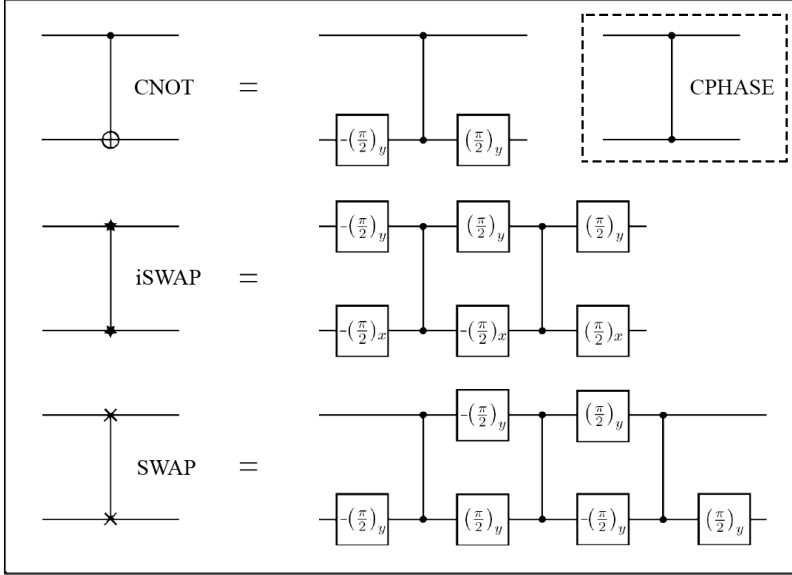
Figure 4.20: Scheme of the CNOT, iSWAP **and** SWAP **like class in the two-qubit Clifford group.** Every type of two-qubit gate can be decomposed into the +target CPHASE gate and single-qubit rotations.

group is 11520 and there are 1.5 CPHASE gates per Clifford on average.

The sequences for two-qubit gate RB are constructed as illustrated in Fig. 4.21, similar to the method described in Section 2.3.2. In the interleaved RB, an extra CPHASE gate is inserted between two Clifford gates [186]. The measured results are averaged over $k = 100$ randomly generated variations for each m Clifford sequence.

The measured expectation values of the two-qubit correlation $\langle \sigma_Z^{\otimes 2} \rangle$, from both standard and interleaved RB are plotted with the corresponding number of Cliffords m, in Fig. 4.22. The results are fitted with

$$\langle \sigma_Z^{\otimes 2}(m) \rangle = Ap^m + B, \tag{4.38}$$

and the extracted depolarizing rate $1 - p$, and the parameters A and B are listed in Table 4.4.
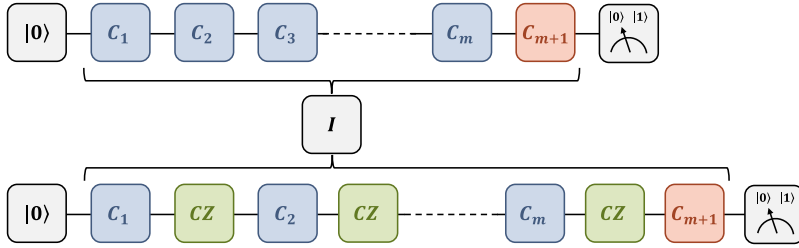
Figure 4.21: Two-qubit gate randomized benchmarking scheme. The standard (top) and interleaved (bottom) sequences are both listed. The standard sequence is constructed from randomly chosen gates in the two-qubit Clifford group. In the interleaved sequence, an additional CPHASE gate is inserted between each Clifford.
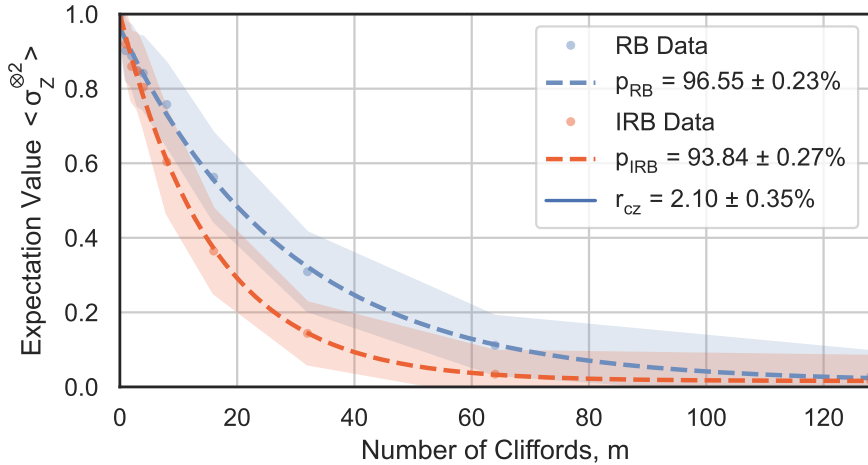
Figure 4.22: Two-qubit randomized benchmarking results. The measured two-qubit correlation $\langle\sigma_Z^{\otimes 2}\rangle$ as a function of the number of Cliffords in the RB (blue) and IRB (red) sequence m. The final two-qubit state is ideally returned to $|00\rangle$ state where $\langle\sigma_Z^{\otimes 2}\rangle = 1$. As the sequence becomes longer, the measured correlation $\langle\sigma_Z^{\otimes 2}\rangle$ decays exponentially to zero, indicating a maximally mixed state. The inset displays the error rate per Clifford for the standard (blue) and interleaved (red) randomized benchmarking sequence extracted from the Eq. (4.38).

Parameter	Fitted Value, RB	Fitted Value, IRB
p	(96.38 ± 0.70) %	(93.84 ± 0.81) %
A	$(9.50 \pm 0.22) \times 10^{-1}$	$(9.83 \pm 0.14) \times 10^{-1}$
B	$(1.36 \pm 0.21) \times 10^{-2}$	$(1.59 \pm 0.12) \times 10^{-2}$

Table 4.4: List of parameters and the fitted values for the standard and interleaved RB results shown in Fig. 4.22. Specifically, $1 - p$ is the depolarizing rate and the parameter A and B contain information about the state preparation and measurement errors.

The error per Clifford for RB and IRB is found to be (3.45 ± 0.23) % and (6.16 ± 0.27) % respectively, using the relation $r_{\text{Clifford}} = \frac{3}{4}p$. By comparing the depolarizing rates from RB and IRB measurements, the error per CPHASE gate can be found with

$$r = \frac{3}{4} \left(1 - \frac{p_{\text{IRB}}}{p_{\text{RB}}} \right) = (2.10 \pm 0.35) \text{ \%} \qquad (4.39)$$

Consequently, the gate fidelity is $p = 1 - r = (97.90 \pm 0.35)$ %. Considering the coherence time of the qubits presented in Table 4.2, the contribution to the gate error measured in RB due to the energy relaxation and dephasing is estimated to be around 98.9 % for a 256 ns gate time, which is calculated from Eq. (2.22) [89, 187]. However, when the flux pulse is applied to the coupler, it is possible for the coupler to cross the qubit in frequency due to the symmetrical SQUID loop design of the coupler, which will contribute to the gate error in two ways. Firstly, the effective coherence time of the qubits is reduced due to the additional dephasing induced by the flux pulse. Secondly, it becomes possible for the qubit population to leak into the coupler due to the crossing of qubit levels. This is also indicated in the population loss and leakage measured in earlier calibration experiments. While the gate mechanism is promising in principle, future design iterations are essential to continuously improve gate performances.

4.4 Summary

In conclusion, we have examined all three parametric two-qubit gates that include iSWAP, SWAP and CPHASE(CZ) theoretically and demonstrated the calibration procedure of parametric CZ in particular. Due to the parametric nature of the flux pulses used for the gate, the calibration procedure is relatively straightforward when comparing to that for the fast DC flux pulses [155]. One major drawback is the speed of the parametric gate, leading to a higher probability for the qubit to decay during the gate operation. Further investigation has been focused on this aspect of the parametric coupling system, which is an ongoing effort. By optimizing coupler design parameters and choosing a better coupler frequency during gate operation, the parametric gate has the potential for improvement in terms of both speed and performance.

CHAPTER 5

Qubit Reset and Leakage Reduction

To achieve fault-tolerant quantum computing, quantum error correction (QEC) algorithms are crucial components in preserving quantum information in a logical qubit. Among QEC algorithms, the surface code has been shown to be a promising platform in recent implementation with superconducting qubits [32–34, 44, 45]. In such a code, physical qubits are designated to be either data or ancilla qubits in a checkerboard pattern [36, 40, 41]. The data qubits store the quantum information, and are parity-checked by measuring the ancilla qubits in each error-correction cycle. Each parity check is followed by a reset operation on the ancilla qubits to return them to the ground state and prepare them for the next round of error detection. However, during the cycle, data and ancilla qubits are prone to leak outside the computational subspace, thus fatally compromising the error-correction algorithms [188–193]. Therefore, both a fast and high-fidelity reset for ancilla qubits and a leakage-reduction unit (LRU) for data qubits are instrumental for practical error correction.

Qubit reset is used to speed up the algorithm runtime as qubits' lifetime improves and the waiting time for the qubit excitation to naturally decay becomes significant [194, 195]. Qubit-reset protocols can be either conditional or unconditional depending on whether or not they require knowledge of the

qubit state. In conditional reset, qubits are reset conditioned on the measured results [196]. If the qubit population is in the first excited state $|1\rangle$, a π-pulse is sent to the qubit to drive the population back to the ground state $|0\rangle$ via real-time feedback. The primary limitation for conditional reset is the feedback time of the control electronics. However, the success rate of the feedback operation depends on the readout fidelity. In unconditional reset, qubit excited-state is depopulated regardless of its initial state [188, 192, 194, 195, 197–199]. Existing unconditional reset schemes typically require additional drive signals, flux-tunable qubits, or additional control elements on the device. These challenges lead to increased difficulties when scaling up to a larger number of qubits.

In the context of LRU, its implementation requires resetting only the $|2\rangle$-state or higher-energy states without disturbing the computational subspace. An LRU can be implemented either by directly coupling the $|2\rangle$-state population to a lossy resonator [189, 191, 200] or by performing a SWAP gate to transfer the $|2\rangle$-state population to another element on the processor [190, 192]. It is crucial to develop an LRU that complements the chosen reset strategy. Although LRUs are mainly discussed within the context of QEC, they can be applied during any quantum algorithm to reduce the accumulation of leakage errors.

In this Chapter, we present both high-fidelity unconditional qubit reset and leakage reduction in an architecture using fixed-frequency transmon qubits [66] pair-wise coupled via tunable couplers [114, 201, 202].

5.1 Unconditional Reset of Fixed-frequency Qubit

We first consider a system consisting of a fixed-frequency transmon qubit, a tunable transmon that acts as the coupler element, and a leaky resonator forming the dissipator stage. The energy levels of the two-qubit subsystem in the single-excitation manifold are sketched out in Fig. 5.1. The high-frequency qubit Q_0 is treated as the ancilla qubit that we aim to reset, and the low-frequency qubit Q_1 acts as the data qubit that needs leakage reduction. To implement the reset protocol on the ancilla qubit, the first step is to do a qubit–coupler (QC) SWAP gate where the excitation is moved from qubit Q_0 to coupler C_0. The coupler C_0 is parked above Q_0 to avoid any interaction with Q_1. Using a similar mechanism, the LRU is implemented on qubit Q_1
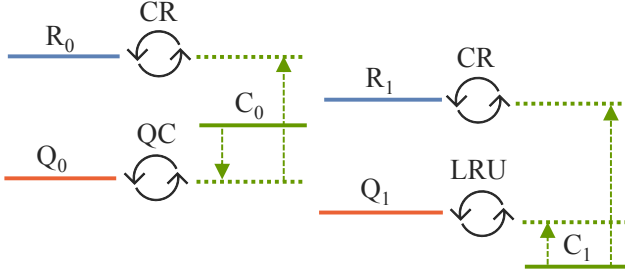
Figure 5.1: Schematic of the reset and leakage-reduction protocol with energy levels of the qubit-resonator-coupler subsystem. In a pair-wise coupled system, two fixed-frequency qubits, Q_0 and Q_1, are coupled via a frequency-tunable coupler C_0 controlled by an applied magnetic flux. Each qubit is also coupled to a dedicated readout resonator, denoted as R_0 and R_1. In the reset protocol, the coupler C_0 is first tuned on resonance with Q_0 to implement a qubit-coupler (QC) SWAP gate. Q_1 is not affected due to the relatively large detuning between the two qubits. For the leakage reduction unit (LRU), coupler C_1 is used, initially biased below the Q_1 frequency. Afterwards, both couplers are tuned to higher frequencies to interact with the resonators of either qubit to implement the coupler-resonator (CR) SWAP gate. The excitation will then decay into the environment via the readout feedline.

via coupler C_1, parked below Q_1. The QC SWAP and the LRU can be executed simultaneously on the respective qubit. Afterwards, the last step of the protocol involves the coupler–resonator (CR) SWAP gates for all couplers in parallel. The resonator excitation can then be dissipated through the feedline.

A simplified circuit diagram of this subsystem is shown in Fig. 5.2. Invoking the rotating-wave approximation (RWA), we model the qubit and the coupler as Kerr oscillators with anharmonicities α_q and α_c, respectively, and we write the system Hamiltonian as

$$
\begin{aligned}
H_{\mathrm{RWA}} = {} & \omega_r a^\dagger a + \omega_q b^\dagger b + \frac{\alpha_q}{2} b^{\dagger 2} b^2 + \omega_c c^\dagger c + \frac{\alpha_c}{2} c^{\dagger 2} c^2 \\
& + g_{qr} \left(a^\dagger b + b^\dagger a \right) + g_{qc} \left(b^\dagger c + c^\dagger b \right),
\end{aligned}
\tag{5.1}
$$

where a $(a^\dagger)$, b $(b^\dagger)$, c $(c^\dagger)$ are the annihilation (creation) operators for the resonator, qubit, and coupler, labeled by the subscripts r, q, and c, respec-
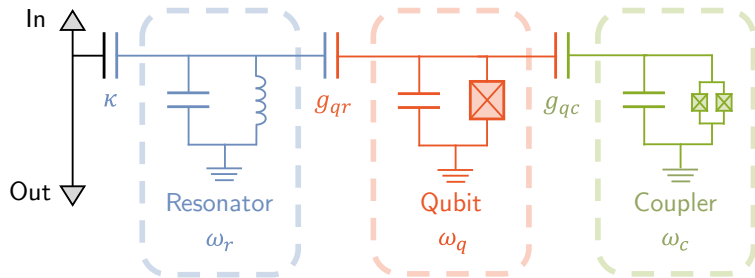
Figure 5.2: Circuit diagram of resonator-qubit-coupler subsystem. The coupler, the qubit and the resonator are coupled with strength g_{qc} and g_{qr} between each of the two elements, respectively. The resonator is coupled to the environment with strength κ via the feedline.

tively. g_{ij} denotes the coupling strength between the systems i and j. For the theoretical study, we assume that the coupler is not directly connected to the resonator. Therefore, the exchange of quanta between the coupler and resonator primarily occurs near their resonance, via second-order interactions that can be studied using the well-known Schrieffer-Wolff perturbative expansion [203].

Note that H_{RWA} is number-conserving as all the terms contain an equal number of raising and lowering ladder operators. The Hamiltonian decouples into different blocks labeled by the total number of excitations N, and each block can be studied separately. The dynamics of a qubit starting in its first-excited state can be studied within the first-excitation subspace:

$$H_1 = \begin{bmatrix} \omega_r & g_{rq} & 0 \\ g_{rq} & \omega_q & g_{qc} \\ 0 & g_{qc} & \omega_c \end{bmatrix}. \tag{5.2}$$

5.1.1 Diabatic SWAP Interactions

To understand the dynamics of the reset protocol, we start by examining the case of diabatic swap between the qubit and the coupler, which contributes to reset the $|1\rangle$-state population of the qubit. We employ both analytical and numerical tools to interpret the reset scheme when the coupler frequency is brought into resonance with the qubit on time shorter than $1/g$. To achieve

this resonant condition, we tune the coupler frequency. During the waiting time at resonance, the qubit exchanges excitations with the coupler, thus completing the first QC SWAP.

At the QC resonance, the resonator is far detuned from the qubit ($\omega_r - \omega_q \gg g_{rq}$) such that we can neglect its contribution to the dynamics during this first swap interaction. This makes the analysis even simpler as it reduces the three-level system in Eq. (5.2) to an effective two-level system (TLS) formed by the qubit and the coupler near resonance. Thus, we expect vacuum Rabi oscillations between the qubit and the coupler.

We start the protocol with the system initialized in $|1_q 0_c 0_r\rangle$, where states are labeled in the order $|$qubit, coupler, resonator$\rangle$. The effective TLS Hamiltonian in the space of states $|1_q 0_c 0_r\rangle$ and $|0_q 1_c 0_r\rangle$ interacting in the first QC SWAP is

$$H_{qc} = \begin{bmatrix} -\Delta_{qc}/2 & g_{qc} \\ g_{qc} & \Delta_{qc}/2 \end{bmatrix}, \qquad (5.3)$$

with $\Delta_{qc} = \omega_q - \omega_c$.

During the waiting time τ of the first swap, $\Delta_{qc} = 0$. Therefore, the state at time $t = \pi/2g_{qc}$ is

$$|\Psi_t\rangle = \cos(g_{qc}t) |1_q 0_c 0_r\rangle + i \sin(g_{qc}t) |0_q 1_c 0_r\rangle, \qquad (5.4)$$

with the qubit population entirely moving to the coupler at time $t = \pi/2g_{qc}$. The interaction is ideally an iSWAP gate. However, since we only consider the population transfer during reset, we can simplify the notation to be SWAP. After the first swap, the coupler is in the excited state, meaning that the coupler needs to move away from resonance near $t = \pi/2g_{qc}$, marking the end of the first swap. The coupler frequency is then ramped up to the resonator frequency to initiate the second step, to enable the interaction between the resonator and the coupler. At resonance, the coupler and the resonator undergo Rabi oscillations, which is referred to as the CR SWAP. The lossy resonator leaks out almost completely in a time of $3/\kappa$, thus emptying the resonator and completing a full reset operation.

The TLS Hamiltonian for the CR SWAP is

$$H_{cr} = \begin{bmatrix} -\Delta_{cr}/2 & g_{cr} \\ g_{cr} & \Delta_{cr}/2 \end{bmatrix}, \qquad (5.5)$$

with $\Delta_{cr} = \omega_c - \omega_r$. The resonator has a loss rate κ, which makes the evolution non-unitary and necessary to treat within the master-equation formalism. If we assume that the coupler and the resonator are not simultaneously excited, the master equation implies that the non-Hermitian Hamiltonian

$$H_{\text{eff}} = H - \mathrm{i}\frac{\kappa}{2}\mathcal{L}^\dagger\mathcal{L} \tag{5.6}$$

equivalently accounts for the dissipation. Solving its effective Schrödinger equation yields an analytical expression for the non-unitary evolution of the resonator and coupler states. Here, we consider photon loss from the resonator as the main source of dissipation. Therefore, the Lindblad operator $\mathcal{L}$ annihilates a resonator excitation, i.e., $\mathcal{L} = a$. The effective non-Hermitian Hamiltonian governing the second swap can be written as

$$H_{cr} = \begin{bmatrix} -\Delta_{cr}/2 & g_{cr} \\ g_{cr} & \Delta_{cr}/2 - \mathrm{i}\frac{\kappa}{2} \end{bmatrix}. \tag{5.7}$$

Solving the Schrödinger equation for the Hamiltonian in Eq. (5.7), we find the decay of the excited coupler wavefunction ψ_c:

$$\begin{cases} \frac{e^{-\frac{\kappa t}{4}}}{2g_{cr}}\left(\kappa\sinh\left(\frac{\sqrt{|\alpha|}t}{4}\right) + \sqrt{|\alpha|}\cosh\left(\frac{\sqrt{|\alpha|}t}{4}\right)\right), & \alpha > 0 \\ \frac{e^{-\frac{\kappa t}{4}}}{2g_{cr}}\left(\kappa\sin\left(\frac{\sqrt{|\alpha|}t}{4}\right) + \sqrt{|\alpha|}\cos\left(\frac{\sqrt{|\alpha|}t}{4}\right)\right), & \alpha < 0 \\ \frac{e^{-\frac{\kappa t}{4}}}{g_{cr}}\left(\frac{\kappa t}{4} + 1\right), & \alpha = 0 \end{cases} \tag{5.8}$$

with $\alpha = \kappa^2 - 4g_{cr}^2$. This provides important insights into the overall reset rates. One might expect that the photon decay rate and, thus, the reset speed increases with κ. As seen from Eq. (5.8), the reset can be divided into three regimes, under-damped ($\alpha < 0$), over-damped ($\alpha > 0$), and critically damped ($\alpha = 0$). In the over-damped regime, populations decay without oscillations. The decay rate is less than $\kappa/2$ as the terms inside the parenthesis, contribute to population growth and slow down the decay. In the under-damped regime, the decay is oscillatory, limiting the overall speed of population decay. The reset rate increases with κ until it hits the critical point $\kappa/g_{cr} = 2$. At the critical damping point, the population decays without oscillations. This is where we expect to get the fastest decay at a rate $\kappa/2$. The ratio $\kappa/g_{cr} = 2$ suggests the optimal point of operation in terms of the overall reset speed.

From Eqs. (5.4) and (5.8), we can derive the total reset time for the fastest case of diabatic reset when it is operated in the regime of the critical damping. At resonance, the vacuum Rabi frequency for CR exchange is $\Omega_R = 2g_{cr}$. Similarly, the vacuum Rabi frequency of the QC interaction is $\Omega_Q = 2g_{qc}$. Using the above relation, we define the total reset time to be:

$$T_{reset} = \Omega_R^{-1} + \Omega_Q^{-1} + \kappa^{-1}, \tag{5.9}$$

which can be used to estimate the reset speed for future device designs. To enable a total reset time on the order of 100 ns, a set of typical design parameters can be $\{\Omega_R/2\pi, \Omega_Q/2\pi, \kappa/2\pi\} = \{10, 60, 10\}$ MHz, which is feasible with a flip-chip architecture and Purcell-filter designs for fast readout.

5.1.2 Adiabatic Landau-Zener-Stückelberg Transitions

To understand the adiabatic component of the reset dynamics, we consider the Landau-Zener-Stückelberg (LZS) problem [204–206]. We will first describe the LZS problem and then map our system to it. Consider a TLS described by the following Hamiltonian, which varies linearly in time:

$$H_{\mathrm{LZS}} = \begin{bmatrix} \alpha t/2 & 0 \\ 0 & -\alpha t/2 \end{bmatrix}, \; E_\pm = \pm \alpha t/2,$$
$$\Psi_+ = \begin{bmatrix} 1 \\ 0 \end{bmatrix}, \; \Psi_- = \begin{bmatrix} 0 \\ 1 \end{bmatrix}. \tag{5.10}$$

Since the Hamiltonian is diagonal, solving the time evolution of the instantaneous eigenstates is straightforward ($\hbar = 1$):

$$|\Psi_\pm(t)\rangle = e^{\pm i\alpha t^2/2} |\Psi_\pm\rangle. \tag{5.11}$$

After adding a coupling strength along the off-diagonals of the Hamiltonian

$$H_{\mathrm{LZS}} = \begin{bmatrix} \alpha t/2 & g \\ g & -\alpha t/2 \end{bmatrix}, \; E_\pm = \pm\sqrt{\left(\frac{\alpha t}{2}^2\right) + g^2}, \tag{5.12}$$

the eigenstates $|\Psi_\pm\rangle$ are no longer time-independent, which leads to $\Psi_+ \to \Psi_-$ and $\Psi_+ \to \Psi_-$.
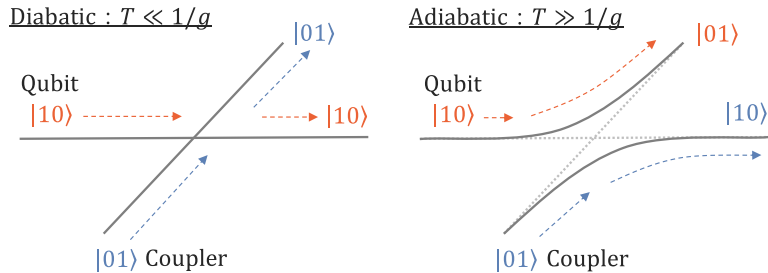
Figure 5.3: Diabatic and adiabatic transitions. The qubit and coupler energy levels are coupled with strength g. The qubit level is stationary while the coupler is transiting across in frequency for a duration T. There are two limiting scenarios in this case: 1) in fast diabatic transition (left), $gT < 1$, the population stays on its original trajectory, 2) in slow adiabatic transition (right), $gT \gg 1$, the population is swapped to the other energy level during the interaction.

The minimum energy gap between the eigenstates occurs at $t = 0$, $\delta_{\min} = 2g$. This sets the time scale for transitions, and two limiting scenarios arise, as shown in Fig. 5.3. If the transition duration is on a timescale of $T \gg 1/g$, the process is said to be adiabatic. This is the origin of the ramp-up time set to $T < 1/g$ in the diabatic swap interactions. It can be shown that the probability of a transition, a non-adiabatic effect, is

$$P_{\text{trans}} = e^{-\frac{2\pi g^2}{\hbar \alpha}}. \tag{5.13}$$

This clearly indicates that the evolution becomes more adiabatic for larger values of couplings, which can be attributed to the increase in the energy gap at the avoided level crossing.

5.2 Qubit Reset and Leakage Reduction Unit

The experimental demonstration is carried out in a two-qubit subset of a 25-qubit device, which is illustrated in Fig. 5.4. More details on the device, fabrication, and performance are provided in Refs. [114, 207]. The qubits are designed to be in two frequency groups in a checkerboard pattern, with neighbouring qubits separated in frequency by roughly 600 MHz [208]. The
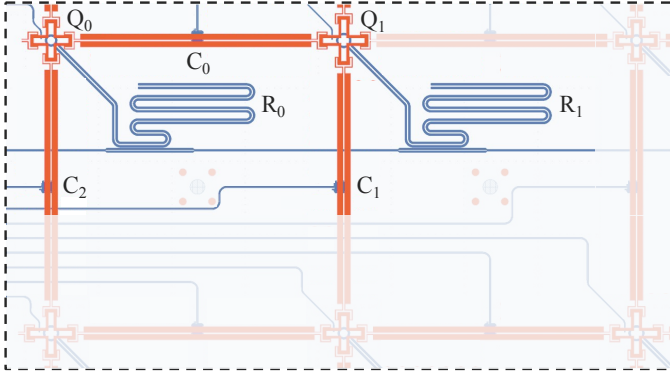
Figure 5.4: Subset of the 25-chip device under test. A pair of qubits, with their respective readout resonators and three of their surrounding couplers, are involved in the experiments. Qubit Q_0 (Q_1) is treated as the ancilla (data) qubit. Couplers C_0 and C_2 are utilized to reset qubit Q_0, and the leakage reduction unit on qubit Q_1 is implemented via coupler C_1. The device is designed and fabricated as a flip-chip architecture [114], with the elements in red placed on the qubit chip and those in blue on the control chip.

subset consists of two fixed-frequency transmon qubits Q_0 and Q_1 [66] with transition frequencies $\omega_{Q_i}/2\pi$ at 5.176 and 4.534 GHz, and anharmonicities of $\eta_{Q_i}/2\pi$ at -256 and -158 MHz for $i = 0$ and 1, respectively. Each qubit is coupled with a strength g_i to a readout resonator R_i of frequency $\omega_{R_i}/2\pi =$ 6.752 and 6.308 GHz for $i = 0$ and 1, respectively. Both resonators are coupled to the same feedline. There is a tunable coupler between each pair of qubits arranged in a square grid on the chip. In this experiment, three of the couplers (C_0, C_1, and C_2) surrounding the pair of qubits are used. The qubit-to-coupler coupling rates $g_{QC}/2\pi$ are 40 MHz (60 MHz) for qubit Q_0 (Q_1), while the qubit-resonator coupling rates $g_{QR}/2\pi$ are around 50 MHz. The coupling between the coupler and resonator has two main sources: a direct capacitive coupling due to their proximity on the chip and an indirect coupling mediated by the qubit. The sample used in our experiment is the same one as in Section 4.3, with parameters listed in Table 4.2 and Table 4.3. The complete experimental setup and full wiring diagram are detailed in **Paper B**.

For qubit reset, one main scenario to consider is the ability to reset not

just the qubit $|1\rangle$-state population, but also that of the higher energy states, due to the accumulation of leakage population outside of the computational subspace. For this reason, an adiabatic pulse is chosen to perform qubit reset due to the possibility of transferring the population from multiple energy levels simultaneously. The pulse shape is calculated from the instantaneous approximate adiabatic condition. Given a Hamiltonian $H(t)$, for any two adjacent eigenstates $|\Psi_n(t)\rangle$ and $|\Psi_m(t)\rangle$ and corresponding eigenvalues $E_n(t)$ and $E_m(t)$, the evolution with duration τ is approximately adiabatic if the following condition is met:

$$\frac{\max\limits_{0 \leq t \leq \tau} \left| \langle \Psi_n(t) | \frac{\partial H(t)}{\partial t} | \Psi_m(t) \rangle \right|}{\max\limits_{0 \leq t \leq \tau} |E_n(t) - E_m(t)|^2} \ll 1. \tag{5.14}$$

This condition implies that the changes in the interactions between the states m and n at time t must be significantly smaller than the energy distance between the states. Note that this is a global condition and can be modified to an instantaneous condition. The instantaneous approximate adiabatic condition was previously used to accelerate Grover's algorithm in adiabatic quantum computation by Roland and Cerf [209, 210], which has been studied and experimentally verified in two-level systems [211, 212].

The exact analytical solution of the adiabatic pulse is derived following the Roland and Cerf protocol to speed up the adiabatic transitions [209, 210], with an example shown and annotated in Fig. 5.5(a). Assuming that the adiabatic condition in Eq. (5.14) is satisfied for every infinitesimal time interval from t to $t + dt$, we arrive at

$$\left| \left\langle \Psi_n(t) \left| \frac{\partial H(t)}{\partial t} \right| \Psi_m(t) \right\rangle \right| \ll |E_n(t) - E_m(t)|^2. \tag{5.15}$$

For a two-level system (TLS) with coupling strength g that is described by the Hamiltonian

$$H_{\mathrm{TLS}}(t) = \hbar \begin{bmatrix} \Delta(t)/2 & g \\ g & -\Delta(t)/2 \end{bmatrix}, \tag{5.16}$$

the adiabatic condition, defined by Eq. (5.15), is:

$$\left| \frac{\partial \Delta(t)}{\partial t} \right| \ll \frac{(\Delta^2(t) + 4g^2)^{\frac{3}{2}}}{g}. \tag{5.17}$$
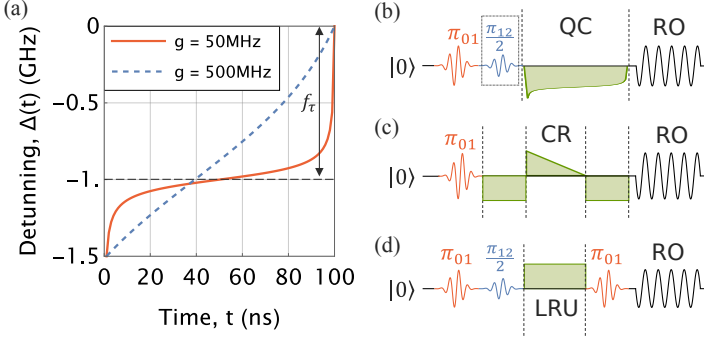
Figure 5.5: Calibration sequences of the reset protocols with adiabatic pulses. (a) The adiabatic pulse for the qubit-coupler (QC) reset SWAP is defined by Eq. (5.19) with four parameters: the pulse duration $\tau = 100$ ns, the coupler frequency offset, $f_\tau = -1$ GHz, the QC coupling strength, g, and the QC detuning that defines the start of the adiabatic process, $f_0 = -1.5$ GHz. In particular, f_τ is essentially the amplitude of the flux pulse. The coupler is first pulsed to be below Q_0, and then crossing the Q_0 energy level adiabatically before returning to the idle position. The pulse schemes to calibrate the **(b)** qubit-coupler (QC) SWAP, **(c)** coupler-resonator (CR) SWAP and **(d)** leakage reduction unit (LRU) include π_{01} (red) and $\pi_{12}/2$ (blue) pulses to prepare the qubit state, the flux pulses (filled areas in green) applied on the coupler, and the readout (RO) pulses on the resonator (black).

We then find the qubit-coupler detuning $\Delta(t)$ for implementing adiabatic evolution. The differential equation can be solved by multiplying a scaling prefactor β to its right-hand side:

$$\left| \frac{\partial \Delta(t)}{\partial t} \right| = \beta \frac{(\Delta^2(t) + 4g^2)^{\frac{3}{2}}}{g}. \tag{5.18}$$

Therefore, given the boundary conditions for a pulse duration of τ, which are denoted as $\Delta(0) = f_0$ and $\Delta(\tau) = f_\tau$, one can find the solution to Eq. (5.18) for the instantaneous adiabatic evolution to be

$$\Delta(t) = -\frac{8g(\beta g \cdot t + \delta)}{\sqrt{1 - 16(\beta g \cdot t)^2 - 32\beta\delta g \cdot t - 16\delta^2}}, \tag{5.19}$$

with

$$\beta = \frac{-4\delta(f_\tau^2 + 4g^2) - f_\tau\sqrt{f_\tau^2 + 4g^2}}{4g\tau(f_\tau^2 + 4g^2)}, \qquad (5.20)$$

$$\delta = -\frac{f_0}{\sqrt{16f_0^2 + 64g^2}}. \qquad (5.21)$$

Trajectories similar to Eq. (5.19) based on the Roland and Cerf protocol can also be found in Refs. [209, 212–215].

The pulse can be defined by four parameters: τ is the pulse duration, f_0 is the coupler frequency offset from the idle point, f_τ is the qubit-coupler detuning before the start of the pulse, and g is the qubit-coupler coupling strength that defines the slope of the center region of the pulse. In practice, the coupling parameter g can be treated as an adjustable variable to be optimized for better reset performance. With increasing g, the pulse gradually transforms from a square pulse with an extra tail to a linear ramp pulse, so that we have the full range to tune the adiabaticity of the transition induced by this pulse.

5.2.1 Qubit-Coupler SWAP Gate

The first step of our reset protocol is to transfer the $|1\rangle$-state population of qubit Q_0 to coupler C_0, as shown in Fig. 5.5(b). We first bias the coupler C_0 to be at least 1 GHz above Q_0 and below its resonator R_0, which would be the common idling point chosen for implementing a parametric two-qubit gate. We prepare Q_0 in $|1\rangle$ (without the $\pi_{12}/2$-pulse at this stage) and then implement a QC SWAP operation between Q_0 and C_0 by applying the adiabatic flux pulse in Eq. (5.19), which is given by the solution of Eq. (5.14). The pulse induces a population transfer between qubit and coupler, which is ideally adiabatic.

To tune-up the QC SWAP gate, we need to acquire the pulse parameters in two separate 2D sweeps, since four parameters are needed to define the pulse. For each sweep, we define the reset error ϵ_{reset} to be the residual non-ground-state population after the operation, $1 - p_0$, where p_0 is the measured $|0\rangle$-state population of Q_0. We use the reset error as the figure of merit for the calibration.

We first measure the reset error as a function of the pulse duration τ_{QC} and the coupler frequency detuning f_τ. We set f_0 and g to be 200 MHz
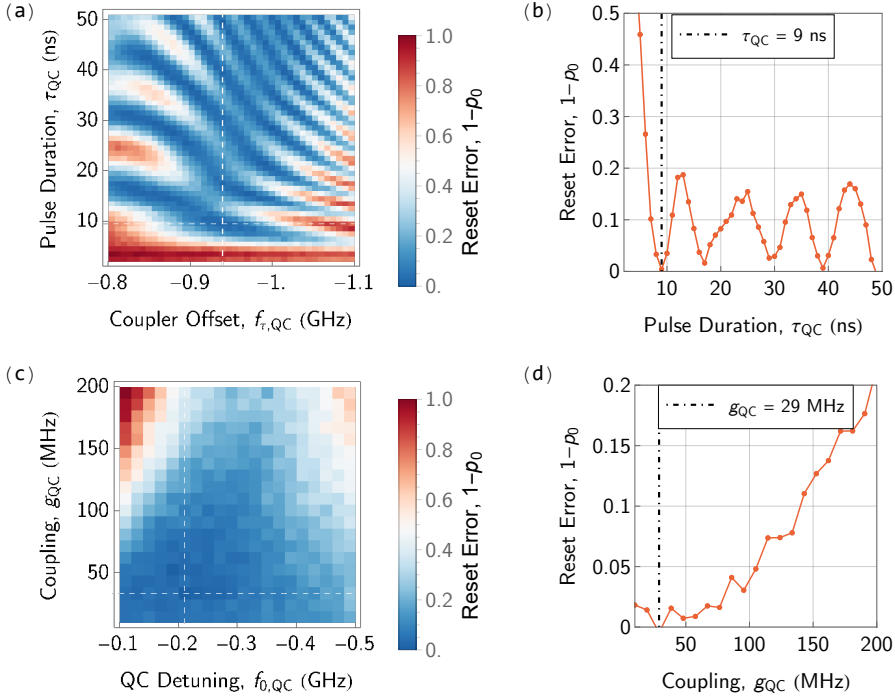
Figure 5.6: Calibration results of qubit-coupler (QC) SWAP. The measurement results of the qubit-coupler (QC) SWAP are shown. The pulse sequence of the measurement is shown in Fig. 5.5(b). The qubit is initialized in the $|1\rangle$ state. For the 2D parameter sweeps, the colour represents the reset error, which takes all non-ground state populations into account, and the regions with lower reset errors are always indicated in blue. The line cut in **(b,d)** indicates the cross-section of the optimal parameters taken from the 2D sweep marked with a vertical white dashed line.

and 71 MHz, respectively, given preliminary qubit and coupler spectroscopy results. The reset error as a function of τ_{QC} and f_τ is shown in Fig. 5.6(a), and a chevron pattern illustrating population transfer from the qubit to the coupler $|1\rangle$-state is observed. A line-cut of the first minimum in reset error is displayed in Fig. 5.6(b) to demonstrate the time evolution of the population. We then fix τ_{QC} and f_τ to be the values that produce the lowest reset error, and sweep both g and f_0 to refine the pulse shape, as shown in Fig. 5.6(c-d). A large
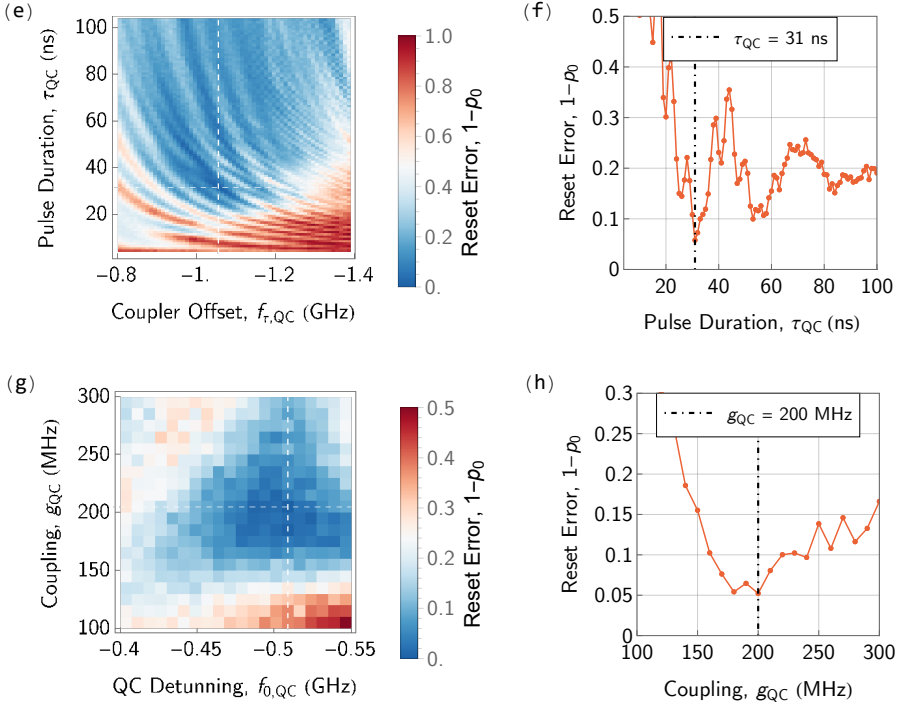
Figure 5.7: Calibration results of qubit-coupler (QC) SWAP for $|2\rangle$-state reset. The pulse sequence of the measurement is shown in Fig. 5.5(b). The qubit is initially prepared in a $(|1\rangle + |2\rangle)/\sqrt{2}$ superposition state.

parameter space, with g being below 50 MHz and f_0 being around -200 MHz, can be identified where the reset error approaches the readout limit. These initial results suggest that the fidelity of this swap operation can be above 99%, limited by drifting qubit parameters and coupler flux bias currents. We achieve depopulation of the $|1\rangle$ state with a 9 ns QC SWAP gate between the ancilla qubit and the coupler. The data qubit, Q_1, is only negligibly affected by the flux pulse, since it is 642 MHz lower in frequency than the ancilla qubit. Therefore, the reset of the ancilla qubit can be performed independently of the state of the data qubit.

To show how we can reset both the $|1\rangle$-state and $|2\rangle$-state population of the ancilla qubit simultaneously, we prepare the ancilla in a superposition state

$(|1\rangle + |2\rangle)/\sqrt{2}$ with an additional $\pi_{12}/2$-pulse [see Fig. 5.5(b)] so that the effect on both states is visible with a single measurement. The coupler interacts with multiple qubit levels during the frequency tuning. The results are shown in Fig. 5.7. There is a relatively small parameter space for a fast reset on the order of 31 ns due to interaction between both qubit $|1\rangle$- and $|2\rangle$-state population with the coupler, with around 5% of the population remaining at the $|1\rangle$ state while the rest is in the $|0\rangle$ state. This is due to the proximity of the data qubit Q_1 to Q_0 in frequency, limiting the furthest extent of the adiabatic pulse and thus the adiabadicity of the pulse. Therefore, we are able to reset both the $|1\rangle$ and the $|2\rangle$ states with the same pulse parameters, although the reset of the $|2\rangle$ state is only partially complete with a single pulse.

To improve the reset fidelity, we repeat the same reset scheme with another coupler. In practice, the implementation is realized with coupler C_0 and coupler C_2, both of which are coupled to qubit Q_0. Assuming that the $|1\rangle$-state reset is ideal, the reset success probability is $1 - 2 \cdot 0.05 = 90\%$ for a pure $|2\rangle$ state. From this, we can estimate that two successive reset operations with similar success probability can achieve a total fidelity of $1 - 0.1^2 = 99\%$, albeit at the cost of double the time.

5.2.2 Coupler-Resonator SWAP Gate

The next step of the reset protocol is to remove the excitation in the coupler by resonant interaction with the qubit readout resonator, as shown in Fig. 5.1. Due to the direct capacitive coupling between the coupler and the qubit read-out resonator and indirect coupling mediated by the qubit, it is possible to implement this scheme without changing the architecture of the device.

To calibrate the coupler-resonator SWAP, we implement the pulse sequence shown in Fig. 5.5(c). We first prepare the ancilla qubit in the $|1\rangle$ state and then apply the reset flux pulse, starting with a QC SWAP to populate the coupler. A diabatic square pulse is preferable here during the calibration since it is easier to observe the oscillation of the excitation between the qubit and the coupler. Afterwards, we implement a linear-ramp pulse to perform the CR SWAP to induce adiabatic transfer, due to the simpler nature of the frequency landscape of the resonators. The amplitude of the CR SWAP flux pulse has the opposite sign of the QC SWAP pulse in order to interact with the resonator levels that are higher in frequency. We add an extra QC SWAP
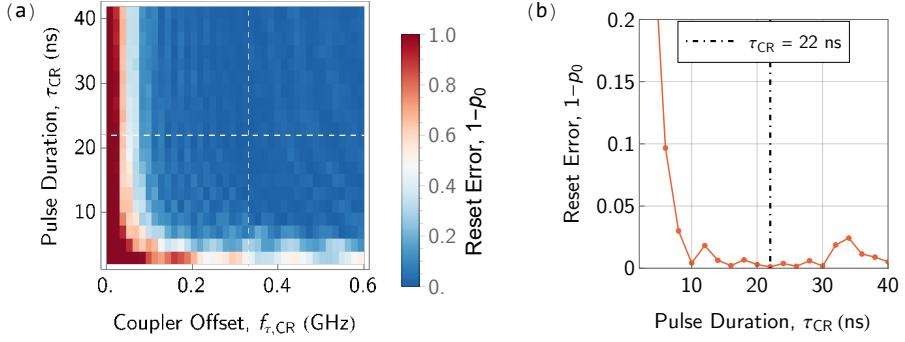
Figure 5.8: Calibration results of coupler-readout resonator (CR) SWAP. The pulse sequence of each measurement is shown in Fig. 5.5(c). The qubit is initialized in the $|1\rangle$ state.
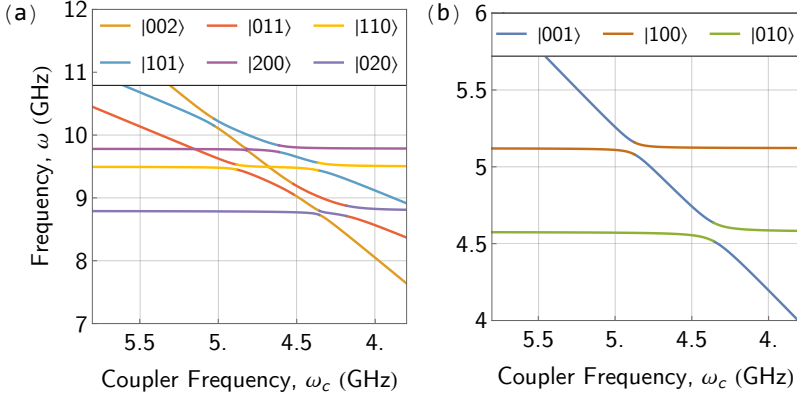
Figure 5.9: Simulated energy spectrum of the Q_0-Q_1-C_0 system and QC SWAP with a square flux pulse. (a) Energy spectrum that involves two-excitation states such as $|002\rangle$, $|011\rangle$, $|110\rangle$, $|101\rangle$, $|200\rangle$, and $|020\rangle$ as a function of the coupler frequency. These states represent different combinations of excitations distributed among the two qubits and the coupler. **(b)** Energy spectrum of the single-excitation states $|001\rangle$, $|100\rangle$, and $|010\rangle$, which involve a single excitation localized in either Q_0, Q_1, or C_0.

pulse after the CR SWAP pulse to move the residual population in the coupler back to the ancilla qubit so that its population can be read out.

The coupler is reset to its ground state $|0_c\rangle$ after 20 ns, as shown in Fig. 5.8,
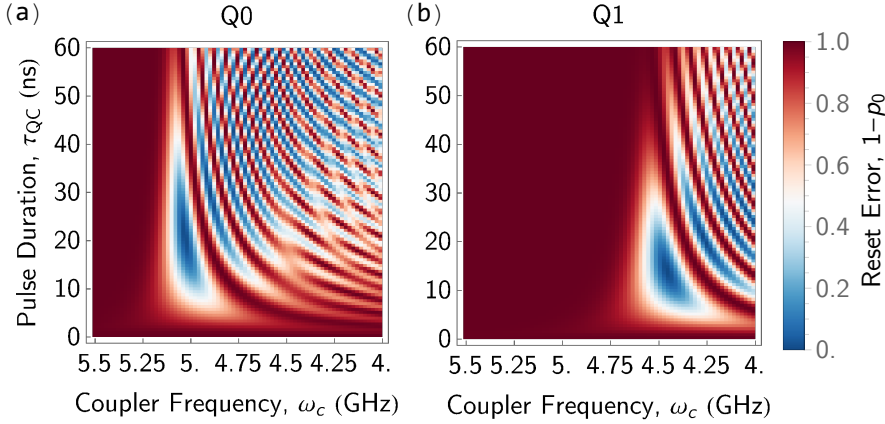
Figure 5.10: QC SWAP with a diabatic flux pulse. Reset error for the qubit **(a)** Q_0 and **(b)** Q_1. The color scale represents the reset error, defined as $1 - p_0$, where p_0 is the probability of the qubit being in the ground state after the reset protocol. The heatmaps illustrate how the state-transfer dynamics and subsequent reset errors depend on the interaction between the qubits and the tunable coupler. Darker regions (red) indicate higher reset errors, while lighter regions (blue) signify more efficient resets with lower error rates.

with reset error reaching below the readout floor at 10^{-4} for a relatively large parameter space. We choose a pulse duration of 22 ns for robustness against fluctuations over time. Note that the CR SWAP can be applied to all couplers simultaneously to reduce sequence time.

5.2.3 Data Qubit Response

One limiting constraint on the adiabaticity of the reset pulse is the frequency spacing between the two qubits. First, we simulate the effect of the coupler frequency-tuning to understand the system behaviour in the regime when the coupler interacts with both qubits [216]. The simulated energy spectrum of the Q_0-Q_1-C_0 system is shown in Fig. 5.9, consisting of the two fixed-frequency transmon qubits, Q_0 and Q_1, coupled via the tunable coupler C_0. In this architecture, the coupler frequency (ω_c) can be adjusted to control the interactions between the qubits, enabling dynamical control over the energy levels of the system. As the coupler frequency is tuned, the energy levels shift,
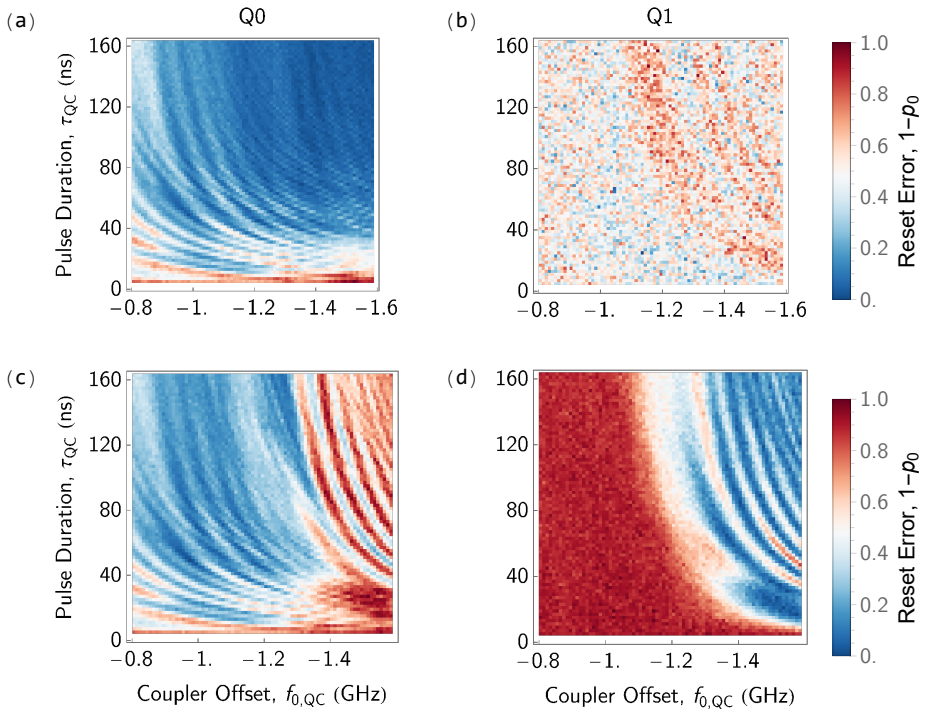
Figure 5.11: Adiabatic pulse performance with respect to the excitation on the data qubit. In **(a-b)** (**(c-d)**), Q_1 is initially prepared in $|0\rangle$ ($|1\rangle$)-state. The interaction between the coupler and Q_0 varies much differently depending on the state of Q_1. The coupling strength parameter g is set to 1 GHz for both measurements to approximate a linear ramp pulse.

displaying several avoided level crossings where the states interact strongly, highlighting the tunable coupling mechanism.

The avoided crossings between the states $|200\rangle$, $|101\rangle$, and $|002\rangle$ in Fig. 5.9(a), as well as $|100\rangle$ and $|001\rangle$ in Fig. 5.9(b), are of particular interest as they provide a pathway for adiabatic state transfer between qubit Q_0 and the coupler C_0. By slowly varying the coupler frequency, the system can transition between these states without occupying intermediate levels, facilitating a controlled swap of an excitation from qubit Q_0 to the coupler C_0. This mechanism is crucial for our approach in unconditional reset of the qubit Q_0.

We then simulate reset errors of qubits Q_0 and Q_1 as a function of the coupler frequency (ω_c) and pulse duration (τ_{QC}) for a square flux pulse. The result is shown in Fig. 5.10. The simulation result shows that Q_1 is not affected by the reset pulse given that one chooses ω_c and τ_{QC} to best reset Q_0.

However, due to the anharmonicity of the transmon, the higher energy transitions have a multitude resonant interactions with the coupler states as shown in Fig. 5.9(a). It becomes difficult to reset both the $|1\rangle$- and $|2\rangle$-state population of the qubit with a single diabatic pulse. Therefore, we need to examine the feasibility to reset multiple qubit states with adiabatic transfer instead.

Experimentally, we can measure the effect of the applied adiabatic pulse on the data qubit directly. In Fig. 5.11, two sets of measurements are carried out for the same reset pulse with Q_1 initially prepared in either $|0\rangle$ [Fig. 5.11(a-b)] or $|1\rangle$ [Fig. 5.11(c-d)]. We observe that the parameter space available for a complete reset for Q_0 in Fig. 5.11(a) is much larger than that in Fig. 5.11(c). The transition in this regime is fully adiabatic, indicated by the fact that there are no oscillations occurring at a longer pulse duration.

However, reset pulses with these parameters move the coupler too close to the Q_1 frequency, resulting in significant undesirable interaction with Q_1, as shown more prominently in Fig. 5.11(d). Therefore, in order to protect the $|1\rangle$-state population of Q_1, we choose to operate in the regime indicated by Fig. 5.11(c). This constraint increases the calibration difficulty and potentially decreases long-term stability in large devices.

5.3 Leakage Reduction Unit with Diabatic Pulse

Leakage in the data qubits is a major error source in any error-correction scheme. Therefore, a protocol to specifically target the $|2\rangle$ state of data qubits without disrupting the $|1\rangle$-state population is necessary for successful error correction. An LRU on the data qubit Q_1 can be implemented by moving the coupler C_1 to where the $|1_1 1_c\rangle$ and $|2_1 0_c\rangle$ states of the Q_1-C_1 system are on resonance, as shown in Fig. 5.1. The coupler C_1 that implements the LRU is parked below the data qubit, to avoid disruption of its $|1\rangle$-state population.

The specific pulse scheme is shown in Fig. 5.5(d). We prepare Q_1 in the $(|1\rangle + |2\rangle)/\sqrt{2}$ superposition state, and apply the flux pulse to move the coupler C_1 such that the $|2_1 0_c\rangle$ state is on resonance with the $|1_1 1_c\rangle$ state. The LRU
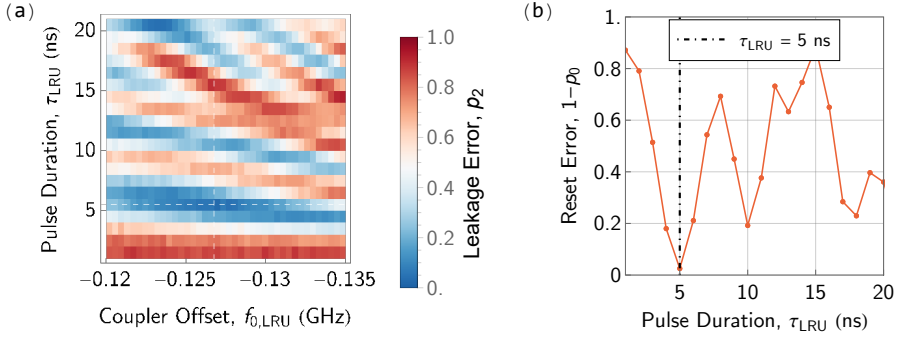
Figure 5.12: Calibration results of leakage reduction protocol. The pulse sequence of each measurement is shown in Fig. 5.5(d). The qubit is initialized in the $|2\rangle$ state.

pulse shape is chosen to be a simple square pulse such that the interaction is fast and diabatic. This minimizes the effect on the qubit $|1\rangle$-state population. An extra π_{01} pulse is added after the LRU, since the readout fidelity is higher when measuring the $|0\rangle$-state population. The results in Fig. 5.12 show that it takes 5 ns to complete the population swapping from the $|2_1 0_c\rangle$ to the $|1_1 1_c\rangle$ state.

Furthermore, the LRU can be implemented simultaneously with the reset pulse on the ancilla qubit, since it uses a different coupler, C_1. Similarly to the reset protocol, after interacting with the qubits, all couplers are made to adiabatically interact with the resonators simultaneously to transfer the couplers' population.

5.4 Single-Shot Verification

To fully characterize the reset and LRU performance, we prepare the data and ancilla qubits in all nine combinations of two-qubit states in the first and second excitation manifolds, i.e., $|0_0 0_1\rangle$, $|0_0 1_1\rangle$, $|0_0 2_1\rangle$, etc. Then we execute the full reset protocol, including $|1\rangle$- and $|2\rangle$-state QC SWAP, CR SWAP, and LRU with the two qubits (Q_0 and Q_1) and the three couplers (C_0, C_1, and C_2), as shown in Fig. 5.13(a). With the measurement protocol established, we employ the CMA-ES algorithm to optimize the pulse parameters g, f_τ, and f_0 to achieve a lower reset error [217].
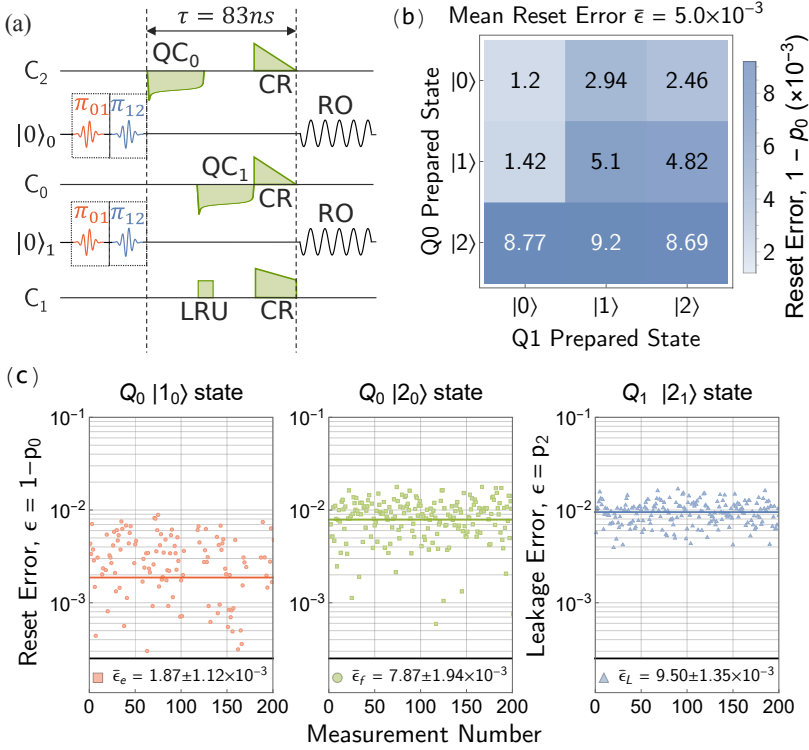
Figure 5.13: Pulse sequence and performance verification with single-shot readout. (a) The pulse sequences include state preparation of two qubits, flux pulses applied on three couplers for reset and leakage reduction, and the readout of qubit population. The total duration of the flux pulse sequence is 83 ns. All 9 combinations of two-qubit initial states in the first and second excitation manifold are prepared and measured. **(b)** Single-shot readout results of resetting all 9 two-qubit states. The mean reset error is calculated from the average of all combinations. **(c)** Long-term single-shot readout results for the 3 out of 9 combinations where Q_0 is prepared in the $|1\rangle$- or $|2\rangle$-state, or Q_1 is prepared in the $|2\rangle$-state respectively. The measurement is repeated 200 times to test the stability of the protocol.

Time-wise, resetting only the $|1\rangle$ state of the ancilla qubit requires only 9 ns. However, to reset both the $|1\rangle$ and $|2\rangle$ states, we need to apply flux pulses on couplers C_0 and C_2 sequentially; these pulses are 31 ns and 30 ns long, respectively. The CR SWAP takes 22 ns while the leakage reduction

unit needs a 5-ns-long pulse, which can start at the same time as the QC SWAP pulses. Therefore, the total time needed to implement both reset and LRU is 83 ns.

Each of the nine states is prepared and measured for 10,000 shots with single-shot readout. The results for each measurement are illustrated as a matrix in Fig. 5.13(b). To understand the long-term stability and error margin, the results are gathered from 200 repeated measurements as illustrated in Fig. 5.13(c). We average over the three out of nine combinations of the initial state where Q_0 is prepared in the $|1\rangle$ or $|2\rangle$ state, or Q_1 is prepared in the $|2\rangle$ state, to trace out the effect of the different input states. On average, the adiabatic reset protocol achieves a reset error of 1.87×10^{-3} (7.87×10^{-3}) for the $|1\rangle$ ($|2\rangle$) state. Meanwhile, the leakage reduction reaches an error of 9.50×10^{-3}. Over time, all three components are robust against random fluctuations during the span of at least a few hours.

5.5 Summary

In summary, we have implemented a fast, high-fidelity, and unconditional qubit reset protocol on fixed-frequency qubits with a tunable coupler. Using adiabatic pulses, our reset protocol achieves a reset error of $(1.87\pm1.12)\times10^{-3}$ for the $|1\rangle$ state within 9 ns, and $(7.87\pm1.94)\times10^{-3}$ for the $|2\rangle$ state in 61 ns. We also perform leakage reduction, on the qubit in 5 ns with a remaining leakage error of $(9.50\pm1.35)\times10^{-3}$. Afterwards, the population in the coupler can be transferred to the readout resonator in 22 ns. In total, the combination of qubit reset, leakage reduction and coupler reset takes only 83 ns to complete. The reset error we achieved is below the suggested threshold for quantum error correction [218], which is between 10^{-2} to $10^{-2.5}$, together with the additional benefit of removing leakage in both ancilla and data qubits. The reset and LRU fidelities are also comparable with the state-of-the-art result from Google with tunable qubits, which are 99.86% and 98.9%, respectively [188, 190]. The reset pulses are straightforward to tune up, with at most four parameters completely defining the entire pulse shape. Moreover, the reset of the ancilla qubits and the leakage reduction unit of the data qubits can run simultaneously to achieve maximal efficiency due to the usage of all available coupler elements.

The main limitation on the fidelity of the reset protocol is found to be

the frequency separation of the qubit pair. With only 642 MHz of spacing between the two qubits, the adiabatic pulses have a limited frequency range to evolve back to the initial state of the coupler in the dispersive regime, which leads to an incomplete adiabatic transition. Another limiting factor for the LRU is the small anharmonicity of the couplers on the current device, $\eta_c = 82$ MHz, which affects the undesirable interaction with the $|1\rangle$ state of the data qubits. Further design iterations and development in pulse-shaping techniques to alleviate these undesirable effects are currently under investigation with more theoretical simulations and better parameter-optimization algorithms.

To see how to scale up the reset and LRU protocol in the surface code implementation based on a 2D square grid, we can start by estimating the ratio between the number of qubits and couplers. For a code distance d, there will be d^2 data qubits, $d^2 - 1$ ancilla qubits, and $c_d = 4d(d-1)$ couplers. The reset and LRU protocol will need $c_r = 3 \cdot d^2 - 1$ couplers to fully implement the scheme. For $d > 3$, c_d is always greater than c_r, thus guaranteeing the implementation of our protocol without the need for additional elements. Moreover, we have recently demonstrated [207] that our processor has a low level of crosstalk, thus, enabling us to further scale up our design. In conclusion, we have demonstrated that the architecture with fixed-frequency qubits and tunable couplers is compatible with quantum error-correction schemes and subsequent fault-tolerant quantum computing.

CHAPTER 6

Conclusion

In this thesis, we mainly address two critical challenges in quantum computing: high-fidelity readout and efficient on-demand qubit reset. These improvements are essential steps towards realizing fault-tolerant quantum computation.

Our readout strategy exploits the higher energy levels of the qubit [65, 95, 106, 115, 117, 119] and introduces a two-tone probing of the resonator to enhance the readout fidelity of multiple states. We demonstrate single-shot readout fidelity up to 99.5 % (96.9 %) for two-state (three-state) discrimination within 140 ns without using a quantum-limited amplifier. The techniques we present here offer significant protection against decay during readout, are straightforward to implement, and can be readily integrated in state-of-the-art quantum-computing devices.

We also propose and demonstrate a reset and leakage reduction scheme that utilizes the tunable coupler as a mean to transfer excitations from a qubit to its readout resonator, from which the excitations can then decay into the feedline. Remarkably, we show that all operations have negligible impact on the other qubits on the chip and are easy to implement with the current fixed-frequency qubits and tunable-coupler architecture without the need for any additional hardware resources. We demonstrate a fast semi-adiabatic $|1\rangle$- to $|0\rangle$-state

reset with an error of $(1.87 \pm 1.12) \times 10^{-3}$ within 9 ns, and an adiabatic reset that can also move both the $|1\rangle$- and $|2\rangle$-state populations to the $|0\rangle$ state at the same time, reaching a $(7.87 \pm 1.94) \times 10^{-3}$ error within 61 ns. We also show a Leakage Reduction Unit (LRU), that removes the $|2\rangle$-state population back to the $|1\rangle$ state without disrupting the computational subspace of the data qubits with an error of 9.50×10^{-3} in 5 ns, and a coupler reset scheme that dissipates the excitation through the qubit readout resonator within 22 ns. Notably, we can simultaneously reset the ancilla qubits and perform leakage reduction of the data qubits in a total time of 83 ns.

Combined with high-fidelity single-qubit gates and parametric two-qubit operations (iSWAP, SWAP, CZ), these advancements establish a robust framework for fault-tolerant quantum computing. The integration of rapid readout, unconditional reset, leakage reduction, and precise control gates positions our chip architecture at the forefront for future demonstrations of quantum error correction algorithms.

For the published work included in this thesis, my contributions are listed in the following:

- **Paper A**: Chen, L. et al. Fast unconditional reset and leakage reduction in fixed-frequency transmon qubits. *arXiv* **2409**, 16748 (2024).

  - I developed the idea, designed the experiment, measured the device and analyzed the results.

- **Paper B**: Chen, L. et al. Transmon qubit readout fidelity at the threshold for quantum error correction without a quantum-limited amplifier. *npj Quantum Information* **9**, 26 (2023).

  - I developed the idea, designed the experiment, measured the device and analyzed the results.

- **Paper C**: Kosen, S. et al. Signal Crosstalk in a Flip-Chip Quantum Processor. *PRX Quantum* **5**, 030350 (2024).

  - I contributed with design review, I set up and maintained the measurement and cryogenic facilities.

- **Paper D**: Kosen, S. et al. Building blocks of a flip-chip integrated superconducting quantum processor. *Quantum Science and Technolgy* **7**, 035018 (2022).

- I contributed with design review, implemented readout optimization techniques, and discussed the interpretation of the results.

- **Paper E**: Krizan, C. et al. Quantum SWAP gate realized with CZ and iSWAP gates in a superconducting architecture. *arXiv* **2412**, 15022 (2024).

  - I improved single-shot readout optimization and implemented error mitigation techniques. I was also involved in gates' implementation and interpretation of the results.

- **Paper F**: Nilsson, H. R. et al. A small footprint travelling-wave parametric amplifier with a high Signal-to-Noise Ratio improvement in a wide band. *arXiv* **2408**, 16366 (2024).

  - I developed single-shot readout performance characterization and optimization techniques.

In addition, I significantly contributed to the tergite automatic calibration [219], developed in collaboration with Chalmers Next Lab, by producing several calibration nodes and analysis.

References

[1] M. A. Nielsen and I. L. Chuang, *Quantum Computation and Quantum Information*. Cambridge university press, 2010.

[2] J. Preskill, "Quantum computing in the NISQ era and beyond," *Quantum*, vol. 2, p. 79, Aug. 2018, ISSN: 2521-327X.

[3] R. P. Feynman, "Quantum mechanical computers," *Foundations of Physics*, vol. 16, no. 6, pp. 507–531, Jun. 1986, ISSN: 1572-9516.

[4] A. Montanaro, "Quantum algorithms: An overview," *npj Quantum Information*, vol. 2, no. 1, p. 15 023, Jan. 2016, ISSN: 2056-6387.

[5] J. J. Sakurai and J. Napolitano, *Modern Quantum Mechanics*, 3rd ed. Cambridge University Press, 2020.

[6] C. H. Bennett and G. Brassard, "Quantum cryptography: Public key distribution and coin tossing," *Theoretical Computer Science*, vol. 560, pp. 7–11, 2014, Theoretical Aspects of Quantum Cryptography – celebrating 30 years of BB84, ISSN: 0304-3975.

[7] A. Einstein, B. Podolsky, and N. Rosen, "Can quantum-mechanical description of physical reality be considered complete?" *Phys. Rev.*, vol. 47, pp. 777–780, 10 May 1935.

[8] R. F. Werner, "Quantum states with Einstein-Podolsky-Rosen correlations admitting a hidden-variable model," *Physical Review A*, vol. 40, pp. 4277–4281, 8 Oct. 1989.

[9] J. S. Bell, "On the einstein podolsky rosen paradox," *Physics Physique Fizika*, vol. 1, pp. 195–200, 3 Nov. 1964.

[10] J. F. Clauser, M. A. Horne, A. Shimony, and R. A. Holt, "Proposed experiment to test local hidden-variable theories," *Physical Review Letters*, vol. 23, pp. 880–884, 15 Oct. 1969.

[11] V. Vedral, "The role of relative entropy in quantum information theory," *Rev. Mod. Phys.*, vol. 74, pp. 197–234, 1 Mar. 2002.

[12] A. Y. Kitaev, "Quantum computations: Algorithms and error correction," *Russian Mathematical Surveys*, vol. 52, no. 6, pp. 1191–1249, 1997.

[13] P. W. Shor, "Polynomial-time algorithms for prime factorization and discrete logarithms on a quantum computer," *SIAM Journal on Computing*, vol. 26, no. 5, pp. 1484–1509, 1997.

[14] L. K. Grover, "A fast quantum mechanical algorithm for database search," in *Proceedings of the Twenty-Eighth Annual ACM Symposium on Theory of Computing*, ser. STOC '96, Philadelphia, Pennsylvania, USA: Association for Computing Machinery, 1996, pp. 212–219, ISBN: 0897917855.

[15] D. Deutsch, A. Ekert, R. Jozsa, J. I. Cirac, P. Zoller, and J. F. Poyatos, "Concepts of quantum computation," in *The Physics of Quantum Information: Quantum Cryptography, Quantum Teleportation, Quantum Computation*, D. Bouwmeester, A. Ekert, and A. Zeilinger, Eds. Berlin, Heidelberg: Springer Berlin Heidelberg, 2000, pp. 93–132, ISBN: 978-3-662-04209-0.

[16] R. Manenti and M. Motta, *Quantum Information Science*. Oxford University Press.

[17] D. P. DiVincenzo, "The physical implementation of quantum computation," *Fortschritte der Physik*, vol. 48, no. 9-11, pp. 771–783, 2000.

[18] D. Keith, M. G. House, M. B. Donnelly, T. F. Watson, B. Weber, and M. Y. Simmons, "Single-shot spin readout in semiconductors near the shot-noise sensitivity limit," *Phys. Rev. X*, vol. 9, p. 041003, 4 Oct. 2019.

[19] D. Loss and D. P. DiVincenzo, "Quantum computation with quantum dots," *Physical Review A*, vol. 57, pp. 120–126, 1 Jan. 1998.

[20] R. Hanson, O. Gywat, and D. D. Awschalom, "Room-temperature manipulation and decoherence of a single spin in diamond," *Phys. Rev. B*, vol. 74, p. 161 203, 16 Oct. 2006.

[21] M. V. G. Dutt *et al.*, "Quantum register based on individual electronic and nuclear spin qubits in diamond," *Science*, vol. 316, no. 5829, pp. 1312–1316, 2007.

[22] A. Imamoglu *et al.*, "Quantum information processing using quantum dot spins and cavity qed," *Physical Review Letters*, vol. 83, pp. 4204–4207, 20 Nov. 1999.

[23] R. Hanson, L. P. Kouwenhoven, J. R. Petta, S. Tarucha, and L. M. K. Vandersypen, "Spins in few-electron quantum dots," *Rev. Mod. Phys.*, vol. 79, pp. 1217–1265, 4 Oct. 2007.

[24] D. Jaksch and P. Zoller, "The cold atom hubbard toolbox," *Annals of Physics*, vol. 315, no. 1, pp. 52–79, 2005, Special Issue, ISSN: 0003-4916.

[25] C. Gross and I. Bloch, "Quantum simulations with ultracold atoms in optical lattices," *Science*, vol. 357, no. 6355, pp. 995–1001, 2017.

[26] J. I. Cirac and P. Zoller, "Quantum computations with cold trapped ions," *Physical Review Letters*, vol. 74, pp. 4091–4094, 20 May 1995.

[27] R. Blatt and C. F. Roos, "Quantum simulations with trapped ions," *Nature Physics*, vol. 8, no. 4, pp. 277–284, Apr. 2012, ISSN: 1745-2481.

[28] M. H. Devoret, A. Wallraff, and J. M. Martinis, "Superconducting qubits: A short review," *arXiv*, 2004.

[29] R. J. Schoelkopf and S. M. Girvin, "Wiring up quantum systems," *Nature*, vol. 451, no. 7179, pp. 664–669, Feb. 2008, ISSN: 1476-4687.

[30] J. Clarke and F. K. Wilhelm, "Superconducting quantum bits," *Nature*, vol. 453, no. 7198, pp. 1031–1042, Jun. 2008, ISSN: 1476-4687.

[31] A. Blais, S. M. Girvin, and W. D. Oliver, "Quantum information processing and quantum optics with circuit quantum electrodynamics," *Nature Physics*, vol. 16, no. 3, pp. 247–256, Mar. 2020, ISSN: 1745-2481.

[32] S. Krinner *et al.*, "Realizing repeated quantum error correction in a distance-three surface code," *Nature*, vol. 605, no. 7911, pp. 669–674, May 2022, ISSN: 1476-4687.

[33]   R. Acharya *et al.*, "Suppressing quantum errors by scaling a surface code logical qubit," *Nature*, vol. 614, no. 7949, pp. 676–681, Feb. 2023, ISSN: 1476-4687.

[34]   R. Acharya *et al.*, "Quantum error correction below the surface code threshold," *Nature*, Dec. 2024, ISSN: 1476-4687.

[35]   W. K. Wootters and W. H. Zurek, "A single quantum cannot be cloned," *Nature*, vol. 299, pp. 802–803, 1982.

[36]   H.-K. Lo, T. Spiller, and S. Popescu, *Introduction to Quantum Computation and Information*. World Scientific, 1998.

[37]   E. Knill *et al.*, "Randomized benchmarking of quantum gates," *Physical Review A*, vol. 77, p. 012 307, 1 Jan. 2008.

[38]   P. Shor, "Fault-tolerant quantum computation," in *Proceedings of 37th Conference on Foundations of Computer Science*, 1996, pp. 56–65.

[39]   J. PRESKILL, "Fault-tolerant quantum computation," in *Introduction to Quantum Computation and Information*, pp. 213–269.

[40]   A. G. Fowler, M. Mariantoni, J. M. Martinis, and A. N. Cleland, "Surface codes: Towards practical large-scale quantum computation," *Physical Review A*, vol. 86, no. 3, Sep. 2012, ISSN: 1094-1622.

[41]   J. M. Martinis, "Qubit metrology for building a fault-tolerant quantum computer," *npj Quantum Information*, vol. 1, no. 1, p. 15 005, Oct. 2015, ISSN: 2056-6387.

[42]   A. Kitaev, "Fault-tolerant quantum computation by anyons," *Annals of Physics*, vol. 303, no. 1, pp. 2–30, 2003.

[43]   E. Dennis, A. Kitaev, A. Landahl, and J. Preskill, "Topological quantum memory," *Journal of Mathematical Physics*, vol. 43, no. 9, pp. 4452–4505, 2002.

[44]   Z. Chen *et al.*, "Exponential suppression of bit or phase errors with cyclic error correction," *Nature*, vol. 595, no. 7867, pp. 383–387, Jul. 2021, ISSN: 1476-4687.

[45]   Y. Zhao *et al.*, "Realization of an error-correcting surface code with superconducting qubits," *Physical Review Letters*, vol. 129, p. 030 501, 3 Jul. 2022.

[46] R. Raussendorf and J. Harrington, "Fault-tolerant quantum computation with high threshold in two dimensions," *Physical review letters*, vol. 98, no. 19, p. 190 504, 2007.

[47] H. Bombin, "Topological subsystem codes," *Physical review A*, vol. 86, no. 3, p. 032 329, 2012.

[48] D. S. Wang, A. G. Fowler, and L. C. Hollenberg, "Surface codes: Reduced overhead for topological quantum error correction," *Physical Review A*, vol. 83, no. 1, p. 010 301, 2010.

[49] R. Barends *et al.*, "Superconducting quantum circuits at the surface code threshold for fault tolerance," *Nature*, vol. 508, no. 7497, pp. 500–503, 2014.

[50] A. Corcoles *et al.*, "Demonstration of a universal set of gates for a protected superconducting qubit," *Physical review letters*, vol. 114, no. 15, p. 150 501, 2015.

[51] A. Neill *et al.*, "Accurate multi-qubit randomized benchmarking," *Physical Review Letters*, vol. 121, no. 16, p. 160 501, 2018.

[52] F. Arute *et al.*, "Quantum supremacy using a programmable superconducting processor," *Nature*, vol. 574, no. 7779, pp. 505–510, 2019.

[53] E. Jeffrey *et al.*, "Fast accurate state measurement of superconducting qubits," *Physical review letters*, vol. 112, no. 19, p. 190 504, 2014.

[54] T. Walter *et al.*, "Rapid high-fidelity single-shot measurement of a singlet-triplet qubit with a rf resonator," *Physical review letters*, vol. 118, no. 26, p. 263 601, 2017.

[55] R. Vijay, D. Slichter, and I. Siddiqi, "Invited review article: Quantum-limited measurement of superconducting qubits," *Review of Scientific Instruments*, vol. 82, no. 11, p. 111 101, 2011.

[56] M. Hatridge, R. Vijay, D. Slichter, J. Clarke, and I. Siddiqi, "Dispersive readout of a superconducting qubit using a broadband josephson parametric amplifier," *Physical review B*, vol. 87, no. 14, p. 140 501, 2013.

[57] E. Magesan *et al.*, "Reducing crosstalk in multi-qubit randomized benchmarking," *Physical Review Letters*, vol. 109, no. 8, p. 080 505, 2012.

[58] D. C. McKay, S. Filipp, T. Meunier, S. Wollmann, P. J. Leek, *et al.*, "Efficient CZ-gates for quantum computing," *Physical Review A*, vol. 96, no. 6, p. 062 327, 2017.

[59] J. Chow *et al.*, "Microwave-activated selective population of noncomputational states for high-fidelity qubits," *Physical review letters*, vol. 109, no. 6, p. 060 501, 2012.

[60] J. Gambetta, J. Chow, and M. Steffen, "Building a fault-tolerant quantum computer using concatenated cat codes," *npj Quantum Information*, vol. 3, no. 1, pp. 1–7, 2017.

[61] V. Bouchiat, D. Vion, P. Joyez, D. Esteve, and M. H. Devoret, "Quantum coherence with a single cooper pair," *Physica Scripta*, vol. 1998, no. T76, p. 165, Jan. 1998.

[62] Y. A. Pashkin, O. Astafiev, T. Yamamoto, Y. Nakamura, and J. S. Tsai, "Josephson charge qubits: A brief review," *Quantum Information Processing*, vol. 8, no. 2, pp. 55–80, Jun. 2009, ISSN: 1573-1332.

[63] J. E. Mooij, T. P. Orlando, L. Levitov, L. Tian, C. H. van der Wal, and S. Lloyd, "Josephson persistent-current qubit," *Science*, vol. 285, no. 5430, pp. 1036–1039, 1999.

[64] T. P. Orlando *et al.*, "Superconducting persistent-current qubit," *Phys. Rev. B*, vol. 60, pp. 15 398–15 413, 22 Dec. 1999.

[65] J. M. Martinis, S. Nam, J. Aumentado, and C. Urbina, "Rabi oscillations in a large josephson-junction qubit," *Physical Review Letters*, vol. 89, p. 117 901, 11 Aug. 2002.

[66] J. Koch *et al.*, "Charge-insensitive qubit design derived from the Cooper pair box," *Physical Review A*, vol. 76, no. 4, Oct. 2007, ISSN: 1094-1622.

[67] V. E. Manucharyan, J. Koch, L. I. Glazman, and M. H. Devoret, "Fluxonium: Single cooper-pair circuit free of charge offsets," *Science*, vol. 326, no. 5949, pp. 113–116, 2009.

[68] L. Ding *et al.*, "High-fidelity, frequency-flexible two-qubit fluxonium gates with a transmon coupler," *Phys. Rev. X*, vol. 13, p. 031 035, 3 Sep. 2023.

[69] V. Bouchiat, D. Vion, D. Esteve, and M. H. Devoret, "Quantum coherence with a single cooper pair," *Physica Scripta*, vol. T76, no. 1, p. 165, 1998.

[70] Y. Nakamura, Y. A. Pashkin, and J. S. Tsai, "Coherent control of macroscopic quantum states in a single-Cooper-pair box," *Nature*, vol. 398, no. 6730, pp. 786–788, 1999.

[71] V. Bouchiat, D. Vion, P. Joyez, D. Esteve, and M. H. Devoret, "Quantum Coherence with a Single Cooper Pair," *Physica Scripta*, vol. T76, no. 1, p. 165, Jan. 1998.

[72] J. Stehlik *et al.*, "Tunable coupling architecture for fixed-frequency transmon superconducting qubits," *Physical Review Letters*, vol. 127, no. 8, Aug. 2021, ISSN: 1079-7114.

[73] D. Vion *et al.*, "Manipulating the quantum state of an electrical circuit," *Science*, vol. 296, no. 5569, pp. 886–889, 2002.

[74] J. M. Martinis, S. Nam, J. Aumentado, K. M. Lang, and C. Urbina, "Decoherence of a superconducting qubit due to bias noise," *Phys. Rev. B*, vol. 67, p. 094 510, 9 Mar. 2003.

[75] M. D. Hutchings *et al.*, "Tunable superconducting qubits with flux-independent coherence," *Physical Review Appl.*, vol. 8, p. 044 003, 4 Oct. 2017.

[76] A. Wallraff *et al.*, "Strong coupling of a single photon to a superconducting qubit using circuit quantum electrodynamics," *Nature*, vol. 431, no. 7005, pp. 162–167, Sep. 2004, ISSN: 1476-4687.

[77] A. Blais, R.-S. Huang, A. Wallraff, S. M. Girvin, and R. J. Schoelkopf, "Cavity quantum electrodynamics for superconducting electrical circuits: An architecture for quantum computation," *Physical Review A*, vol. 69, p. 062 320, 6 Jun. 2004.

[78] M. Göppl *et al.*, "Coplanar waveguide resonators for circuit quantum electrodynamics," *Journal of Applied Physics*, vol. 104, no. 11, p. 113 904, Dec. 2008, ISSN: 0021-8979.

[79] J. Zotova *et al.*, "Compact superconducting microwave resonators based on Al-AlO$_x$-al capacitors," *Physical Review Appl.*, vol. 19, p. 044 067, 4 Apr. 2023.

[80] L. S. Bishop, E. Ginossar, and S. M. Girvin, "Response of the strongly driven Jaynes-Cummings oscillator," *Physical Review Letters*, vol. 105, p. 100 505, 10 Sep. 2010.

[81] F. Motzoi, J. M. Gambetta, P. Rebentrost, and F. K. Wilhelm, "Simple pulses for elimination of leakage in weakly nonlinear qubits," *Physical Review Letters*, vol. 103, p. 110 501, 11 Sep. 2009.

[82] J. M. Gambetta, F. Motzoi, S. T. Merkel, and F. K. Wilhelm, "Analytic control methods for high-fidelity unitary operations in a weakly nonlinear oscillator," *Physical Review A*, vol. 83, p. 012 308, 1 Jan. 2011.

[83] F. Motzoi and F. K. Wilhelm, "Improving frequency selection of driven pulses using derivative-based transition suppression," *Physical Review A*, vol. 88, p. 062 318, 6 Dec. 2013.

[84] T. Walter *et al.*, "Rapid high-fidelity single-shot dispersive readout of superconducting qubits," *Physical Review Applied*, vol. 7, p. 054 020, 5 May 2017.

[85] J. Heinsoo *et al.*, "Rapid high-fidelity multiplexed readout of superconducting qubits," *Physical Review Applied*, vol. 10, p. 034 040, 3 Sep. 2018.

[86] M. A. Rol *et al.*, "Restless tuneup of high-fidelity qubit gates," *Physical Review Applied*, vol. 7, p. 041 001, 4 Apr. 2017.

[87] J. Emerson, R. Alicki, and K. Życzkowski, "Scalable noise estimation with random unitary operators," *Journal of Optics B: Quantum and Semiclassical Optics*, vol. 7, no. 10, S347–S352, Sep. 2005.

[88] E. Magesan, J. M. Gambetta, and J. Emerson, "Scalable and robust randomized benchmarking of quantum processes," *Physical Review Letters*, vol. 106, p. 180 504, 18 May 2011.

[89] T. Abad, J. Fernández-Pendás, A. Frisk Kockum, and G. Johansson, "Universal fidelity reduction of quantum operations from weak dissipation," *Physical Review Letters*, vol. 129, no. 15, Oct. 2022, ISSN: 1079-7114.

[90] B. Foxen *et al.*, "Demonstrating a continuous set of two-qubit gates for near-term quantum algorithms," *Physical Review Letters*, vol. 125, p. 120 504, 12 Sep. 2020.

[91] Y. Xu *et al.*, "High-fidelity, high-scalability two-qubit gate scheme for superconducting qubits," *Physical Review Letters*, vol. 125, p. 240 503, 24 Dec. 2020.

[92] V. Negirneac *et al.*, "High-fidelity controlled-Z gate with maximal intermediate leakage operating at the speed limit in a superconducting quantum processor," *Physical Review Letters*, vol. 126, p. 220 502, 22 Jun. 2021.

[93] Y. Sung *et al.*, "Realization of high-fidelity CZ and ZZ-free iSWAP gates with a tunable coupler," *Physical Review X*, vol. 11, no. 2, Jun. 2021, ISSN: 2160-3308.

[94] J. Heinsoo *et al.*, "Rapid High-fidelity Multiplexed Readout of Superconducting Qubits," *Physical Review Applied*, vol. 10, no. 3, p. 034 040, Sep. 2018, ISSN: 2331-7019.

[95] S. S. Elder *et al.*, "High-fidelity measurement of qubits encoded in multilevel superconducting circuits," *Physical Review X*, vol. 10, p. 011 001, 1 Jan. 2020.

[96] Y. Sunada *et al.*, "Fast readout and reset of a superconducting qubit coupled to a resonator with an intrinsic Purcell filter," *Physical Review Applied*, vol. 17, p. 044 016, 4 Apr. 2022.

[97] A. Blais, A. L. Grimsmo, S. M. Girvin, and A. Wallraff, "Circuit quantum electrodynamics," *Reviews of Modern Physics*, vol. 93, no. 2, May 2021, ISSN: 1539-0756.

[98] P. Campagne-Ibarcq *et al.*, "Deterministic remote entanglement of superconducting circuits through microwave two-photon transitions," *Physical Review Letters*, vol. 120, p. 200 501, 20 May 2018.

[99] P. Kurpiers *et al.*, "Deterministic quantum state transfer and remote entanglement using microwave photons," *Nature*, vol. 558, no. 7709, pp. 264–267, Jun. 2018, ISSN: 1476-4687.

[100] P. Kurpiers *et al.*, "Quantum communication with time-bin encoded microwave photons," *Physical Review Applied*, vol. 12, p. 044 067, 4 Oct. 2019.

[101] J. Ilves *et al.*, "On-demand generation and characterization of a microwave time-bin qubit," *npj Quantum Information*, vol. 6, no. 1, p. 34, 2020.

[102] P. Magnard *et al.*, "Microwave quantum link between superconducting circuits housed in spatially separated cryogenic systems," *Physical Review Letters*, vol. 125, p. 260 502, 26 Dec. 2020.

[103] R. Dassonneville *et al.*, "Fast high-fidelity quantum nondemolition qubit readout via a nonperturbative cross-kerr coupling," *Physical Review X*, vol. 10, p. 011 045, 1 Feb. 2020.

[104] M. D. Reed *et al.*, "High-fidelity readout in circuit quantum electrodynamics using the Jaynes-Cummings nonlinearity," *Physical Review Letters*, vol. 105, p. 173 601, 17 Oct. 2010.

[105] D. Gusenkova *et al.*, "Quantum nondemolition dispersive readout of a superconducting artificial atom using large photon numbers," *Physical Review Applied*, vol. 15, p. 064 030, 6 Jun. 2021.

[106] F. Mallet *et al.*, "Single-shot qubit readout in circuit quantum electrodynamics," *Nat. Phys.*, vol. 5, no. 11, pp. 791–795, 2009.

[107] E. A. Sete, J. M. Martinis, and A. N. Korotkov, "Quantum theory of a bandpass Purcell filter for qubit readout," *Physical Review A*, vol. 92, no. 1, p. 012 325, Jul. 2015, ISSN: 1050-2947.

[108] B. Yurke *et al.*, "Observation of parametric amplification and deamplification in a Josephson parametric amplifier," *Physical Review A*, vol. 39, pp. 2519–2533, 1989.

[109] J. Y. Mutus *et al.*, "Strong environmental coupling in a Josephson parametric amplifier," *Applied Physics Letters*, vol. 104, no. 26, p. 263 513, 2014.

[110] C. Macklin *et al.*, "A near quantum-limited Josephson traveling-wave parametric amplifier," *Science*, vol. 350, no. 6258, pp. 307–310, 2015.

[111] M. Renger *et al.*, "Beyond the standard quantum limit for parametric amplification of broadband signals," *npj Quantum Information*, vol. 7, no. 1, p. 160, Nov. 2021, ISSN: 2056-6387.

[112] P. A. Spring *et al.*, "Fast multiplexed superconducting qubit readout with intrinsic purcell filtering," *arXiv*, 2024.

[113] C. W. Gardiner and M. J. Collett, "Input and output in damped quantum systems: Quantum stochastic differential equations and the master equation," *Physical Review A*, vol. 31, pp. 3761–3774, 6 Jun. 1985.

[114] S. Kosen *et al.*, "Building blocks of a flip-chip integrated superconducting quantum processor," *Quantum Science and Technology*, vol. 7, no. 3, p. 035 018, Jun. 2022, ISSN: 2058-9565.

[115] M. J. Peterer *et al.*, "Coherence and decay of higher energy levels of a superconducting transmon qubit," *Physical Review Letters*, vol. 114, p. 010 501, 1 Jan. 2015.

[116] B. D'Anjou and W. A. Coish, "Enhancing qubit readout through dissipative sub-Poissonian dynamics," *Physical Review A*, vol. 96, p. 052 321, 5 Nov. 2017.

[117] P. Jurcevic *et al.*, "Demonstration of quantum volume 64 on a superconducting quantum computing system," *Quantum Science and Technology*, vol. 6, no. 2, p. 025 020, Mar. 2021.

[118] N. Cottet, H. Xiong, L. B. Nguyen, Y.-H. Lin, and V. E. Manucharyan, "Electron shelving of a superconducting artificial atom," *Nature Communications*, vol. 12, no. 1, p. 6383, 2021.

[119] C. Wang, M.-C. Chen, C.-Y. Lu, and J.-W. Pan, "Optimal readout of superconducting qubits exploiting high-level states," *Fundamental Research*, vol. 1, no. 1, pp. 16–21, 2021, ISSN: 2667-3258.

[120] M. S. Jattana, F. Jin, H. De Raedt, and K. Michielsen, "General error mitigation for quantum circuits," *Quantum Information Processing*, vol. 19, no. 11, p. 414, Nov. 2020, ISSN: 1573-1332.

[121] T. Baumgratz, A. Nüßeler, M. Cramer, and M. B. Plenio, "A scalable maximum likelihood method for quantum state tomography," *New Journal of Physics*, vol. 15, no. 12, p. 125 004, Dec. 2013.

[122] D. Sank *et al.*, "Measurement-induced state transitions in a superconducting qubit: Beyond the rotating wave approximation," *Physical Review Letters*, vol. 117, p. 190 503, 19 Nov. 2016.

[123] D. H. Slichter *et al.*, "Measurement-induced qubit state mixing in circuit qed from up-converted dephasing noise," *Physical Review Letters*, vol. 109, p. 153 601, 15 Oct. 2012.

[124] D. I. Schuster *et al.*, "AC stark shift and dephasing of a superconducting qubit strongly coupled to a cavity field," *Physical Review Letters*, vol. 94, p. 123 602, 12 Mar. 2005.

[125] J. Gambetta *et al.*, "Qubit-photon interactions in a cavity: Measurement-induced dephasing and number splitting," *Physical Review A*, vol. 74, p. 042 318, 4 Oct. 2006.

[126] D. I. Schuster *et al.*, "Resolving photon number states in a superconducting circuit," *Nature*, vol. 445, no. 7127, pp. 515–518, Feb. 2007, ISSN: 1476-4687.

[127] H. Wang *et al.*, "Measurement of the decay of Fock states in a superconducting quantum circuit," *Physical Review Letters*, vol. 101, p. 240 401, 24 Dec. 2008.

[128] D. Ristè, J. G. van Leeuwen, H.-S. Ku, K. W. Lehnert, and L. Di-Carlo, "Initialization by measurement of a superconducting quantum bit circuit," *Physical Review Letters*, vol. 109, p. 050 507, 5 Aug. 2012.

[129] E. Magesan, J. M. Gambetta, A. D. Córcoles, and J. M. Chow, "Machine learning for discriminating quantum measurement trajectories and improving readout," *Physical Review Letters*, vol. 114, p. 200 501, 20 May 2015.

[130] B. Lienhard *et al.*, "Deep-neural-network discrimination of multiplexed superconducting-qubit states," *Physical Review Applied*, vol. 17, p. 014 024, 1 Jan. 2022.

[131] Y. Bengio and A. Courville, "Deep learning of representations," in *Handbook on Neural Information Processing*, M. Bianchini, M. Maggini, and L. C. Jain, Eds. Berlin, Heidelberg: Springer Berlin Heidelberg, 2013, pp. 1–28, ISBN: 978-3-642-36657-4.

[132] P. Duan, Z.-F. Chen, Q. Zhou, W.-C. Kong, H.-F. Zhang, and G.-P. Guo, "Mitigating crosstalk-induced qubit readout error with shallow-neural-network discrimination," *Physical Review Applied*, vol. 16, p. 024 063, 2 Aug. 2021.

[133] R. Navarathna *et al.*, "Neural networks for on-the-fly single-shot state classification," *Applied Physics Letters*, vol. 119, no. 11, p. 114 003, 2021.

[134] C. C. Bultink *et al.*, "General method for extracting the quantum efficiency of dispersive qubit readout in circuit QED," *Applied Physics Letters*, vol. 112, no. 9, p. 092 601, 2018.

[135] B. Lienhard, "Machine learning assisted superconducting qubit readout," Ph.D. dissertation, MIT, 2021.

[136] C. M. Caves, "Quantum limits on noise in linear amplifiers," *Phys. Rev. D*, vol. 26, p. 1817, 1982.

[137] T. Yamamoto *et al.*, "Flux-driven Josephson parametric amplifier," *Appl. Phys. Lett.*, vol. 93, p. 042 510, 2008.

[138] N. Bergeal *et al.*, "Phase-preserving amplification near the quantum limit with a Josephson ring modulator," *Nature*, vol. 465, p. 64, 2010.

[139] N. Roch *et al.*, "Widely tunable, nondegenerate three-wave mixing microwave device operating near the quantum limit," *Physical Review Letters*, vol. 108, p. 147 701, 2012.

[140] A. Roy and M. Devoret, "Introduction to parametric amplification of quantum signals with Josephson circuits," *Comptes Rendus Phys.*, vol. 17, p. 740, 2016.

[141] J. Aumentado, "Superconducting parametric amplifiers," *IEEE Microwave magazine*, vol. 21, pp. 45–59, 2020.

[142] R. J. Schoelkopf and S. M. Girvin, "Wiring up quantum systems," *Nature*, vol. 451, p. 664, 2008.

[143] H. Kanter and A. H. Silver, "Self-pumped Josephson parametric amplification," *Appl. Phys. Lett.*, vol. 19, pp. 515–517, 1971.

[144] M. J. Feldman, P. T. Parrish, and R. Y. Chiao, "Parametric amplification by unbiased josephson junctions," *J. Appl. Phys.*, vol. 46, pp. 4031–4042, 1975.

[145] B. Yurke *et al.*, "Observation of 4.2-K equilibrium-noise squeezing via a Josephson-parametric amplifier," *Physical Review Letters*, vol. 60, pp. 764–767, 1988.

[146] H. K. Olsson and T. Claeson, "Low-noise Josephson parametric amplification and oscillations at 9 ghz," *J. Appl. Phys.*, vol. 64, pp. 5234–5243, 1988.

[147] M. A. Castellanos-Beltran, K. D. Irwin, G. C. Hilton, L. R. Vale, and K. W. Lehnert, "Amplification and squeezing of quantum noise with a tunable Josephson metamaterial," *Nature Phys.*, vol. 4, p. 929, 2008.

[148] T. Roy *et al.*, "Broadband parametric amplification with impedance engineering: Beyond the gain-bandwidth product," *Appl. Phys. Lett.*, vol. 107, p. 262 601, 2015.

[149] M. Simoen *et al.*, "Characterization of a multimode coplanar waveguide parametric amplifier," *J. Appl. Phys.*, vol. 118, p. 154 501, 2015.

[150] A. L. CULLEN, "A travelling-wave parametric amplifier," *Nature*, vol. 181, no. 4605, pp. 332–332, Feb. 1958, ISSN: 1476-4687.

[151] P. K. Tien and H. Suhl, "A traveling-wave ferromagnetic amplifier," *Proc. lnst. Radio Engrs.*, vol. 46, p. 700, 1958.

[152] P. K. Tien, "Parametric amplification and frequency mixing in propagating circuits," *J. Appl. Phys.*, vol. 29, p. 1347, 1958.

[153] L. Chen *et al.*, "Transmon qubit readout fidelity at the threshold for quantum error correction without a quantum-limited amplifier," *npj Quantum Information*, vol. 9, no. 1, Mar. 2023, ISSN: 2056-6387.

[154] F. Arute *et al.*, "Quantum supremacy using a programmable superconducting processor," *Nature*, vol. 574, no. 7779, pp. 505–510, 2019, ISSN: 1476-4687.

[155] L. DiCarlo *et al.*, "Demonstration of two-qubit algorithms with a superconducting quantum processor," *Nature*, vol. 460, pp. 240–4, Jul. 2009.

[156] M. Kjaergaard *et al.*, "Superconducting qubits: Current state of play," *Annual Review of Condensed Matter Physics*, vol. 11, no. Volume 11, 2020, pp. 369–395, 2020, ISSN: 1947-5462.

[157] R. Barends *et al.*, "Superconducting quantum circuits at the surface code threshold for fault tolerance," en, *Nature*, vol. 508, no. 7497, pp. 500–503, Apr. 2014, ISSN: 1476-4687.

[158] M. Neeley *et al.*, "Generation of three-qubit entangled states using superconducting phase qubits," *Nature*, vol. 467, pp. 570–3, Sep. 2010.

[159] A. Dewes *et al.*, "Characterization of a two-transmon processor with individual single-shot qubit readout," *Physical Review Letters*, vol. 108, p. 057 002, 5 Feb. 2012.

[160] Y. Chen *et al.*, "Qubit architecture with high coherence and fast tunable coupling," *Physical Review Letters*, vol. 113, p. 220 502, 22 Nov. 2014.

[161] M. A. Rol *et al.*, "Fast, high-fidelity conditional-phase gate exploiting leakage interference in weakly anharmonic superconducting qubits," *Physical Review Letters*, vol. 123, p. 120 502, 12 Sep. 2019.

[162] J. M. Chow *et al.*, "Simple all-microwave entangling gate for fixed-frequency superconducting qubits," *Physical Review Letters*, vol. 107, p. 080 502, 8 Aug. 2011.

[163] S. Sheldon, E. Magesan, J. M. Chow, and J. M. Gambetta, "Procedure for systematically tuning up cross-talk in the cross-resonance gate," *Physical Review A*, vol. 93, p. 060 302, 6 Jun. 2016.

[164] S. Poletto *et al.*, "Entanglement of two superconducting qubits in a waveguide cavity via monochromatic two-photon excitation," *Physical Review Letters*, vol. 109, p. 240 505, 24 Dec. 2012.

[165] J. M. Chow, J. M. Gambetta, A. W. Cross, S. T. Merkel, C. Rigetti, and M. Steffen, "Microwave-activated conditional-phase gate for superconducting qubits," *New Journal of Physics*, vol. 15, no. 11, p. 115 012, Nov. 2013.

[166] H. Paik *et al.*, "Experimental demonstration of a resonator-induced phase gate in a multiqubit circuit-qed system," *Physical Review Letters*, vol. 117, p. 250 502, 25 Dec. 2016.

[167] S. Caldwell *et al.*, "Parametrically Activated Entangling Gates Using Transmon Qubits," en, *arXiv*, Jun. 2017.

[168] M. Reagor *et al.*, "Demonstration of universal parametric entangling gates on a multi-qubit lattice," *Science Advances*, vol. 4, no. 2, eaao3603, Feb. 2018, ISSN: 2375-2548.

[169] S. S. Hong *et al.*, "Demonstration of a Parametrically-Activated Entangling Gate Protected from Flux Noise," *arXiv:1901.08035 [quant-ph]*, Jan. 2019, arXiv: 1901.08035.

[170] D. C. McKay, S. Filipp, A. Mezzacapo, E. Magesan, J. M. Chow, and J. M. Gambetta, "Universal Gate for Fixed-Frequency Qubits via a Tunable Bus," *Physical Review Applied*, vol. 6, no. 6, p. 064 007, Dec. 2016.

[171] M. Roth, M. Ganzhorn, N. Moll, S. Filipp, G. Salis, and S. Schmidt, "Analysis of a parametrically driven exchange-type gate and a two-photon excitation gate between superconducting qubits," *Physical Review A*, vol. 96, no. 6, p. 062 323, Dec. 2017.

[172] P. Krantz, M. Kjaergaard, F. Yan, T. P. Orlando, S. Gustavsson, and W. D. Oliver, "A quantum engineer's guide to superconducting qubits," *Applied Physics Reviews*, vol. 6, no. 2, p. 021 318, 2019.

[173] R. Li, K. Kubo, Y. Ho, Z. Yan, Y. Nakamura, and H. Goto, "Realization of high-fidelity CZ gate based on a double-Transmon coupler," *Phys. Rev. X*, vol. 14, p. 041 050, 4 Nov. 2024.

[174] M. Reagor *et al.*, "Demonstration of universal parametric entangling gates on a multi-qubit lattice," *Science Advances*, vol. 4, no. 2, eaao3603, 2018.

[175] C. Križan *et al.*, "Quantum swap gate realized with cz and iswap gates in a superconducting architecture," *arXiv*, 2024.

[176] F. Leymann and J. Barzen, "The bitter truth about gate-based quantum algorithms in the NISQ era," *Quantum Science and Technology*, vol. 5, no. 4, p. 044 007, Sep. 2020, ISSN: 2058-9565.

[177] J.-X. Han, J. Zhang, G.-M. Xue, H. Yu, and G. Long, "Protecting logical qubits with dynamical decoupling," arXiv:2402.05604, 2024.

[178] D. M. Abrams, N. Didier, B. R. Johnson, M. P. da Silva, and C. A. Ryan, "Implementation of XY entangling gates with a single calibrated pulse," *Nature Electronics*, vol. 3, no. 12, pp. 744–750, Dec. 2020, ISSN: 2520-1131.

[179] G. Yan *et al.*, "Quantum circuit synthesis and compilation optimization: Overview and prospects," arXiv:2407.00736, 2024.

[180] A. T. Rezakhani, "Characterization of two-qubit perfect entanglers," *Physical Review A*, vol. 70, no. 5, Nov. 2004, ISSN: 1094-1622.

[181] A. Mondal and K. K. Parhi, "Quantum circuits for stabilizer error correcting codes: A tutorial," *IEEE Circuits Syst. Mag.*, vol. 24, no. 1, pp. 33–51, 2024, ISSN: 1558-0830.

[182] J. Fernández-Pendás, "Fast parameteric two-qubit gate," in prep.

[183] N. Hansen, S. Müller, and P. Koumoutsakos, "Reducing the time complexity of the derandomized evolution strategy with covariance matrix adaptation (CMA-ES)," *Evolutionary computation*, vol. 11, pp. 1–18, Feb. 2003.

[184] N. Hansen, "The CMA evolution strategy: A tutorial," *arXiv*, Jan. 2010.

[185] E. Knill *et al.*, "Randomized benchmarking of quantum gates," *Physical Review A*, vol. 77, p. 012 307, 1 Jan. 2008.

[186] E. Onorati, A. H. Werner, and J. Eisert, "Randomized benchmarking for individual quantum gates," *Physical Review Letters*, vol. 123, p. 060 501, 6 Aug. 2019.

[187] P. J. J. O'Malley *et al.*, "Qubit metrology of ultralow phase noise using randomized benchmarking," *Physical Review Applied*, vol. 3, p. 044 009, 4 Apr. 2015.

[188] M. McEwen *et al.*, "Removing leakage-induced correlated errors in superconducting quantum error correction," *Nature Communications*, vol. 12, p. 1761, 2021.

[189] J. F. Marques *et al.*, "All-microwave leakage reduction units for quantum error correction with superconducting transmon qubits," *Physical Review Letters*, vol. 130, p. 250 602, 25 Jun. 2023.

[190] K. C. Miao *et al.*, "Overcoming leakage in quantum error correction," *Nature Physics*, vol. 19, no. 12, pp. 1780–1786, Dec. 2023, ISSN: 1745-2481.

[191] F. Battistel, B. Varbanov, and B. Terhal, "Hardware-efficient leakage-reduction scheme for quantum error correction with superconducting Transmon qubits," *PRX Quantum*, vol. 2, p. 030 314, 3 Jul. 2021.

[192] X. Yang *et al.*, "Coupler-assisted leakage reduction for scalable quantum error correction with superconducting qubits," *arXiv*, 2024.

[193] C. M. Diniz, C. J. V. Bôas, and A. C. Santos, "Scalable quantum eraser for superconducting integrated circuits," 2024.

[194] D. Egger *et al.*, "Pulsed reset protocol for fixed-frequency superconducting qubits," *Physical Review Applied*, vol. 10, p. 044 030, Oct. 2018.

[195] K. Geerlings *et al.*, "Demonstrating a driven reset protocol for a superconducting qubit," *Physical Review Letters*, vol. 110, p. 120 501, 12 Mar. 2013.

[196] M. S. Moreira *et al.*, "Realization of a quantum neural network using repeat-until-success circuits in a superconducting quantum processor," *npj Quantum Information*, vol. 9, p. 118, Nov. 2023.

[197] Y. Zhou *et al.*, "Rapid and unconditional parametric reset protocol for tunable superconducting qubits," *Nature Communications*, vol. 12, p. 5924, Oct. 2021.

[198] P. Magnard *et al.*, "Fast and unconditional all-microwave reset of a superconducting qubit," *Physical Review Letters*, vol. 121, p. 060 502, 6 Aug. 2018.

[199] G. B. P. Huber *et al.*, "Parametric multi-element coupling architecture for coherent and dissipative control of superconducting qubits," *arXiv*, 2024.

[200] N. Lacroix *et al.*, "Fast flux-activated leakage reduction for superconducting quantum circuits," *arXiv*, 2023.

[201] D. C. McKay, S. Filipp, A. Mezzacapo, E. Magesan, J. M. Chow, and J. M. Gambetta, "Universal gate for fixed-frequency qubits via a tunable bus," *Physical Review Applied*, vol. 6, p. 064 007, 6 Dec. 2016.

[202] F. Yan *et al.*, "Tunable coupling scheme for implementing high-fidelity two-qubit gates," *Physical Review Applied*, vol. 10, p. 054 062, 5 Nov. 2018.

[203] S. Bravyi, D. P. DiVincenzo, and D. Loss, "Schrieffer–Wolff transformation for quantum many-body systems," *Annals of Physics*, vol. 326, no. 10, pp. 2793–2826, 2011, ISSN: 0003-4916.

[204] S. E.C.G., "Theory of inelastic collisions between atoms," *Helvetica Physica Acta*, no. 5, pp. 369–423, 1932.

[205] L. L., "On the theory of transfer of energy at collisions I," *Physikalische Zeitschrift der Sowjetunion*, vol. 1, p. 88, 1932.

[206] O. V. Ivakhnenko, S. N. Shevchenko, and F. Nori, "Nonadiabatic landau–zener–stückelberg–majorana transitions, dynamics, and interference," *Physics Reports*, vol. 995, pp. 1–89, 2023, Nonadiabatic Landau-Zener-Stückelberg-Majorana transitions, dynamics, and interference, ISSN: 0370-1573.

[207] S. Kosen *et al.*, "Signal crosstalk in a flip-chip quantum processor," *PRX Quantum*, vol. 5, no. 3, Sep. 2024, ISSN: 2691-3399.

[208] A. Osman *et al.*, "Mitigation of frequency collisions in superconducting quantum processors," *Physical Review Research*, vol. 5, p. 043 001, 4 Oct. 2023.

[209] J. Roland and N. J. Cerf, "Quantum search by local adiabatic evolution," *Physical Review A*, vol. 65, p. 042 308, 4 Mar. 2002.

[210] T. Albash and D. A. Lidar, "Adiabatic quantum computation," *Reviews of Modern Physics*, vol. 90, p. 015 002, 1 Jan. 2018.

[211] D. Stefanatos and E. Paspalakis, "Speeding up adiabatic passage with an optimal modified Roland–Cerf protocol," *Journal of Physics A: Mathematical and Theoretical*, vol. 53, no. 11, p. 115 304, Feb. 2020.

[212] N. Malossi *et al.*, "Quantum driving protocols for a two-level system: From generalized Landau-Zener sweeps to transitionless control," *Physical Review A*, vol. 87, p. 012 116, 1 Jan. 2013.

[213] M. G. Bason *et al.*, "High-fidelity quantum driving," *Nature Physics*, vol. 8, no. 2, pp. 147–152, 2012.

[214] D. Stefanatos and E. Paspalakis, "Resonant shortcuts for adiabatic rapid passage with only *z*-field control," *Physical Review A*, vol. 100, p. 012 111, 1 Jul. 2019.

[215] F. Petiziol, B. Dive, S. Carretta, R. Mannella, F. Mintert, and S. Wimberger, "Accelerating adiabatic protocols for entangling two qubits in circuit qed," *Physical Review A*, vol. 99, p. 042 315, 4 Apr. 2019.

[216] S. P. Fors, J. Fernández-Pendás, and A. F. Kockum, "Comprehensive explanation of ZZ coupling in superconducting qubits," *arXiv*, 2024.

[217] A. Auger and N. Hansen, "A restart CMA Evolution Strategy with increasing population size," *2005 IEEE Congress on Evolutionary Computation*, vol. 2, pp. 1769–1776, 2005.

[218] G. P. Gehér, M. Jastrzebski, E. T. Campbell, and O. Crawford, "To reset, or not to reset – that is the question," *arXiv*, 2024.

[219] *Tergite autocalibration*, Software, Apache License 2.0, Available at: https://github.com/tergite/tergite-autocalibration, 2025.

Part II

Papers

PAPER A

Transmon qubit readout fidelity at the threshold for quantum error correction without a quantum-limited amplifier

Liangyu Chen, Hang-Xi Li, Yong Lu, Christopher W. Warren, Christian J. Križan, Sandoko Kosen, Marcus Rommel, Shahnawaz Ahmed, Amr Osman, Janka Biznárová, Anita Fadavi Roudsari, Benjamin Lienhard, Marco Caputo, Kestutis Grigoras, Leif Grönberg, Joonas Govenius, Anton Frisk Kockum, Per Delsing, Jonas Bylander, Giovanna Tancredi

The layout has been revised.

PAPER B

Fast unconditional reset and leakage reduction in fixed-frequency transmon qubits

Liangyu Chen, Simon Pettersson Fors, Zixian Yan, Anaida Ali, Tahereh Abad, Amr Osman, Eleftherios Moschandreou, Benjamin Lienhard, Sandoko Kosen, Hang-Xi Li, Daryoush Shiri, Tong Liu, Stefan Hill, Abdullah-Al Amin, Robert Rehammar, Mamta Dahiya, Andreas Nylander, Marcus Rommel, Anita Fadavi Roudsari, Marco Caputo, Grönberg Leif, Joonas Govenius, Miroslav Dobsicek, Michele Faucci Giannelli, Anton Frisk Kockum, Jonas Bylander, Giovanna Tancredi

The layout has been revised.

PAPER C

Signal Crosstalk in a Flip-Chip Quantum Processor

Sandoko Kosen, Hang-Xi Li, Marcus Rommel, Robert Rehammar, Marco Caputo, Leif Grönberg, Jorge Fernández-Pendás, Anton Frisk Kockum, Janka Biznárová, **Liangyu Chen**, Christian Križan, Andreas Nylander, Amr Osman, Anita Fadavi Roudsari, Daryoush Shiri, Giovanna Tancredi, Joonas Govenius, Jonas Bylander

The layout has been revised.

Building blocks of a flip-chip integrated superconducting quantum processor

Sandoko Kosen, Hang-Xi Li, Marcus Rommel, Daryoush Shiri, Christopher Warren, Leif Grönberg, Jaakko Salonen, Tahereh Abad, Janka Biznárová, Marco Caputo, **Liangyu Chen**, Kestutis Grigoras, Göran Johansson, Anton Frisk Kockum, Christian Križan, Daniel Pérez Lozano6, Graham J Norris, Amr Osman, Jorge Fernández-Pendás, Alberto Ronzani, Anita Fadavi Roudsari, Slawomir Simbierowicz, Giovanna Tancredi, Andreas Wallraff, Christopher Eichler, Joonas Govenius and Jonas Bylander

The layout has been revised.

PAPER E

Quantum SWAP gate realized with CZ and iSWAP gates in a superconducting architecture

Christian Križan, Janka Biznárová, **Liangyu Chen**, Emil Hogedal, Amr Osman, Christopher W. Warren, Sandoko Kosen, Hang-Xi Li, Tahereh Abad, Anuj Aggarwal, Marco Caputo, Jorge Fernández-Pendás, Akshay Gaikwad, Leif Grönberg, Andreas Nylander, Robert Rehammar, Marcus Rommel, Olga I. Yuzephovich, Anton Frisk Kockum, Joonas Govenius, Giovanna Tancredi, Jonas Bylander

The layout has been revised.

PAPER F

A small footprint travelling-wave parametric amplifier with a high Signal-to-Noise Ratio improvement in a wide band

Hampus Renberg Nilsson, **Liangyu Chen**, Giovanna Tancredi, Robert Rehammar, Daryoush Shiri, Filip Nilsson, Amr Osman, Vitaly Shumeiko, Per Delsing

The layout has been revised.